Confined Cavitation: An Experimental Study

Rory J. Dijkink

ISBN: 978-90-365-2822-1 (2009)

Confined Cavitation

An Experimental Study

Rory J. Dijkink

UITNODIGING

Hierbij wil ik u van harte uitnodigen voor het bijwonen van de openbare verdediging van mijn proefschrift

Confined Cavitation
An Experimental Study

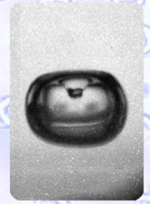

op vrijdag 12 juni 2009 om 14:45 in zaal 2 van gebouw de Spiegel van de Universiteit Twente in Enschede.

Na afloop van de promotie plechtigheid zal er een receptie zijn.

Rory J. Dijkink
Breugelmansgaarde 162
7511PV Enschede

CONFINED CAVITATION
AN EXPERIMENTAL STUDY

Samenstelling promotiecommissie:

Prof. dr. ir. L. van Wijngaarden, voorzitter	Universiteit Twente
Prof. dr. rer. nat. D. Lohse, promotor	Universiteit Twente
Assist. Prof. dr. C. D. Ohl, promotor	Universiteit Twente
Prof. dr. L. W. M. M. Terstappen	Universiteit Twente
Prof. dr. ir. A. van den Berg	Universiteit Twente
Prof. dr. A. Vogel	Institüt für Biomedizinische Optik, Universität zu Lübeck
Prof. dr. A. A. Darhuber	Technische Universiteit Eindhoven
Prof. dr. J. G. E. Gardeniers	Universiteit Twente

The research described in this thesis has been supported by the VIDI research program of the "Nederlandse Organisatie voor Wetenschappelijk Onderzoek" (NWO). It was carried out at the Physics of Fluids research group of the faculty of Science and Technology of the University of Twente and partially in Singapore during visits to the Division of Physics and Applied Physics in the School of Physical and Mathematical Sciences of Nanyang Technological University.

Nederlandse titel:
Cavitatie onder geometrische beperkingen: een experimentele studie

Publisher:
Rory J. dijkink, Physics of Fluids, University of Twente,
P.O. Box 217, 7500 AE Enschede, The Netherlands
pof.tnw.utwente.nl

Cover design: Rory J. Dijkink
Cover illustration: Bubble collapse on a single boundary, see chapters 2 and 3
Print: Gildeprint B.V., Enschede

ISBN 978-90-365-2822-1

CONFINED CAVITATION
AN EXPERIMENTAL STUDY

PROEFSCHRIFT

ter verkrijging van
de graad van doctor aan de Universiteit Twente,
op gezag van de rector magnificus,
prof. dr. H. Brinksma,
volgens besluit van het College voor Promoties
in het openbaar te verdedigen
op vrijdag 12 juni 2009 om 15.00 uur

door

Rory J. Dijkink
geboren op 2 maart 1979

te Amsterdam

Dit proefschrift is goedgekeurd door de promotoren:

prof. dr. rer. nat. Detlef Lohse

en:

assist. prof. dr. Claus-Dieter Ohl

Contents

1 Introduction

1.1 Cavitation

This thesis deals with a special type of bubble, the so called inertial cavitation bubble. Although an exact definition is not available it is a largely empty bubble which leads to violent bubble collapse cycles. These extreme volume oscillations result in fluid mechanic phenomena such as noise and shock wave emission, intense heating of the bubble interior, and even light emission [1].

After the first fundamental reports on cavitation, only dealing with spherical bubbles [2], it entered the field of engineering science [3]. Cavitation bubbles close to a rigid boundary lose their spherical symmetry [4, 5, 6] and collapse onto that surface focussing the kinetic energy of an axial liquid jet onto a very small area [7]. The resulting pressure is strong enough to cause major damage to even the hardest materials [6, 8] and thus the first line of cavitation research was to minimize cavitation damage by either preventing its initiation or removing the bubbles before they collapse. Cavitation research started at the beginning of the twentieth century when operating speeds of ship propellers passed a threshold where the created low pressure regions were now strong enough to initiate cavitation bubbles [8, 9]. Cavitation damage is still a big problem in naval engineering, but also in other area's such as valves, pumps and turbines

[10].

On the other hand people have started putting cavitation to good use. One common application is ultrasonic cleaning [11] where an ultrasound field is generated in a liquid filled bath creating clusters of cavitation bubbles with the ability to remove small particles from hard surfaces [12]. All kinds of materials ranging from surgical tools stained with blood or tissue to greasy engine parts and even fabrics [13] can be cleaned in such an ultrasonic bath.

Specialized acoustic cleaning devices exist to clean micron- and nano-sized structures in the semiconducter industry. But with the ever decreasing structure sizes the critical size of "killer" particles, i.e. a dirt particle that renders a chip inoperable, also gets smaller while the structures themselves get weaker [14]. Ultrasonics have been mostly abandoned because of the amount of damage cavitation inflicted upon the silicon substrate and structures [15]. Since then the semiconductor industry has moved to frequencies in the megahertz range to create smaller cavitation bubbles [16]. Research continues in an attempt to further understand and improve acoustic cleaning of silicon wafers.

On a larger scale cavitation is being developed for use in waste water treatment plants. On the one side acoustically generated cavitation can clean the water treatment filters and membranes in situ []. And secondly the shockwaves and jets generated by cavitation bubbles can disinfect the water by killing any microbes or other hazardous organisms present [17].

Besides killing single celled organisms from the outside cavitation generated inside an organism can destroy groups of cells internally. By generating the cavitation bubbles with acoustics, which can penetrate living tissue without causing harm, objects and cells inside a living person can be reached without physical access. These kind of techniques are called minimally invasive therapies and are already being used in medicine.

There are some differences in the acoustics used, for example a single shockwave has a single high pressure peak with a long negative pressure tail. One of the earliest applications is extracorporeal shockwave lithotripsy where the shockwaves are focussed into the body to fragment a variety of stones, e.g. kidney, renal, gallbladder, and salivary gland duct stones [18]. The reason for using focussed shockwaves is to allow the pressure wave to traverse the tissue between the lithotripter and the stone without causing damage. Only in the focal region do the pressure extrema reach the magnitudes needed for the treatment. The effects of the shockwaves on the stone are twofold: first is the direct mechanical effect of the shockwave where tensile stresses inside the stone cause it to crack and

fracture and second is the cavitation cloud created by the negative pressure tail which grinds the fragments into pieces small enough to leave the body by natural means [19, 20].

Another medical treatment uses a strong continuous acoustic field in stead of shockwaves. The technique is called HIFU (High Intensity Focussed Ultrasound) and uses again a focussed acoustic field to lyse cells only in a small focal volume [21, 22]. HIFU is used to treat a whole list of ailments that previously required surgery [23].

It is for example used to treat both benign and malignant prostate problems, i.e. benign prostate enlargement [24] and prostate cancer [25] respectively. Other locations of tumor growth (e.g. liver, kidney, breast, uterus, pancreas and bone [26]) are also easily accessed and treated with HIFU and by using a technique called time reversal to assure that each part of the acoustic field arrives in the focal volume in phase, even hard to reach tumors such as brain tumors can be reached [27].

Finally instead of treating diseased tissue by destroying or killing it, cavitation can also be used to try and cure the patient. Genes and some drugs can't freely enter a cell or it's nucleus [28]. By facilitating the uptake of foreign materials into the affected cells cavitation can be used to locally treat diseases[22, 29].

1.2 Cell transfection

There are many diseases which are genetic in origin and many of them have already been identified and located on the genome. To cure these diseases the genes coding for the disease have to be replaced or deactivated, this is called gene therapy. And though the genes themselves have to be developed for each case separately it is the method of delivery, essential for all of gene therapy, which is still a big problem especially for in vivo treatment [30].

The easiest approach is to use something which already exists and as it happens there already exists a very efficient tool for transfection of genetic material into cells, i.e. viruses. There are however some drawbacks to using modified viral vectors such as possible toxicity, the body's immune response, the limited amount of genetic material they can transfect and producing the viral vectors in large quantities [31].

Because of these limitations alternatives have been developed which can largely be divided into two groups: Nonviral vectors and gene delivery by physical means [32]. The nonviral vectors use different molecules

to bond with or encapsule the DNA and thus get the genes into the cell nucleus. A wide variety of artificial vectors is described in literature (e.g. [31, 30, 32]).

There are currently three major means of physical transfection that, though less efficient than viral vectors, they are non-toxic, they don't incite an immune response and can be administered at predefined locations [30, 32]. The basic idea for all three methods is to temporarily create pores in the cell membrane such that foreign materials can enter the cell, without killing it. Because of this, physical delivery systems aren't specific to genetic material but will also work for other drugs that need to be inserted into cells for treatment [33, 34, 12].

The first method is called the "gene-gun" where particles coated with DNA are shot into exposed tissue at high speed. The particles penetrate a few millimeter into the tissue depositing the genetic material along the way. It's short working depth means it's mainly suitable for in vitro use and transdermal drug delivery. It can be used on internal organs and tissue but only when they are made accessible by surgery [35, 30].

The cell membrane can also be temporarily permeabilized using pulsed electric fields. This technique, called electroporation or electropermeabilization, charges the the double lipid layer of a cells outer membrane similar to an electric capacitor. When the applied transmembrane potential exceeds the dielectric strength of the membrane holes are forced open in the membrane allowing foreign molecules to enter the cell [36, 33]. To apply the electric field in vivo needle or plate electrodes are used. For treatment of cells deeper in the body surgery is again needed to gain access [36].

Finally, as stated at the end of the previous section, cells can be porated by cavitation bubbles. Inertial cavitation can locally induce strong shear flows along nearby surfaces [12]. When such a surface is covered by adherent cells the shear flow stretches the cell membrane until holes appear in the membrane [29, 37]. If the damage is to great the cell will die but with limited poration of the membrane the cell can survive and even repair the holes after some time. In the intervening time the cell membrane is permeable to any foreign materials that are in solution or suspension near the cell. Because up till now these cavitation bubbles were in general created using shockwaves this method of cell permeabilization is called sonoporation.

Previous experiments have shown that sonoporation works, but also demonstrated the limited amount of control on the experimental parameters [29]. The passing shockwave creates a whole cloud of bubbles of

varying sizes and at arbitrary positions inside the focal volume [38] resulting in random patterns of uptake [29]. This made it hard to find any link between the porated cells and the bubble responsible.

1.3 Micro fluidics

Microfluidics hold the potential to revolutionize the field of biology and chemistry, using less space and reagents and allowing for many experiments to be conducted simultaneously [39]. But there are some problems which obstruct a direct miniaturization of large scale fluid handling systems. In fluid dynamics there are always a lot of different effects acting and competing at the same time. One example is viscosity and inertia, where viscosity is mainly a fluid specific parameter inertia depends for a large part on the characteristic size and speed of the flow.

This competition between the two is expressed by the Reynolds number, which is inertial effects divided by viscous effects, and is larger than 1 for most everyday flows making them inertial flows. Only liquids with very high viscosity such as for example paint or honey are dominated by viscosity on these scales but when going down to microfluidic scales almost all flows are viscous. This regime where inertia has no effect is called the Stokes regime and is characterized by fully reversible flows making things we normally take for granted, like mixing or pumping, a engineering challenge [40].

Recently it was demonstrated that cavitation bubbles are fast enough to create jets, vortices and other non-reversible flows [41] and that these bubbles can indeed be use for mixing in microfluidics [42].

1.4 Thesis outline

The main aim of this thesis is cell membrane permeation through cavitation and this is discussed in the first two chapters. Chapter 2 deals with the wall shear stress induced by a cavitation bubble close to a wall. It is this wall shear stress that is responsible for the cell membrane permeation. Actual transfection experiments and the dependence on the distance of the bubble to the wall are shown in chapter 3.

Chapter 4 investigates wether cavitation bubbles can also porate and manipulate cells in a lab-on-a-chip device. The strong collapse of these planar microfluidic bubbles inspired the further study of cavitation in these

geometries. This resulted in a cavitation induced microfluidic pump which is described in chapter 5 and a study on a 1 dimensional cavitation bubble in the center of a micro capillary (chapter 6) and near one end of the capillary (chapter 7) where the expanding bubble creates a micro jet.

References

[1] M. Brenner, S. Hilgenfeldt, and D. Lohse, "Single-bubble sonoluminescence," *Rev. Mod. Phys.* **74**, pp. 425 (2002).

[2] L. Rayleigh, "On the pressure developed during the collapse of a spherical cavity," *Phil. Mag.* **34**, pp. 94 (1917).

[3] C. Brennen, *Cavitation and Bubble Dynamics* (Oxford University, Oxford, 1995).

[4] T. B. Benjamin and A. T. Ellis, "The Collapse of Cavitation Bubbles and the Pressures thereby Produced against Solid Boundaries," *Philos. Trans. R. Soc. Lond. A* **260**, pp. 221 (1966).

[5] M. S. Plesset and R. B. Chapman, "Collapse of an initially spherical vapour cavity in the neighbourhood of a solid boundary.," *J. Fluid Mech.* **47**, pp. 283 (1971).

[6] A. Vogel, W. Lauterborn, and R. Timm, "Optical and acoustic investigations of the dynamics of laser-produced cavitation bubbles near a solid boundary," *J. Fluid Mech.* **206**, pp. 299 (1989).

[7] B. W. Zeff, B. Kleber, J. Fineberg, and D. P. Lathrop, "Singularity dynamics in curvature collapse and jet eruption on a fluid surface," *Nature* **403**, pp. 401 (2000).

[8] A. Philipp and W. Lauterborn, "Cavitation erosion by single laser-produced bubbles," *J. Fluid Mech.* **361**, pp. 75 (1998).

[9] D. Silberrad, "Propeller erosion," *Engineering* pp. 33–35 (1912).

[10] R. E. A. Arndt, "Cavitation in fluid machinery and hydraulic structures," *Ann. Rev. Fluid Mech.* **13**, pp. 273 (1981).

[11] D. Krefting, R. Mettin, and W. Lauterborn, "High-speed observation of acoustic cavitation erosion in multibubble systems," *Ultrason. Sonochem.* **11**, pp. 119 (2004).

[12] C. D. Ohl, M. Arora, R. Dijkink, V. Janve, and D. Lohse, "Surface cleaning from laser-induced cavitation bubbles," *Appl. Phys. Lett.* **89**, pp. 74102 (2006a).

[13] V. S. Moholkar, M. M. C. G. Warmoeskerken, C. D. Ohl, and A. Prosperetti, "Mechanism of mass-transfer enhancement in textiles by ultrasound," *AIChE J.* **50**, pp. 58 (2004).

[14] K. Xu, R. Vos, G. Vereecke, G. Doumen, W. Fyen, P. W. Mertens, M. M. Heyns, C. Vinckier, J. Fransaer, and F. Kovacs, "Fundamental study of the removal mechanisms of nano-sized particles using brush scrubber cleaning," *J. Vac. Sci. Technol. B* **23**, pp. 2160 (2005).

[15] G. W. Gale and A. A. Busnaina, "Removal of particulate contaminants using ultrasonics and megasonics: A review," *Part. Sci. Technol.* **13**, pp. 197 (1995).

[16] F. Holsteyns, Ph.D. thesis, K. U. Leuven, Belgium (2008).

[17] P. R. Gogate, "Application of cavitational reactors for water disinfection: Current status and path forward," *J Environ. Manage.* **85**, pp. 801 (2007).

[18] P. Plaisier, R. W. van der Hul, O. T. Terpstra, and H. A. Bruining, "Current role of extracorporeal shockwave therapy in surgery," *Br. J. Surg.* **81**, pp. 174 (1994).

[19] W. Eisenmenger, "The mechanisms of stone fragmentation in ESWL," *Ultrasound Med. Biol.* **27**, pp. 683 (2001).

[20] S. Zhu, F. H. Cocks, G. M. Preminger, and P. Zhong, "The role of stress waves and cavitation in stone comminution in shock wave lithotripsy," *Ultrasound Med. Biol.* **28**, pp. 661 (2002).

[21] M. R. Bailey, V. A. Khokhlova, O. A. Sapozhnikov, S. G. Kargl, and L. A. Crum, "Physical mechanisms of the therapeutic effect of ultrasound (a review)," *Acta Physica* **49**, pp. 369 (2003).

[22] C. C. Coussios and R. A. Roy, "Applications of Acoustics and Cavitation to Noninvasive Therapy and Drug Delivery," *Ann. Rev. Fluid Mech.* **40**, pp. 395 (2008).

[23] F. Wu, Z. B. Wang, W. Z. Chen, J. Z. Zou, J. Bai, H. Zhu, K. Q. Li, F. L. Xie, C. B. Jin, H. B. Su, et al., "Extracorporeal focused ultrasound surgery

for treatment of human solid carcinomas: early chinese clinical experience," *Ultrasound Med. Biol.* **30**, pp. 245 (2004).

[24] S. Madersbacher, C. Kratzik, and M. Marberger, "Prostatic tissue ablation by transrectal high intensity focused ultrasound: histological impact and clinical application," *Ultrasonics Sonochemistry* **4**, pp. 175 (1997), fifth Meeting of the European Society of Sonochemistry.

[25] A. Blana, S. Rogenhofer, R. Ganzer, J. C. Lunz, M. Schostak, W. F. Wieland, and B. Walter, "Eight Years' Experience With High-Intensity Focused Ultrasonography for Treatment of Localized Prostate Cancer," *Urology* **72**, pp. 1329 (2008).

[26] G. ter Haar and C. Coussios, "High intensity focused ultrasound: Physical principles and devices," *Int. J. Hyperthermia* **23**, pp. 89 (2007).

[27] M. Pernot, J. F. Aubry, M. Tanter, J. L. Thomas, and M. Fink, "High power transcranial beam steering for ultrasonic brain therapy," *Phys. Med. Biol.* **48**, pp. 2577 (2003).

[28] J. Zabner, A. J. Fasbender, T. Moninger, K. A. Poellinger, and M. J. Welsh, "Cellular and Molecular Barriers to Gene Transfer by a Cationic Lipid," *J. Biol. Chem.* **270**, pp. 18997 (1995).

[29] C. D. Ohl, M. Arora, R. Ikink, N. de Jong, M. Versluis, M. Delius, and D. Lohse, "Sonoporation from jetting cavitation bubbles," *Biophys. J.* **91**, pp. 4285 (2006b).

[30] X. Gao, K. S. Kim, and D. Liu, "Nonviral gene delivery: what we know and what is next," *AAPS J.* **9**, pp. E92 (2007).

[31] A. El-Aneed, "An overview of current delivery systems in cancer gene therapy," *J. CONTROL. RELEASE* **94**, pp. 1 (2004).

[32] C. H. Su, H. I. Yeh, C. J. Y. Hou, and C. H. Tsai, "Nonviral technologies for gene therapy in cardiovascular research," *Int. J. Gerontol.* **2**, pp. 35 (2008).

[33] J. Gehl, "Electroporation: theory and methods, perspectives for drug delivery, gene therapy and research," *Acta Physiol. Scand.* **177**, pp. 437 (2003).

[34] K. Y. Ng and Y. Liu, "Therapeutic ultrasound: its application in drug delivery," *Med. Res. Rev.* **22**, pp. 204 (2002).

[35] N. S. Yang, J. Burkholder, B. Roberts, B. Martinell, and D. McCabe, "In vivo and in vitro gene transfer to mammalian somatic cells by particle bombardment," *Proc. Natl. Acad. Sci. USA* **87**, pp. 9568 (1990).

[36] S. Somiari, J. Glasspool-Malone, J. J. Drabick, R. A. Gilbert, R. Heller, M. J. Jaroszeski, and R. W. Malone, "Theory and in vivo application of electroporative gene delivery," *Mol. Ther.* **2**, pp. 178 (2000).

[37] K. R. Rau, P. A. Quinto-Su, A. N. Hellman, and V. Venugopalan, "Pulsed laser microbeam-induced cell lysis: time-resolved imaging and analysis of hydrodynamic effects," *Biophys. J.* **91**, pp. 317 (2006).

[38] M. Arora, L. Junge, and C. D. Ohl, "Cavitation cluster dynamics in shock-wave lithotripsy: part 1. free field," *Ultrasound Med. Biol.* **31**, pp. 827 (2005).

[39] T. M. Squires and S. R. Quake, "Microfluidics: Fluid physics at the nanoliter scale," *Rev. Mod. Phys.* **77**, pp. 977 (2005).

[40] E. M. Purcell, "Life at low Reynolds number," *Am. J. Phys.* **45**, pp. 3 (1977).

[41] E. Zwaan, S. L. Gac, K. Tsuji, and C. D. Ohl, "Controlled cavitation in microfluidic systems," *Phys. Rev. Lett.* **98**, pp. 254501 (2007).

[42] A. N. Hellman, K. R. Rau, H. H. Yoon, S. Bae, J. F. Palmer, K. S. Phillips, N. L. Allbritton, and V. Venugopalan, "Laser-Induced Mixing in Microfluidic Channels," *Anal. Chem.* **79**, pp. 4484 (2007).

2

Measurement of cavitation induced wall shear stress [‡]

The wall shear stress from cavitation bubbles collapsing close to a rigid boundary is measured with a constant temperature anemometer. The bubble is created with focused laser light and its dynamics is observed with high-speed photography. By correlating the frames, a hydrophone signal, and the wall shear stress we find that the highest stresses are created after the impact of the jet, during its radial spreading on the surface. The maximum of the wall shear stress varies with the power of -2.75 as a function of the distance from the jet impact and in accordance with the prediction for a steady wall impinging jet. The highest amplitude of the signal of the wall shear stresses is found for bubbles oscillating close to the boundary and reaches more than 3 *kPa. Additionally, it contains a slowly decaying weaker component which may be generated by an expanding vortex ring.*

2.1 Introduction

Ultrasonic water bathes spotted in many labs, at opticians, and jewelers clean surfaces efficiently from attached contaminants. It is generally ac-

[‡]Published as: Rory Dijkink and Claus-Dieter Ohl, *Measurement of cavitation induced wall shear stress*, Appl. Phys. Lett. **93**, pp. 254107 (2008).

cepted that *not* the acoustic sound field directly but the cavitation bubbles driven by the sound field are responsible for surface cleaning [1, 2, 3]. With cleaning we refer to the process by which an attached dirt particle is at first *dislocated* and then *dragged* along with the flow. Yet, rigid boundaries on which the particle adhere limit the strength of the dragging flow: the no-slip boundary condition dictates that the lateral velocity has to ultimately drop to zero on the surface. Thus smaller dirt particles are more difficult to remove as they require a larger velocity gradient. Submicrometer sized particles are of major concern in the ultraclean processing of silicon surfaces in the chip industry [4]. Their safe to operate cleaning regime is bounded by the structural stability of nanometer sized up-patterns of modern processor and memory designs. Thus for defect free cleaning it is of utmost importance to understand the acting forces and adjust them within the structural stability limits of the patterns. In an effort to understand more on the flow we report in this chapter on the time dependent velocity gradient at the surface for a single but "well controlled" cavitation bubble.

Generally, the flow strength tangent to the wall is expressed by the wall shear stress, τ_w. It is the wall normal gradient of the velocity, U, at the wall, $y = 0$, scaled by the dynamic viscosity of water, $\mu = 10^{-3}$ Pa s:

$$\tau_w = \mu \left. \frac{dU}{dy} \right|_{y=0} \tag{2.1}$$

To correlate this quantity with the bubble dynamics we make use of high-speed photography. In our previous work [5] we revealed that the particles on the surface are accelerated only during a very brief moment of the bubble oscillation phase; this is after a re-entrant jet has developed [6], which pierces through the lower bubble interface, and impinges onto the rigid wall [7, 8].

2.2 Experimental setup

Ultrasound generated cavitation bubbles appear statistically and are difficult to control. Therefore, we study the flow from a single bubble generated at the focus of a pulsed laser which allows for high spatial and temporal control. A frequency doubled Nd:YAG laser (Solo PIV, New Wave, $\lambda = 532\,\mathrm{nm}$, pulse duration $6\,\mathrm{ns}$) is focused at a distance h from the boundary, see Fig. 2.1. The origin of the cartesian xy-coordinate system is positioned

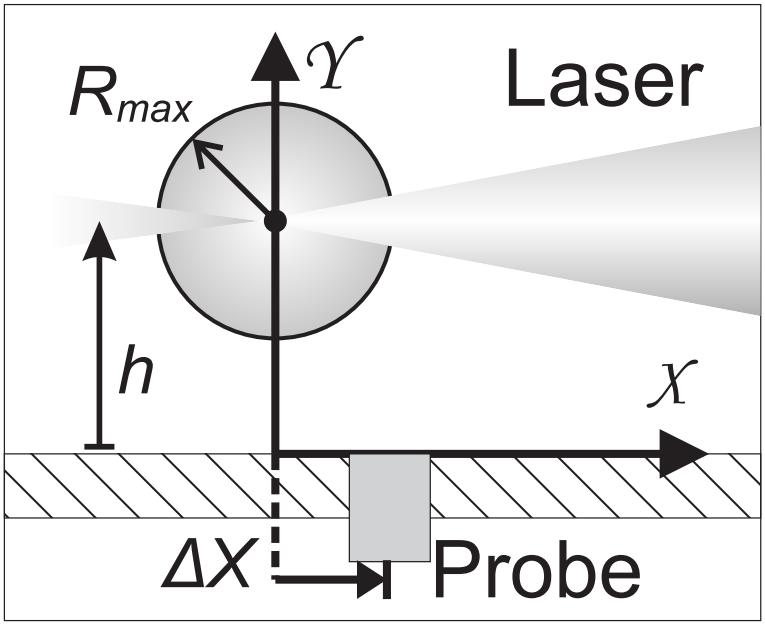

Figure 2.1: Sketch of the geometry of the experiment to correlate the wall shear stress with the bubble dynamics. The bubble is generated at the laser focus at xy-position $(0, h)$. The center of the probe is located at $(\Delta X, 0)$

on the wall with the y-axis pointing up towards the bubble center as indicated in Fig. 2.1. To measure the wall shear stress we make use of a resistive thin film sensor (model 55R46 from Dantec Dynamics, Skovlunde, Denmark) located at a distance Δx from the origin. The dimensions of the active sensor area are $750\,\mu m \times 200\,\mu m$. The probe is connected to a anemometer (CTA, Streamline, Dantec Dynamics); and its working principle is based on the cooling of the sensor by advection [9]. As it operates in a constant temperature mode, thus the signal from the CTA is proportional to the current needed to stabilize the temperature. Internally the CTA uses a feedback loop with an upper frequency of 50kHz supplying a constant current through a Wheatstone bridge; the sensor is part of one arm of the bridge. A relation resembling King's law [9] can be derived exploiting the similarity between a temperature and a velocity boundary layer. This leads to

$$E^2 = A + B\tau_w^{1/n}, \tag{2.2}$$

where E is the measured voltage and τ_w the wall shear stress. From calibration measurements in channel flows we determine the constants A, B, and n for wall shear stress 0.05 Pa$< \tau_w <$ 10 Pa (see section 2.2.1).

The sensor is flush mounted in a rigid boundary which is connected to a two-axis translation stage to adjust the vertical, h, and the lateral position, Δx, with sufficient accuracy, see Fig. 2.1. The bubble dynamics is recorded at the same time with the wall-shear stress measurements with a high speed camera at moderate resolution (Photron APX, 128 X 96 pixels and 90.000 frames/s). Additionally, the acoustic signals from the bubble nucleation and later collapses are probed with a hydrophone (Grass 10CH, Holte, Denmark, positioned about 15mm from the laser focus). All three signals, the wall shear stress, the frame synchronization signal from the camera, and the acoustic emission are recorded simultaneously. Because of the high reproducibility of laser induced bubbles showing with the same laser power and acoustic signature we present in this chapter frames taken at higher spatial resolution and with improved illumination using a HPV-1 camera (Shimadzu Europa GmbH, Duisburg, Germany) at a resolution of 312 X 260$pixels$ at 250.000$frames/s$.

2.2.1 Probe calibration

For the calibration our CTA-probe was flush mounted it in the top wall of a microchannel (μ-Slide VI, ibidi, Munich, Germany). This microchannel has a rectangular cross-section of 3.8mm by 0.4mm and the shear rates are calculated based on a fully developed laminar flow. For zero flow no shear exists gives and it is immediately clear that $A = E_0^2$ or the heat loss from the probe due to radiation. B and n still remain unknown but can be obtained through a series of calibration measurements where a shear flow with known strength is imposed on the probe. The channel is hooked up to a syringe pump to impose a pressure driven flow of constant velocity over a period of time. The shear is calculated from the flow velocity and plotted against the increase in the quadratic voltage applied across the probe $(E^2 - E_0^2)$ on a double log scale(see figure 2.2). The inclination of the line gives us n and the offset results in B thus fully defining the response of our probe.

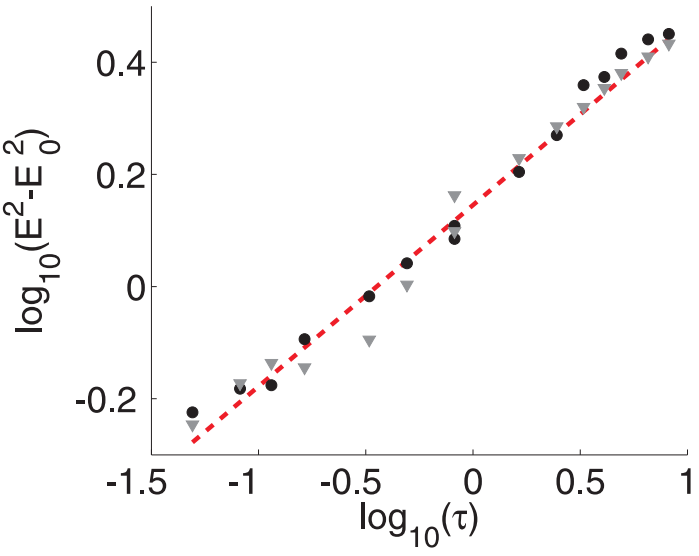

Figure 2.2: Double logarithmic plot of the data from the shear probe plotted against the calculated shear stress which is imposed on the probe. The two sets of measurements are represented by the black dots and the grey triangles and the dashed red line denotes the fitted curve used to get the constants needed for the calibration of the probe.

2.3 Results and discussion

A data set from one experiment is shown in Fig. 2.3. It consists of three rows: on the top selected frames from the high speed recording, below the calibrated wall shear stress from the CTA, and at the bottom the acoustic signal recorded with the hydrophone. The cavitation bubble expansion and collapse cycle with a maximum bubble radius of 0.75 mm lasts for 143 µs. The first bubble expansion takes place in the first 65 µs during which the bubble flattens at the proximal side to the boundary and develops a spherical shape at the distant side. During shrinkage more liquid rushes in from the top leading to a faster shrinkage of the upper part of the bubble which is nicely visible at time 133 µs. The bubble reaches a minimum volume very close to this frame which is visible in the acoustic emission in the second row of Fig. 2.3 at time 143 µs. More acoustic emissions are visible, the first spike at time 0 is generated during the genera-

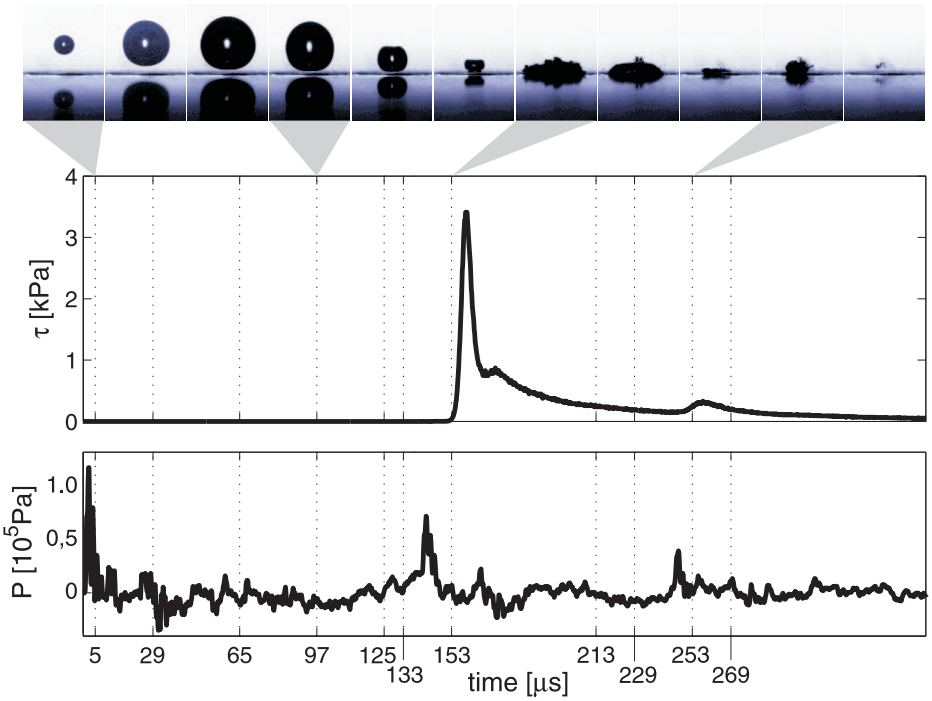

Figure 2.3: Simultaneous measurement of the bubble shape, the acoustic emission, and the shear stress exerted on the boundary. The selected frames in the top row present the bubble pulsation close to a boundary. The bottom part of each frame is a reflection from the boundary and helps to locate the position of the wall. The bubble collapses non-spherical symmetrical with the formation of a reentrant jet flow. During reexpansion the bubble deforms into a pan-cake shape. Acoustic emission (third row) is recorded during the bubble creation and bubble collapses; yet, intense shearing of the liquid close to the boundary (second row, measured at the marked position in the first frame) is only observed 17 μs after the first collapse. Thus maximum wall shear stress is not occurring during bubble collapse but when the radial spreading jet flows across the sensor. The maximum bubble radius is 0.75mm and the bubble is created 0.8mm away from the boundary. The dashed vertical lines indicate the time of the picture taken and shown in the top row.

tion of the bubble and the third spike (at time 246 μs) during the second bubble collapse. Other lower amplitude spikes come from reflections of the pressure waves and are an acoustic signature of the container. As a side note, the acoustic propagation time from the laser focus to the hydrophone has been determined by correlating the acoustic signal with a negative spike recorded by the hot film sensor; this is presumably caused by mild but rapid heating of the probe through the plasma emission from the focused laser pulse.

During the first bubble oscillation period - from bubble creation up to its first collapse- the recorded wall shear stress remains below 1 Pa and it is not detectable on the scale in Fig. 2.3. We find that the wall shear stress increases only after the acoustic emission of the collapse is recorded. A maximum in the wall shear stress of 3.5 kPa is reached 17 μs after the collapse. This amplitude is reached within 3 μs, likely limited by the bandwidth of the CTA. The shear stress signal drops quickly afterwards, reaches a second maximum and then decays exponentially on a slow timescale. Also, a third local maximum is visible right after the second bubble collapse at 246 μs. We explain the strong peak after the bubble collapse with the jet spreading radially on the surface. As the sensor is 0.25 mm away from the impact/stagnation point of the jet the delay between both reflects the travel time of the jet to the sensor. Assuming that the bubble collapse and the jet impact are occurring within a few microseconds we can estimate the velocity of the radial spreading jet to be around 15 m/s which is in the expected range [10]. The slowly decaying component of the later signal is likely caused by the expanding vortex ring [11]. However, we have no simple explanation for the second maximum and probably can only understand this when comparing with a fluid dynamics simulation. Please also note, that the sensor can only measure the absolute value of the wall shear stress, e.g. it can't detect flow reversal.

The results of many of such experiments are summarized in Fig. 2.4. For the further analysis the initial distance from the wall and the lateral location of the probe are now non-dimensionalized with the maximum bubble radius R_{max}, leading to the probe distance $\eta = h/R_{max}$ and stand-off parameter $\gamma = x/R_{max}$, respectively.

Outside the impact region of the jet the wall shear stress decreases with distance simply due to mass conservation. The upper group in Fig. 2.4 quantifies the drop of the wall shear stress by plotting the maximum of the signal as a function of η for one stand-off parameter $\gamma = 1.0 \pm 0.1$ (see section 2.3.1 for a discussion of the effect of spatial averaging due to a finite probe size). The wall shear stress drops within two bubble radii to

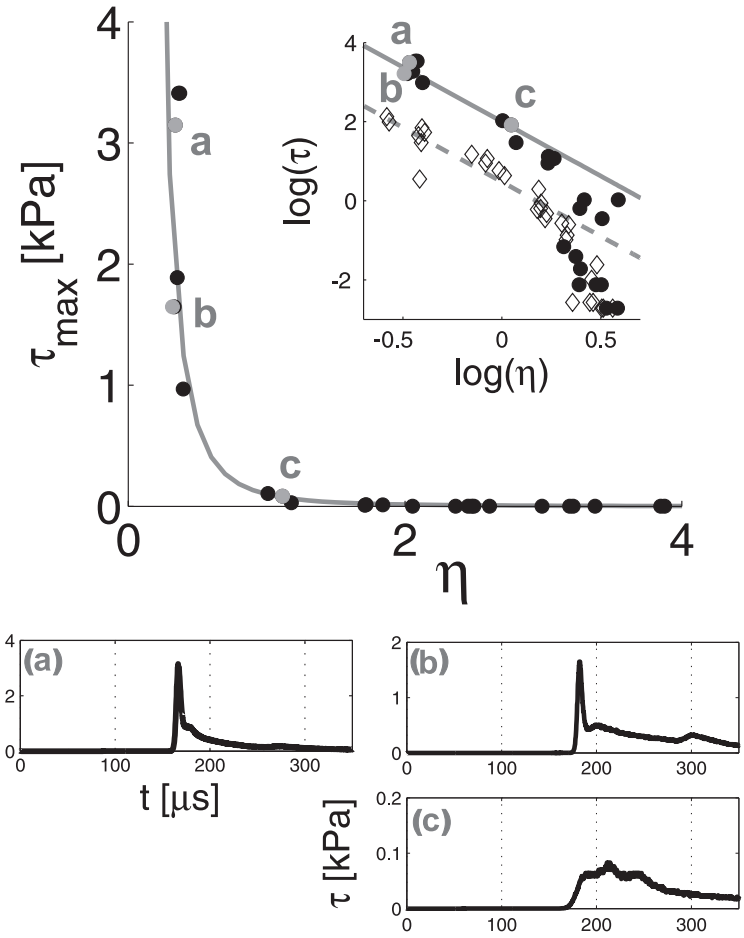

Figure 2.4: In the upper part of the figure the maximum of the wall shear stress as a function of the distance η for a stand-off distance of $\gamma = 1.0$ is plotted. At the three marked positions a, b and c the time resolved signals are displayed below. The inset of the upper plot depicts the wall shear stress double logarithmically and compared to the Glauert solution [12] with a similarity exponent of -2.75 ($\bullet$ for $\gamma = 1.0 \pm 0.1$ and $\diamondsuit$ for $\gamma = 2.5 \pm 0.2$).

about 10% from its maximum value. This supports our previous finding that bubble induced cleaning is occurring on circular patches with radii comparable to the bubble [5, 13]. Three example signals named a to c are depicted in the lower rows. Close to the impact point (a and b in Fig. 2.4) the amplitude of the signal changes, yet the shape remains similar. Further away (c in Fig. 2.4) the initial peak is strongly reduced, i.e. its magnitude is similar to the expanding vortex ring. By plotting the maximum of the wall shear stress double logarithmically we can test for a power law dependency. Glauerts similarity solution [12] of the Navier Stokes equations of a steady and infinitely thin wall jet predicts a scaling of $\tau \propto \eta^{-2.75}$. In the inset of Fig. 2.4 the two lines have a slope of -2.75, the solid line goes through data points for $\gamma = 1.0$ and the dashed line through a second set of data with $\gamma = 2.5$. We find good agreement between the steady similiarity solution and the measurements from an impulsive wall jetting flow. For larger distances η the signal of the wall shear probe is very weak leading to noisier measurements. Also we expect a transition of the laminar boundary to a turbulent one.

2.3.1 Spatial shear averaging

The size of the measuring area of the CTA-probe is quite significant when compared to the sizes of our bubbles (The bubbles have maximum radii of around $0.75\mathrm{mm}$ and the hotfilm is $0.2\mathrm{mm}$ wide). This can result in sig-

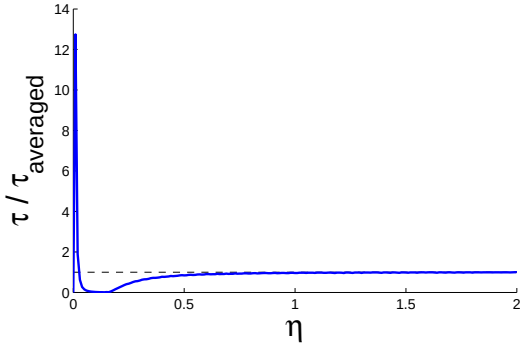

Figure 2.5: The exact solution of $\tau = 100\eta^{-2.75}$ (in blue) is spatially averaged over an area of $\Delta\eta = 0.32$ (curve in red) to get an estimate of the error introduced into our measurements by the size of the probe.

nificant spatial averaging of the shear stress signal. To get some idea of how large an impact it has a numerical study was done where the fit for the $\gamma = 1$ from figure 3 of the main paper is taken as the reference signal. This signal is then averaged over η over a length comparable to the width of the probe's hotfilm ($\Delta\eta = 0.32 \simeq 2.4\text{mm}$). Both the reference curve and the spatially averaged result are plotted in figure 2.5 in blue and red respectively.

2.4 Conclusion

In summary we have shown, that a millimeter sized bubble collapsing close to a boundary creates very intense strong shear stress. A wall shear stress of 3.5 kPa relates to a spatial acceleration of the flow from zero at the boundary to 3.5 m/s at only a distance of 1 μm. The bandwidth limited temporal measurements reveal that this shear stress increases from a few Pascals to 3.5kPa within 3 μs or less. This remarkable fluid dynamics has its origin in the symmetry breaking of the spherical flow by the boundary leading to the focused and high-speed jet.

References

[1] F. Holsteyns, Ph.D. thesis, K. U. Leuven, Belgium (2008).

[2] D. Krefting, R. Mettin, and W. Lauterborn, "High-speed observation of acoustic cavitation erosion in multibubble systems," *Ultrason. Sonochem.* **11**, pp. 119 (2004).

[3] V. S. Moholkar, M. M. C. G. Warmoeskerken, C. D. Ohl, and A. Prosperetti, "Mechanism of mass-transfer enhancement in textiles by ultrasound," *AIChE J.* **50**, pp. 58 (2004).

[4] K. Xu, R. Vos, G. Vereecke, G. Doumen, W. Fyen, P. W. Mertens, M. M. Heyns, C. Vinckier, J. Fransaer, and F. Kovacs, "Fundamental study of the removal mechanisms of nano-sized particles using brush scrubber cleaning," *J. Vac. Sci. Technol. B* **23**, pp. 2160 (2005).

[5] C. D. Ohl, M. Arora, R. Dijkink, V. Janve, and D. Lohse, "Surface cleaning from laser-induced cavitation bubbles," *Appl. Phys. Lett.* **89**, pp. 74102 (2006a).

[6] B. W. Zeff, B. Kleber, J. Fineberg, and D. P. Lathrop, "Singularity dynamics in curvature collapse and jet eruption on a fluid surface," *Nature* **403**, pp. 401 (2000).

[7] E. A. Brujan, G. S. Keen, A. Vogel, and J. R. Blake, "The final stage of the collapse of a cavitation bubble close to a rigid boundary," *Phys. Fluids* **14**, pp. 85 (2002).

[8] M. S. Plesset and R. B. Chapman, "Collapse of an initially spherical vapour cavity in the neighbourhood of a solid boundary.," *J. Fluid Mech.* **47**, pp. 283 (1971).

[9] H. H. Bruun, *Hot-Wire Anemometry: Principles and Signal Analysis* (Oxford University Press, 1995).

[10] E. Klaseboer, "Private communication," (2008).

[11] T. B. Benjamin and A. T. Ellis, "The Collapse of Cavitation Bubbles and the Pressures thereby Produced against Solid Boundaries," *Philos. Trans. R. Soc. Lond. A* **260**, pp. 221 (1966).

[12] M. B. Glauert, "The wall jet," *J. Fluid Mech.* **1**, pp. 625 (1956).

[13] C. D. Ohl, M. Arora, R. Ikink, N. de Jong, M. Versluis, M. Delius, and D. Lohse, "Sonoporation from jetting cavitation bubbles," *Biophys. J.* **91**, pp. 4285 (2006b).

3

Controlled cavitation-cell interaction: trans-membrane transport and viability studies [‡]

Cavitation bubble dynamics close to a rigid surface gives rise to a rapid and transient fluid flow. A single bubble is created with a laser pulse at different stand-off distances from the rigid surface, where the stand-off distance γ *is defined by* $\gamma = h/R_{max}$*, with h being the initial distance and* R_{max} *being the maximum bubble radius. When the surface is covered with adherent cells, molecular delivery and cell detachment after single cavitation activity are observed at different locations. We find a maximum of cell detachment at a normalized stand-off distance of* $\gamma \sim 0.65$*. In contrast, the maximum of the molecular uptake is found when* γ *approaches* 0*. The single cavitation event has only little effect on the viability of cells in the non-detached area. We find apoptosis of cells only very close to the area of detachment and, additionally, the metabolism of the non-detached cells shows no pronounced difference compared to control cells according to an MTS assay. Thus, although the cavitation event is responsible for the detachment of cells, only few of the remaining cells undergo a permanent change.*

[‡]Published as: Rory Dijkink, Séverine Le Gac, Erwin Nijhuis, Albert van den Berg, István Vermes, André Poot and Claus-Dieter Ohl, *Controlled cavitationcell interaction: trans-membrane transport and viability studies*, Phys. Med. Biol. **53**, pp. 375-390 (2008).

3.1 Introduction

The effect of continuous and weak wall shear stress on adherent cells and their biological pathways is well documented in literature [1]. For higher flow velocities in the bulk, the wall shear stress increases and this eventually leads to the detachment and transport of cells with the flow. A transient and strong flow allows the exposure of cells to high levels of shear yet without their detachment. Recently, it was observed that this regime of short but high wall shear stress facilitates the uptake of non-membrane permeant molecules into the cells [2].

This finding might allow for developing strategies for the delivery of foreign and large molecules into cells. The necessary fast and transient flow is created with a cluster of vapor bubbles induced with an acoustic wave. By aiming the focused acoustic source close to a surface plated with adherent cells, bubbles can be generated in the vicinity of the cells. The bubbles expand rapidly within a few tens of microseconds to radii of 200 μm and above [2]. During the accelerated shrinkage of the bubbles being close to the cell-supporting surface the fluid flow is concentrated into a jet directed toward this surface [3, 4, 5]. This jet flow impacts onto the surface and then spreads radially on top of the adherent cells. With increasing radial distance from the point of jet impact on the surface we find cell detachment, cell death and molecular delivery. It is known that the size of the bubble and its distance from the boundary strongly affects the magnitude and duration of the flow close to the surface where the cells reside [6, 4]. Unfortunately, when vapor bubbles are nucleated with acoustic waves there is no control on the distance of the bubble with respect to the wall [7] and little on the number density and distance between bubbles [8].

The uncontrolled nature of this type of cavitation exposure to cells causes poor repeatability of the experiment. Thus, we were not able to quantify the molecular uptake and the viability of the cells after the bubble activity in previous studies [2] with respect to the bubble dynamics. This experimental shortcoming is now solved by utilizing a laser pulse to create a single bubble [9] close to the adherent cells. The usage of a focused laser pulse allows for controlling the start of the bubble pulsation, its position and its maximum size. This method enables parameter studies on the fluid dynamics and the effect on cells. In detail we report here on the radius of the cell detachment, cell morphology, molecular delivery, cell viability and induction of apoptosis. All of the data presented are from well-controlled and repeatable experiments involving a single-cavitation

event.

The chapter is organized as follows: firstly, the experimental set-up to generate and photograph single-cavitation events is presented. Secondly, cell cultivation, staining, confocal laser microscopy, and the viability MTS assay are introduced. In the results section we give an overview on the details of the bubble dynamics and related flow phenomena. Subsequently, the cell-detachment area and the amount of molecular uptake as a function of the stand-off distance are discussed. This section is succeeded with biological relevant studies on cavitation-induced apoptosis and cell viability. In the discussion the origin and the importance of the high speed flow generated close to the boundary on the observed biological effects are emphasized.

3.2 Materials and methods

3.2.1 Experimental set-up to create single-cavitation bubbles

Single millimeter sized cavitation bubbles are created by focusing pulsed laser light into a liquid. Therefore, we use an infrared Nd:YAG laser (New Wave Solo, Fremont, Ca, USA) at the fundamental wavelength of $1064\,\mathrm{nm}$ with a pulse duration of $7\,\mathrm{ns}$ and a pulse energy of approximately $16\,\mathrm{mJ}$. The laser light enters a cuvette from the top through an aberration minimized lens system, see figure 3.1. The cuvette is filled with a cell culture medium (Iscoves modified Dulbeccos medium, see below). The lens system is partly submerged and attached to a z-positioning stage. Thereby, the distance between the laser focus where the bubbles are created and the surface covered with adherent cells can be precisely adjusted. Adherent cells are plated onto the bottom surface of open eight-well plates arranged on a single microscope slide (µ-slide eight well, ibidi, Martinsried, Germany) which is submerged into the cuvette. This procedure allows, due to geometrical constraints, cavitation experiments in the central four wells while keeping the chamber slide submerged. The remaining outer wells are used as controls.

All walls (cell culture chambers, bottom of the cuvette and its side walls) are transparent to facilitate visual control and recording. Therefore, the set-up is equipped with two cameras. A double frame camera (Sensicam QE double shutter, PCO, Kehlheim, Germany) allows viewing from the side as illustrated in figure 3.1 to record the position of the bubble with respect to the cell layer. The second camera, a digital $4\,\mathrm{megapixel}$

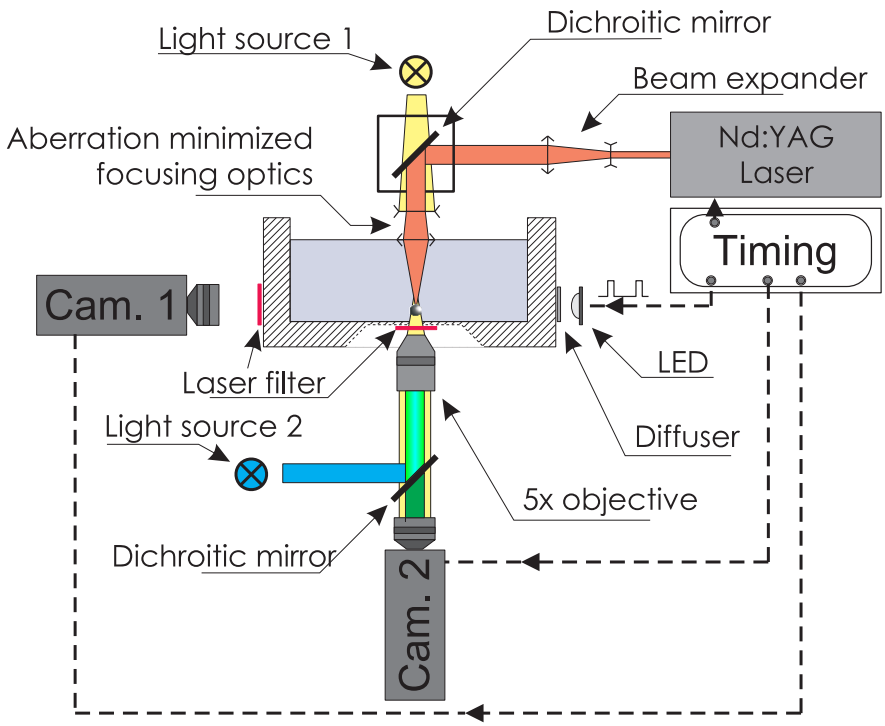

Figure 3.1: Experimental set-up used to generate single laser-induced cavitation bubbles close to adherent cells. The cavitation bubble is generated with an infrared laser pulse coming from the top into the medium-filled container and focused with a lens system. The upper dichroic mirror reflects the laser pulse but lets pass some light for illumination from the top. Cameras 1 and 2 record the bubble dynamics from aside and below, respectively. Side illumination is achieved with a bright light-emitting diode. Cells are grown in eight-well plates on a slide which is positioned on the transparent bottom of the container. An Hg lamp is also placed below the container for fluorescence measurements; this light source is used to excite the cells that have taken up a fluorescent dye.

still camera, is connected to the camera port of the inverted microscope (Axiovert CF 40, Zeiss, Goettingen, Germany) supporting the cuvette, and is used for fluorescence imaging.

3.2.2 Cell culture and preparation for cavitation experiments

Epidermal HeLa cells (derived from human cervix carcinoma) are grown in Iscoves modified Dulbeccos medium supplemented with 10% of fetal calf serum (FCS) and 1% antibiotic antimycotic (all supplements are obtained from Invitrogen, Breda, The Netherlands). Cultures are performed in a humidified incubator with a temperature of $37^{\circ}C$ and a CO_2 level of 5%. Tissue culture equipment is purchased from Nalge Nunc (Fisher Scientific B.V, Landsmeer, The Netherlands). Prior to the experiments, cells are seeded into the eight-well plates and grown overnight in an incubator to allow attachment of the cells to the surface and subsequently to reach an exponentially growing cell population. When $80-90\%$ cell confluency per well is obtained experiments were performed. The eight-well plate is gently submerged into the tank filled with serum-free and pre-heated culture medium.

3.2.3 Cell staining and imaging

Cell staining: Calcein. We investigate cell membrane permeabilization using the small fluorescent molecule calcein ($623\,mol wt$; maximum absorption at wavelength $\lambda_{exc} = 490nm$ and wavelength at maximum emission $\lambda_{em} = 515nm$) (Merck, Darmstadt, Germany). Calcein at a concentration of $1mgml^{-1}$ in a medium is gently injected into the wells after the slide has been submerged into the non-supplemented culture medium. After the cavitation experiment, the cells are thoroughly but also carefully washed with a fresh medium to remove the remaining calcein which causes a high level of background fluorescence.

Three-dyes cell staining. We study apoptosis using three cell staining dyes giving information on the cell state, namely TetraMethylRhodamine Ethyl ester, perchlorate (TMRE) ($\lambda_{exc} = 550nm$; $\lambda_{em} = 590nm$), Annexin V-Alexa Fluor 647 ($\lambda_{exc} = 650nm$; $\lambda_{em} = 665nm$) and YOPRO-1 ($\lambda_{exc} = 491nm$; $\lambda_{em} = 509nm$) (all from Molecular Probes, Invitrogen, Breda, The Netherlands). Cell staining is performed in a calcium-enriched medium ($2.5mMCaCl_2$) (calcium is required for binding of Annexin V to phosphatidylserine, PS, present on the outer membrane of ap-

optotic cells) supplemented with the dyes at the concentrations of 300nM, 0.5%v/v and 500nM for TMRE, Annexin V-Alexa Fluor 647 and YOPRO-1, respectively. We investigate two approaches (see results section): (i) either we wash cells and add fresh culture medium supplemented with calcium and the dyes after the cavitation experiment or (ii) we perform the experiments in a calcium-enriched culture medium (the tank was filled with calcium-enriched but not supplemented culture medium) and add the dyes at the end of the experiment.

Fluorescence microscopy. We use a microscope (Axiovert CF40, Carl Zeiss, Gottingen, Germany) with a 5× objective to photograph the calcein uptake. Fluorescence is excited with a mercury lamp (HBO 50, Carl Zeiss) and observed with an appropriate filter block (no. 09, Carl Zeiss, band pass BP excitation filter $450\text{nm} < \lambda < 490\text{nm}$, long pass LP emission filter $\lambda > 510\text{nm}$).

Confocal laser scanning microscopy (CLSM). Confocal laser scanning microscopy is performed on a Zeiss LSM 510-meta system. Excitation and filters are as follows: TMRE, $\lambda_{exc} = 543\text{nm}$, LP 560nm; Alexa Fluor 647, $\lambda_{exc} = 633\text{nm}$, LP 650nm; YOPRO-1, $\lambda_{exc} = 488\text{nm}$, BP $500 - 550\text{nm}$. A multi-track configuration is used in case of imaging with several dyes. Laser intensity is decreased to limit photo-bleaching; it is set at 5%, 4% and 10% of the maximum for 488nm, 543nm and 633nm, respectively.

Image analysis. The size of the bubble and its distance from the wall are determined from pictures taken during the maximum bubble expansion with the side viewing camera. The size of the cell depleted area is measured with image processing techniques. For this, bright field illumination of the individual wells gave the best contrast. The position of the laser focus is determined from bright continuum emission of the plasma. The magnification of the picture is obtained from geometrical features of the individual plastic wells.

Calcein uptake is measured from the fluorescent micrographs taken with a still color camera. After suitable image processing the area in each picture with positive cells (green fluorescent) and the average level of dye uptake as a function of the radial distance from the projected laser focus are determined. Image processing is done with the MATLAB/IP toolbox (The Mathworks, Natick, MA, USA).

3.2.4 MTS assay

Cell viability after exposure to a cavitation event is assessed through an MTS ($3-(4,5-dimethylthiazol-2-yl)-5-(3-carboxymethoxyphenyl)-2-(4-sulfophenyl)-2H-tetrazolium$, inner salt) assay. Directly following the cavitation experiment wells are washed. MTS is added according to the CellTiter 96 AQueos 96 proliferation assay protocol (Promega, WI, USA) 1 hour before recording the absorbance. It should be noted that when the reagent is added without washing the wells (i.e. removing the medium where the experiment is performed) the redox reaction on which the MTS assay relies is hindered. This is thought to be due to a high amount of chemicals that are released in the medium due to cell lysis and necrosis upon exposure to the cavitation bubble. The MTS cell proliferation assay is performed 0, 2, 4 and 24 h after cavitation exposure. During this time the plates are incubated at 37°C and 1 h before recording the absorbance the MTS reagent was added. The MTS reagent is converted by dehydrogenase enzymes in metabolically active cells into soluble formazan whose absorbance is read at $492nm$ using an automated Victor plate reader. This absorbance value is directly proportional to the amount of viable cells. Similar measurements are concomitantly conducted on control cells that have also undergone the same treatment, i.e. seeded in eight-well chambers, taken out of the incubator for a while, submerged into the same growth medium, but not exposed to cavitation bubbles.

3.3 Results

The usage of a laser to create single cavitation bubbles allows exposing adherent cells to a reproducible controlled flow. One of the important experimental parameters for the cavitationcell interaction is the distance between the bubble center and the substrate on which the cells were grown. This so-called stand-off distance γ is defined by $\gamma = h/R_{max}$, where h is the initial distance of the bubble center to the wall and R_{max} is the maximum radius of the bubble. In the potential flow limit bubbles with the same stand-off distance exhibit similar dynamics. Three examples of the bubble dynamics for different stand-off distances are presented in figure 3.2. Here, the distance of the bubble nucleation point from the boundary is increased from top (figure 3.2(a)) to bottom (figure 3.2(c)) and for each distance five frames from a high speed sequence have been selected.

Figure 3.2(a) depicts a bubble very close, stand-off distance $\gamma = 0.1$, to the boundary which is at the lower part of the individual frames. Here, the bubble expands resembling nearly a hemisphere; it shrinks, and then collapses at about 200μs after its creation. During re-expansion the bubble develops into a cigar shape upward directed structure.

When the bubble is created at some distance away from the boundary, see figure 3.2(b) with $\gamma = 0.9$, the upper side of the bubble again expands into a spherical shape, whereas the lower side facing the boundary is flattened. During shrinkage the bubble obtains an approximate triangular shape in projection and a jet flow is generated starting from the top more curved part of the bubble and being accelerated toward the boundary. The jet flow is not visible in this sequence but responsible for the toroidal bubble in the last frame of the high-speed sequence of figure 3.2(b). Here, after the impact and spreading of the jet flow, a vortex ring is generated, which stabilizes the re-expanding bubble into a torus.

In contrast, the jet flow becomes, although indirectly, visible in the sequence at the largest stand-off distance $\gamma = 2.0$. The bubble expands and collapses almost spherically; yet again a thin and fast jet flow is created which is visualized by the shape of the re-expanding bubble on top of this jet flow. The jet flow causes the cusp shape at the lower bubble side, and the jet impacts around t = 300μs on the surface. Additionally, the bubble moves toward the boundary and presumably, the second collapse of the bubble (not shown here) takes place on the boundary.

It has been observed that detachment of cells occurs after the jet has impacted on the wall [7, 2] and that the cells are washed away during the radial spreading of the jet on the surface. Thus, it is expected that the velocity of the jet at impact is an important parameter for cell detachment. Further, it has been found that the detachment region continues to grow even after the bubble has ceased. It is very probable that the later detachment is caused by a vortex ring fed by the jet flow.

From simple arguments the jet impact velocity must possess at least one global maximum between $\gamma = 0$ and $\gamma = \infty$. A bubble collapsing very far from the boundary will not develop a jet or the jet has died out before it reaches the wall. A bubble which expands as a hemisphere, $\gamma = 0$, will - due to symmetry reasons - not develop a jet flow. Indeed, the measurements of Philipp and Lauterborn [10] show a maximum impact velocity at a stand-off distance of $\gamma \sim 0.7$. Thus as we assume that the detachment and the impact velocity of the jet are correlated, we would expect a maximum in the detachment area for $\gamma \sim 0.7$ as well.

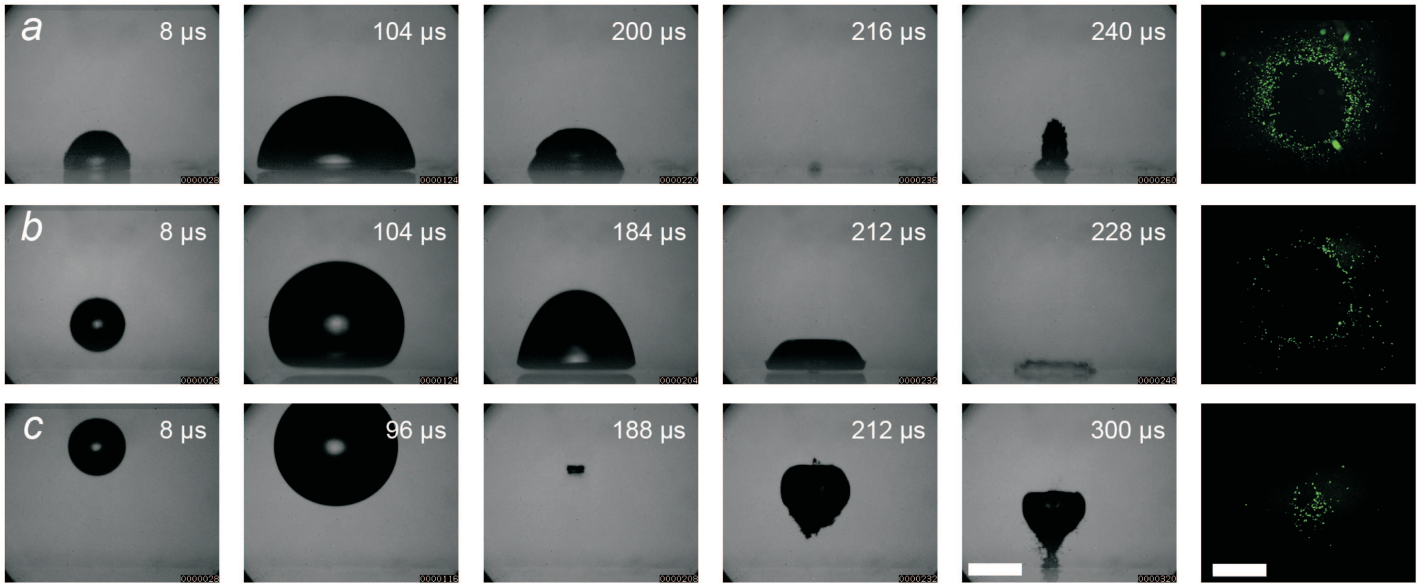

Figure 3.2: Series of frames showing the collapse of a cavitation bubble for various stand-off distances and illustrating the influence of the stand-off distance on the bubble oscillation regime and the calcein uptake (last picture on the right). (A) $\gamma = 0.1$, (B) $\gamma = 0.9$ and (C) $\gamma = 2.0$. Pictures are taken from the side using a high-speed camera (250kfps) starting from the creation of the bubble at time 8$\mu\mathrm{s}$. The rigid boundary is located at the bottom of the individual frames. The two bars both with a length of 1mm display that both the frames from the high-speed recording and the fluorescence have the same magnification.

3.3.1 Area of cell detachment

We find no cell detachment for stand-off distances larger than $\gamma > 2.0$. Therefore, the reported γ values in this work are limited to the range between 0 and 2.0. All the bubbles have an average maximum radius of $1.0\mathrm{mm} \pm 15\%$. The three fluorescent micrographs in figure 3.2 illustrate the areas of cell detachment together with the high-speed sequence as a function of the standoff distance. When the bubble is created far from the cell layer little or no cell detachment is observed. With decreasing distance the cell detachment area increases. Interestingly, the detachment area reaches a maximum at $\gamma \sim 0.65$, and then the area decreases again yet to a finite area as γ approaches 0. The reproducibility in this experiment is demonstrated by the scatter in the data points in figure 3.3 e.g., we achieve a reproducibility of the detachment radius of $10 - 20\%$. The radius of the detachment area for small stand-off distances is in the order of the maximum bubble radius $\mathrm{R_{max}}$, which is in agreement with the findings in our previous work [2]. Interestingly, both the detachment area and the impact velocity of the jet obtain a maximum at approximately the same stand-off distance of $\gamma \sim 0.7$. This agrees with the previous findings of Junge et al [7] and Ohl et al [11, 2] that the jet is responsible for a strong boundary layer flow able to detach the cells. Interestingly, detachment is still found for $\gamma \sim 0$ thus when no flow-focusing phenomenon is expected. Here, presumably the boundary layer breaks the symmetry of the hemispherical inflow during the last collapse phase and a net flow from the top prevails which might be responsible for the observed cell detachment.

3.3.2 Molecular delivery into cells

Next, we investigate the cavitation-induced uptake of foreign molecules through the cell membrane. This uptake is probed with the fluorescent molecule calcein (623Da, Stokes-radius 0.68nm) which is added to the medium before the cavitation event. After cavitation exposure cells are carefully washed and the calcein uptake quantified with fluorescence microscopy. The patterns of molecular uptake for the three representative stand-off distances $\gamma = 0.1$, 0.9 and 2 are depicted besides the corresponding bubble series in figure 3.2. The green fluorescence originates from the interior (cytoskeleton) of the adherent HeLa cells. Thus, the laser-induced cavitation bubble is able to porate the cell membrane very similar to shockwave- induced cavitation.

From the pictures as shown on the right of figure 3.2 we quantify the

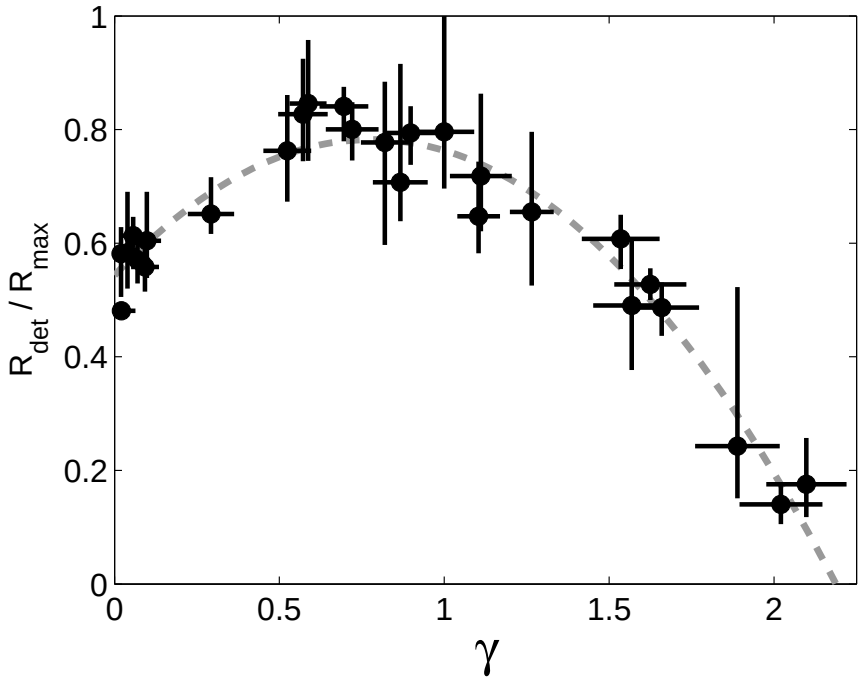

Figure 3.3: Plot of the averaged non-dimensionalized radius R_{det}/R_{max} of the cell detachment area (πR_{det}^2) as a function of the stand-off distance γ. The filled circles are individual experiments and the dashed line is a fitted parabola with a correlation coefficient of 0.95. The error in the detachment radius is obtained from the variations in the radius of the detached area along the circumference. The averaged maximum bubble radius is $1.0\text{mm} \pm 15\%$.

uptake with two methods. For both of the methods the geometrical center of the uptake area is determined first and then the fluorescent intensity distribution is measured as a function of the radial distance while averaging over the angle. The radial distribution of the calcein uptake is shown in figure 3.4 for various stand-off distances. Please note that the height of each curve is rescaled e.g., their amplitude does not reveal the integrated intensity. Calcein positive cells are found on a ring surrounding the detachment area, i.e. uptake is found for cells being exposed presumably to the highest levels of wall shear stress while remaining attached. The width

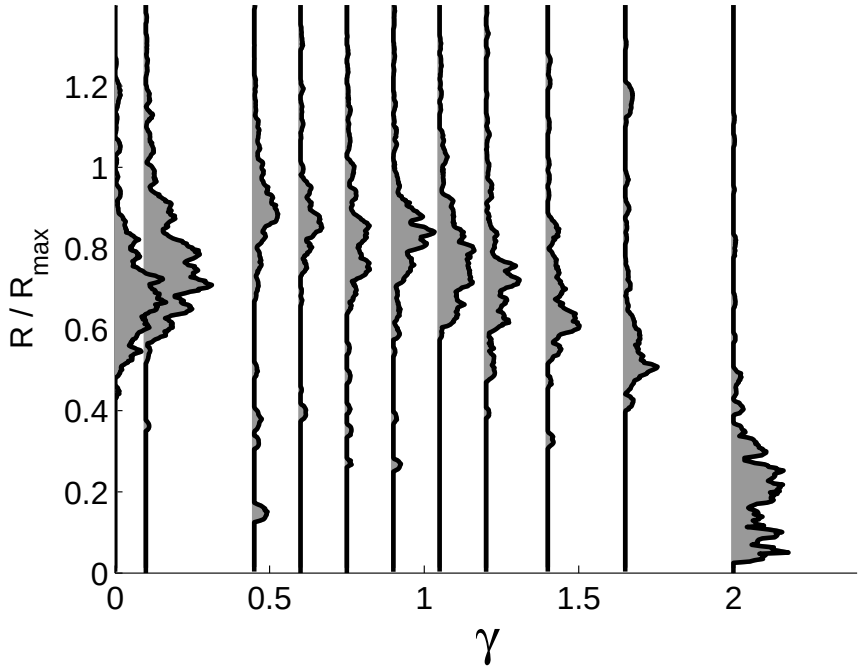

Figure 3.4: Fluorescence intensity pattern as a function of the distance from the projected center of the bubble (normalized by the maximum radius of the bubble R_{max}) for various stand-off distance values γ. For each stand-off distance the zero fluorescence baselines are vertical and the signal represents the integrated fluorescence signal averaged over the angle. In average the maximum bubble radius is $1.0\mathrm{mm} \pm 15\%$.

of the ring of calcein uptake varies with the stand-off distance: the closer the bubble is generated to the boundary the wider the ring of uptake.

What is the optimum stand-off distance for molecular uptake? An answer to this question is given in figure 3.5 by plotting the total area of calcein fluorescence for various γ-values; this area is normalized by the cross-section of the bubble. Although the scatter of the data is large, a clear trend is visible: with decreasing stand-off distance more cells show uptake. This negative trend is supported by a Spearman rank correlation coefficient of -0.77. Maximum uptake is found for bubbles closest to the cells, i.e. for $\gamma = 0$ and the uptake decreases with increasing distance. In

contrast to the finding of a maximum of the detachment at $\gamma \sim 0.65$, we find monotonically increasing uptake when the bubble is created closer to the cells. The absolute value in figure 3.5 however should be read with care for a few reasons: firstly, not the whole cell is fluorescent but only some fraction of it. Secondly, though confluence is constant it is not taken into account in this measurement and last, low levels of fluorescence may be lost by applying a threshold in the image analysis. Thus, the number of cells affected cannot be directly read from the area of uptake.

3.3.3 Cavitation-induced cell death

It is reported in Ohl et al [2] that cell death (ethidium bromide positive cells) occurs at the edge of the detached region. The question remains whether cell death is necrosis- or apoptosistype and whether deep into the non-detached cell layer late apoptosis is induced. Effects on cell viability and especially the induction of apoptosis have been reported for cancerous human lymphocytes exposed to cavitation bubbles driven with a continuous ultrasound wave [12].

Here, for the study of apoptosis fluorescent compounds are used and for quantitative analysis of cell metabolism an MTS assay is employed. For this study and the below reported MTS assay, we fixed the stand-off distance of the bubble to $\gamma \sim 1$.

The fluorescent staining agents for the apoptosis studies consist of a set of three apoptotic and viability markers which allow for detecting cell death and for distinguishing between apoptosis and necrosis. The first marker is a mitochondrial staining, TetraMethylRhodamine Ethyl ester (or TMRE, perchlorate) which is dependent on the inner mitochondrial membrane potential. Healthy cells are positive to TMRE, whereas they become TMRE-negative when entering apoptosis as a result of the depolarization of the inner membrane of the mitochondria. Later in the process of apoptosis, the phospholipid composition of the cell membrane changes, notably with the externalization of phosphatidylserine (PS) which is targeted by the second marker, Annexin V-Alexa Fluor 647 [13, 14]. The third dye is a nuclear probe, YOPRO-1 that enters cells only after disruption of their membrane (in late stages of apoptosis). By using these three dyes, we can distinguish between viable cells (TMRE-positive), cells entering apoptosis (TMRE-negative), early apoptotic cells (Annexin V-positive) and late apoptotic cells (Annexin V and YOPRO-1 positive).

In a first step, we wash cells after the cavitation experiment, place them in a calcium enriched medium supplemented with the three dyes

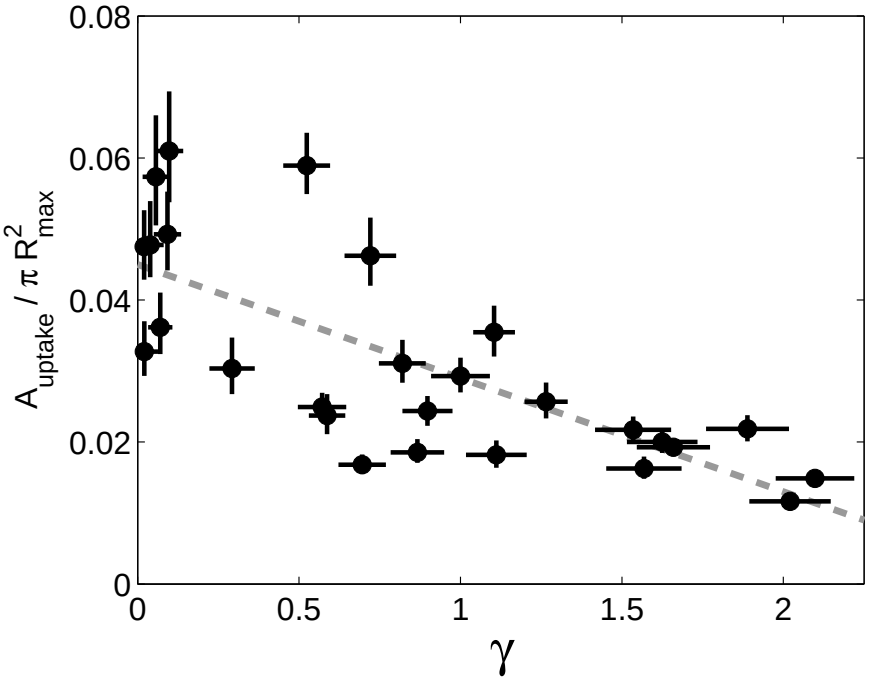

Figure 3.5: Plot of the measured area (normalized by the cross-section of the bubble at maximum radius, πR_{max}^2) with calcein uptake as a function of the stand-off distance γ. The error in the measured area of uptake is obtained by varying the threshold value during image analysis by $\pm 10\%$. Additionally, we performed a rank correlation test (Spearman) which gives a correlation coefficient of -0.77, supporting the large negative correlation between the stand-off distance and the uptake area. The dashed line is linear least square fit to the data. The averaged maximum bubble radius is $1.0 mm \pm 15\%$.

and image them using CLSM. Cells are found TMRE-positive both in the control samples and in the treated wells except close to the detachment area. In the zone surrounding the detachment area, cells are round-shaped and some of them start to detach. Moreover, cells in this area become positive to both Annexin V and YOPRO-1, indicating apoptosis. It is important to mention that dead cells that have detached from the surface and float in the medium are removed upon washing and replacing the

medium.

Not to loose the free-floating cells dying directly upon exposure to the bubble, we decided to carry out a second series of experiments without washing the cells at the end of the cavitation experiment but by directly using calcium-enriched culture medium and to only add the three dyes after the cavitation experiment. As depicted in figure 3.6, the amount of cells positive to both Annexin V and YOPRO-1 increases and are randomly dispersed in the well, both on the detached area as well as above the viable cells, as these dead cells are free to move in the solution. Apoptosis is mainly detected at the border of the detachment area and not in cells further away. This is visible in figure 3.6 by the two-colored ring located around the detachment area detected by confocal microscopy.

Using the same procedure (without washing) we image cells over time at one particular location at the border of the detachment area for $3\mathrm{h}$ (starting circa 30 min after the cavitation experiment) with a $10\mathrm{min}$ interval between pictures. Two confocal microscope images have been selected in figure 3.7 depicting the area $30\mathrm{min}$ and $3\mathrm{h}$ after the cavitation event. It shows the increasing number of apoptotic cells as time passes. At the beginning, figure 3.7 top, mainly Annexin V-positive cells are found, whereas the amount of YOPRO-1-positive cells increases in the first hours. The shape of the cells evolves as well, blebs become larger and hollow structures into which apoptotic cells leak appear, see figure 3.7 bottom.

Both themorphology of the cells (e.g. blebbing) and the consecutive staining with Annexin V and YOPRO-1 characterize these cells as apoptotic and not necrotic. In the case of necrosis, the cell membrane and nucleus are permanently porated and cells become simultaneously positive to Annexin V and YOPRO-1. Furthermore, necrosis is instantaneous and no cell blebbing, which is characteristic for apoptosis, takes place.

We perform timelapse imaging up to $24\mathrm{h}$ after the cavitation experiment. After $24\mathrm{h}$, not significantly more dead cells are found (data not shown). Also, cells located close to the detachment area grow again and adopt a flat and stretched shape, which is demonstrated in figure 3.8. This indicates that cell growth is not inhibited by the cavitation event. In this figure cells located close to the detachment area are compared 1 and $24\mathrm{h}$ after cavitation exposure; the two pictures reveal that cells adopt a round shape just after the cavitation event whereas they reshape back to a monolayer flat morphology one day after the experiment. Longer monitoring of cell viability is not feasible due to the limited size of the wells. In summary, we see that cell death occurs by apoptosis and mainly close to the spot where the bubble is created. Moreover, cell death is ob-

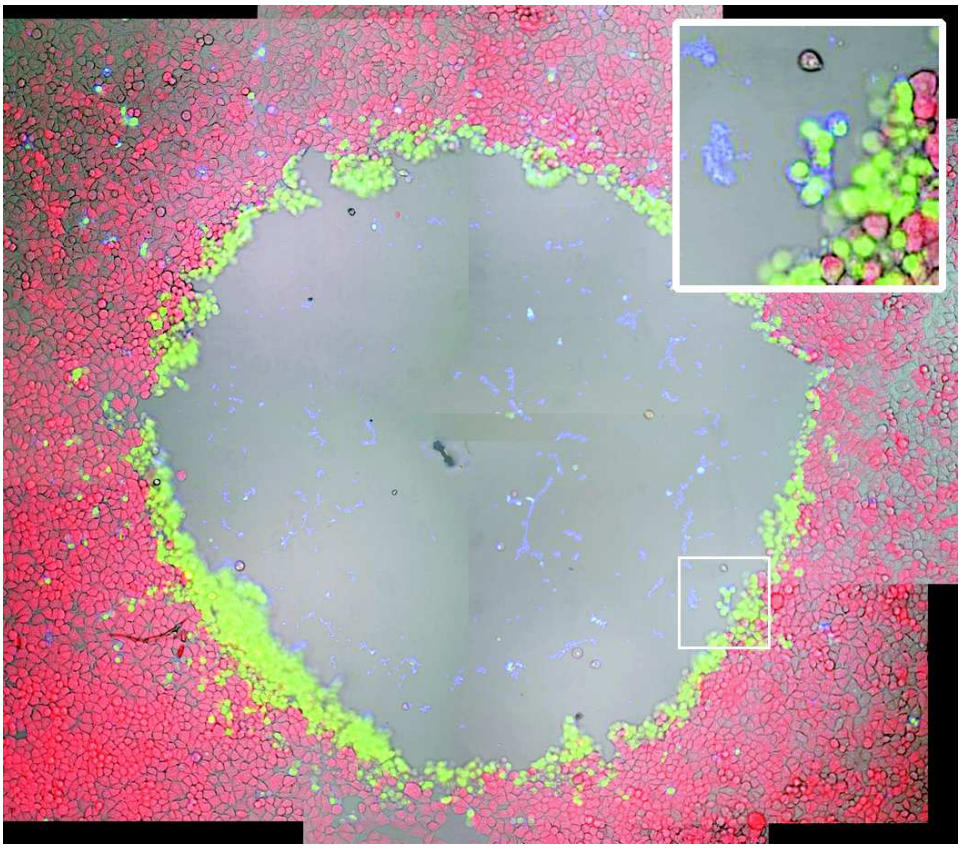

Figure 3.6: Reconstituted picture of the detachment area and its surrounding part, showing the four zones on the surface. Cells are stained with the set of three markers for detecting apoptosis after exposure to the cavitation bubble. TMRE (red in color online and gray outer cells in print) stains viable cells, while (Annexin V-Alexa Fluor 647) (blue in color online and dark gray inner cells in print) (YOPRO-1) (green in color online and bright cells at the border in print) stain dead cells. TMRE-positive cells are found everywhere in the monolayer but in the detached area (zone 1) and just around it (zone 2), where cells have been affected by the cavitation bubble. Annexin V- and YOPRO-1-positive cells are found floating in the medium above the monolayer and the detached area as well as the border of the detachment area (zone 2) where cells are dying at a slow time-scale.

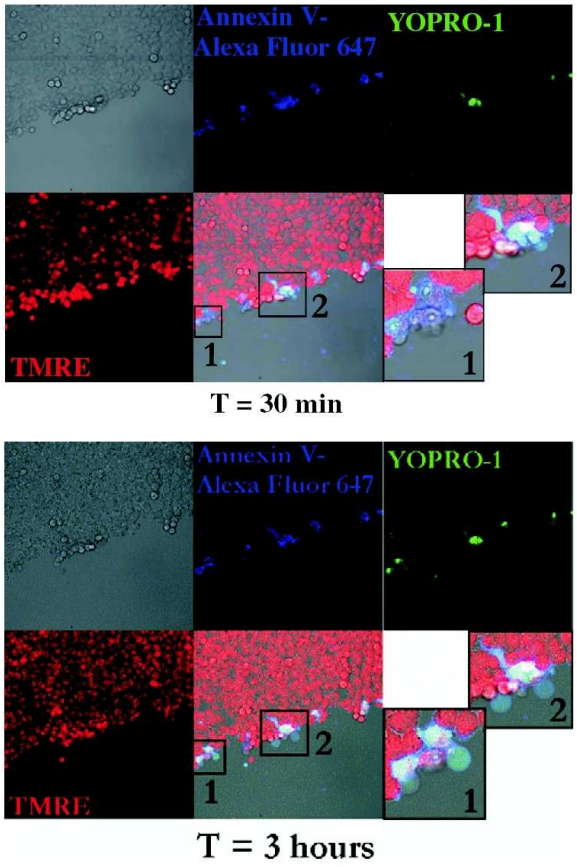

Figure 3.7: Two views from a time-lapse imaging sequence recorded at the border of the detachment area illustrating changes in cells and apparition of apoptosis as a result of the cavitation bubble induced flow. In both views the cells are stained with three dyes, TMRE, Alexa Fluor 647 (coupled to Annexin V) and YOPRO-1. The upper view was taken 30$\mathtt{min}$ after exposing the cells to the cavitation event. At $\mathtt{t} = 30\mathtt{min}$, there are a few dead cells at the center of the viewing area (enlarged in insert 2) and at the left (insert 1). After 2$\mathtt{h}$ (data not shown), a new group of dead cells appear right to the center. Also blebbing structures, characteristic for apoptosis, appear on the cytoplasmic membrane in these three groups of cells. 3$\mathtt{h}$ after the cavitation event the blebs become larger (inserts 1 and 2). Also DNA staining is shown by the bright spots illustrating the condensation of chromatin and fragmentation of the DNA inside the nucleus.

served within a few hours after the cavitation event but no further cellular changes are observed after $2-3$h.

3.3.4 Cell viability

Viability of HeLa cells after their exposure to a single bubble is concomitantly assessed using an MTS assay over a time window of 24h so as to determine whether cells are functioning properly or whether they have been impaired by the cavitation event. This is compared to control samples, plated in similar microchambers but not submitted to a cavitation event. Figure 3.9 presents the results as averaged values for formazan absorbance (for four independent samples) for both series of samples (treated and control) at 0, 2, 4 and 24h. These values are corrected for the amount of cells in each well and therefore take into account the 5% loss of cells observed directly after the cavitation event (detachment area). These detached cells are removed by washing the samples prior to addition of the MTS reagent. From the data presented in figure 3.9, we can conclude

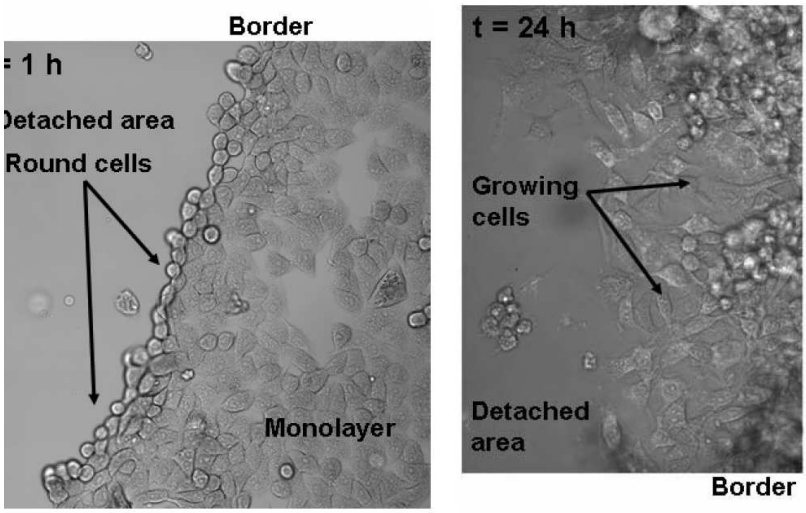

Figure 3.8: Enlarged views of the border of the detachment area. Left: 1h after exposure to the cavitation bubble the cells along the detachment area obtain presumably due to the loss of most of their focal adhesion points a rounded shape. Right: 24h later, the cells grow again into the former cell-denuded area and posses a flat shape.

that the overall viability of cells within two hours after exposure to a cavitation event is comparable to that observed in the control wells. A small decrease in cell viability ($1-5\%$) is subsequently observed for the treated samples (at 4 and 24h); this can be explained with the apoptosis of cells in the direct vicinity of the detachment area. The incidence that a single cavitation bubble has on a monolayer of HeLa cells with respect to the cell viability is in good agreement with the data collected using CLSM techniques that show a small increase in apoptosis within a few hours following the cavitation event close to the location of bubble oscillation whereas the overall amount of dead cells remains constant at longer time-scales (e.g., 24h). The initial lower abundance measured for formazan production, at $t = 0$, which shows a lower metabolic activity of cells just after the experiment for both the control and treated samples can be explained by the stress these cells have undergone: they have been taken out of the incubator and their medium has changed. After two hours, the cells have recovered as indicated by the higher metabolic activity.

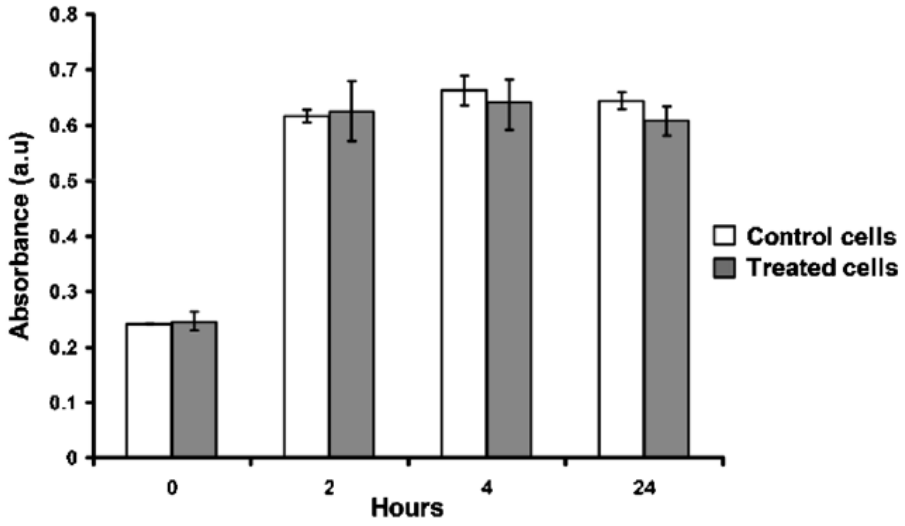

Figure 3.9: Cell viability and metabolic activity assessed through an MTS assay. Samples were taken at $t = 0$, 2, 4 and 24h for cells exposed to a cavitation bubble (gray) (at $t = 0$) and for control cells (white) that underwent the same treatment except from the exposure to a cavitation event. Data correspond to the absorbance intensity measured at 492nm for the production of formazan by cells; these values have been averaged over four samples and are corrected for the amount of cells remaining in the wells (i.e. they take into account cell detachment following the cavitation event).

3.4 Discussion

3.4.1 Regions in the monolayer of cell-bubble interaction

After exposure to a cavitation bubble the monolayer of cells can be divided in four distinct regions. The first region is located directly below the center of the bubble and corresponds to the spot of jet impact and radial spreading. In this region cells are suddenly detached. The second region is located around the detachment zone and consists of a 1-3 cell wide ring where cells die on a time-scale of $1-2$h. These cells have greatly experienced the jet-induced flow but they have not been detached, and as a result become porated in a permanent way, causing apoptosis. In an earlier study we found, when fixing the cells within a few minutes after the cavitation exposure, large pores in SEM pictures of those cells [2]. The third zone is composed of cells which are porated but to a lesser extent and in a transient way. This region is the area where viable drug delivery occurs. The fourth zone consists of the rest of the monolayer and is composed of cells which are unaffected by the cavitation event; they are located too far from the bubble-induced flow.

We assume that the pore size and/or the number of pores in the membrane decrease with increasing distance of the cells from the bubble center. Cells located very close to the bubble (region 1 and 2) are literally perforated; they are lysed or die by apoptosis. Cells located in region 3 are also porated but pores are smaller or less frequent, and they enable the entry of foreign substances (region 3) or are too small for that. It might be possible to decide if either the number of pores or the size of the pores decreases with distance by using particles of different sizes with different fluorescent markers and evaluate their uptake pattern as a function of the distance from the jet impact.

3.4.2 Cell death

As already mentioned, exposure to a cavitation event leads to cell death in given zones in the monolayer. Either immediate cell lysis or slow apoptotic death is observed $1-3$h after cavitation exposure in the first ring of cells around the detachment area. On a longer time-scale no further change is observed and remaining cells are observed to be viable and functioning properly according to an MTS assay. Moreover according to confocal studies cells in region 2 die by apoptosis and not by necrosis as indicated by the Annexin V-positive staining. This finding is similar with

the reported cell death following ultrasound exposure with microbubbles [15]. However, it is not clear in the ultrasound experiments if similar but smaller scale bubble dynamics is present, see also van Wamel et al [16].

Sonoporation leads to death of cells according to two mechanisms, either by lysis [17, 18] or apoptosis [19]. If in vivo cell killing is the goal, then apoptosis would be the preferred modality as fewer immune reactions are expected from the organism while cell lysis evokes an inflammatory response [20]. In our experiments, we observe apoptotic bodies floating in solution (data not shown); this demonstrates that cells are detached from the surface upon bubble expansion and collapse as suggested by Ohl and Wolfrum [21]. Yet, cell lysis can not be excluded especially for cells close to the stagnation point. Indeed, first attempts to carry out an MTS assay without washing have not been successful; our hypothesis is that the medium was full of chemicals released by cells and that these compounds hinder the redox reaction on which the MTS assay is based. Consequently, although cells die by apoptosis we cannot exclude lysis for cells from the detached area.

3.4.3 Correlation with wall shear stress exposure

Our main assumption is that the cavitation-induced flow strains the adherent cells which leads to pore creation in their membranes and consequently to the uptake of molecules from the surrounding fluid into the cells cytoplasm. Although this study does not reveal the dynamics of cell membrane straining, the obtained results are supported by this general picture of a fluid mechanical induced forcing of the cell membrane. The second observation, namely cell detachment, is found for bubbles collapsing close enough to the boundary, $\gamma \leqslant 2$. A maximum of the detached area is found for $\gamma = 0.65$. Interestingly, it has also been reported that the highest jet impact velocities are occurring between 1 and 0.5 [10]. This finding suggests that detachment of the cells might be correlated with the impulsive flow from the spreading of the wall jet. Unfortunately, the fluid dynamics driven by the cavitation bubble is considerably more complex e.g., the bubble collapses multiple times, a translation of the bubble center toward the wall occurs, a long lasting vortex ring is created. Still, considering that the detachment is caused by the first and most violent jet impact we can give an estimate of the wall shear stress occurring.

The fluid dynamics of the wall spreading jet has been studied using an analytical solution, the Glauert solution [22] for a steady and laminar wall jet. For the convenience of the reader we repeat here equation (1) of Ohl

et al [2]:

$$\tau = \rho\nu \left(\frac{\partial u}{\partial y}\right)_{y=0} = \rho \left(\frac{125F^3}{216\nu x^{11}}\right)^{1/4}, \tag{3.1}$$

where the constant $F = (1/128)u_{jet}^3 d_{jet}^4$ allows an estimate of the wall shear stress at the border of the detached region. The variables and parameters in equation (1) are: u is the bulk velocity tangential to the wall, ρ is the density of the liquid, ν is the kinematic viscosity, and u_{jet} and d_{jet} are the speed and diameter of the jet, respectively.

For $\gamma = 0.65$ with a jet velocity at impact of $v_{jet} = 70 ms^{-1}$ (see e.g., figure 3(d) Philipp and Lauterborn 1998) and a jet diameter of $1/10$ of the maximum bubble diameter $R_{max} = 1.0 mm$ the wall shear stress at the edge of the detached region (at $0.8 mm$ from the stagnation point) the Glauert solution predicts approximately $30 kPa$ for the wall shear stress. Although this value seems very large, it is of the same magnitude as reported by Rau et al [18]. There, the wall shear stress estimated during the bubble expansion which causes cell lysis ranged between $60 kPa$ and $220 kPa$. We want to mention that in both approaches [2, 18] a rigid wall with no slip is assumed and this overestimates the wall shear stress when the surface is covered with deformable cells.

The number of cells showing molecular uptake increases with decreasing the stand-off distance, which is in contrast to the area of detached cells. Again, we expect that the wall shear stress is the important contribution to the trans-membrane transport. Yet, only cells in a certain range of exposure conditions show uptake. For too high or too long lasting shear, the cell will become detached and too little shear does not affect the cell membrane. Here, the results indicate that not only the jet but other flow features contribute to the pore formation. High levels of wall shear stress can be generated not only by the spreading jet flow, but also by the expanding/collapsing bubble interfacewhen the bubble is close enough to the boundary [18].

If we come back to the experiments conducted by Venugopalans and Vogels group [23, 18, 24], they report on cell lysis already occurring during the rapid expansion of the bubble. In this case a hemispherical bubble is created on top of the wall supporting the cells e.g., the bubbles stand-off distance is about $\gamma = 0$. Yet, the mechanisms for bubble-cell interaction are similar: the bubble accelerates the fluid close to the boundary to a high velocity which leads to strong shear in the boundary layer where the cells reside. The timing when the shear is generated is different: in the

latter experiments by Venugopalans and Vogels group the explosive expansion and in our experiments and as reported by Ohl et al [2] during the spreading of the jet.

In summary the following scenario is suggested. When the bubble oscillates far from the boundary, $\gamma > 2$ approximately, the jet flow is too weak to create sufficient shear once it impacts on the boundary. In the intermediate regime, approximately $0.5 < \gamma < 2$, the jet impacts with sufficient strength such that the radial spreading leads to the most important contribution. In this regime the bubble is too far from the boundary to harm the cell membrane by its rapid expansion. However, when the bubble is generated closer to the boundary, approximately $0 < \gamma < 0.5$, the expansion (and presumably also the collapse) of the bubble dominates while the jet flow strength decreases and vanishes for $\gamma \sim 0$.

3.5 Conclusion and outlook

We have demonstrated drug delivery in a monolayer of HeLa cells by means of a single cavitation bubble created in close vicinity to the surface covered with cells. The findings are in agreement with our previous work [2], however now a more controlled and single bubble system is used. The advantage is that we have control over the position of the bubble with respect to the cells. The efficiency of the drug delivery process depends on the stand-off distance at which the bubble is created with respect to the wall: the closer the bubble to the wall the higher the yield, together with little cell loss by cell detachment. Moreover, the studies of cell fate and viability after exposure to a single cavitation event demonstrate that cells survive the cavitation event, although a small amount of cells located just at the border of the detachment area die by apoptosis within a few hours. This apoptotic ring is a few cells wide.

The four regions of bubble-cell interaction are the result of a particular (time averaged) strength and a certain exposure duration. Thus one might ask if an optimum exposure condition exists for which viable transmembrane transport can be achieved without inducing apoptosis. To answer this question, the measurements of the wall shear stress have to be conducted to obtain its magnitude and its function of time. With this knowledge possibly cells grown in microfluidic channels could be exposed to a mock flow field with similar wall shear stress features. Thereby, the flow-induced drug delivery is optimized and made available for a larger number of cells. Because it is expected that the wall shear stress for up-

take and apoptosis differs with cell type, it might be possible to differentiate between cells using different hydrodynamic exposure conditions.

References

[1] Y. J. Li, J. H. Haga, and S. Chien, "Molecular basis of the effects of shear stress on vascular endothelial cells," *J. Biomech.* **38**, pp. 1949 (2005).

[2] C. D. Ohl, M. Arora, R. Ikink, N. de Jong, M. Versluis, M. Delius, and D. Lohse, "Sonoporation from jetting cavitation bubbles," *Biophys. J.* **91**, pp. 4285 (2006a).

[3] J. R. Blake, G. S. Keen, R. P. Tong, and M. Wilson, "Acoustic cavitation: the fluid dynamics of non-spherical bubbles," *Philos. Trans. R. Soc. Lond. A* **357**, pp. 251 (1999).

[4] O. Lindau and W. Lauterborn, "Cinematographic observation of the collapse and rebound of a laser-produced cavitation bubble near a wall," *J. Fluid Mech.* **479**, pp. 327 (2003).

[5] B. W. Zeff, B. Kleber, J. Fineberg, and D. P. Lathrop, "Singularity dynamics in curvature collapse and jet eruption on a fluid surface," *Nature* **403**, pp. 401 (2000).

[6] E. A. Brujan, G. S. Keen, A. Vogel, and J. R. Blake, "The final stage of the collapse of a cavitation bubble close to a rigid boundary," *Phys. Fluids* **14**, pp. 85 (2002).

[7] L. Junge, C. D. Ohl, B. Wolfrum, M. Arora, and R. Ikink, "Cell detachment method using shock-wave-induced cavitation," *Ultrasound Med. Biol.* **29**, pp. 1769 (2003).

[8] M. Arora, C. D. Ohl, and D. Lohse, "Effect of nuclei concentration on cavitation cluster dynamics," *J. Acoust. Soc. Am.* **121**, pp. 3432 (2007).

[9] A. Vogel, W. Lauterborn, and R. Timm, "Optical and acoustic investigations of the dynamics of laser-produced cavitation bubbles near a solid boundary," *J. Fluid Mech.* **206**, pp. 299 (1989).

[10] A. Philipp and W. Lauterborn, "Cavitation erosion by single laser-produced bubbles," *J. Fluid Mech.* **361**, pp. 75 (1998).

[11] C. D. Ohl, M. Arora, R. Dijkink, V. Janve, and D. Lohse, "Surface cleaning from laser-induced cavitation bubbles," *Appl. Phys. Lett.* **89**, pp. 74102 (2006b).

[12] L. B. Feril, T. Kondo, Z. Cui, Y. Tabuchi, Q. Zhao, H. Ando, T. Misaki, H. Yoshikawa, and S. Umemura, "Apoptosis induced by the sonomechanical effects of low intensity pulsed ultrasound in a human leukemia cell line," *Cancer Lett.* **221**, pp. 145 (2005).

[13] S. L. Gac, I. Vermes, and A. van den Berg, "Quantum dots based probes conjugated to annexin V for photostable apoptosis detection and imaging," *Nano Lett.* **6**, pp. 1863 (2006).

[14] I. Vermes, C. Haanen, H. Steffens-Nakken, and C. Reutelingsperger, "A novel assay for apoptosis. Flow cytometric detection of phosphatidylserine expression on early apoptotic cells using fluorescein labelled Annexin V," *J. Immunol. Methods* **184**, pp. 39 (1995).

[15] L. B. Feril, T. Kondo, Q. Zhao, R. Ogawa, K. Tachibana, N. Kudo, S. Fujimoto, and S. Nakamura, "Enhancement of ultrasound-induced apoptosis and cell lysis by echo-contrast agents," *Ultrasound Med. Biol.* **29**, pp. 331 (2003).

[16] A. van Wamel, K. Kooiman, M. Harteveld, M. Emmer, F. J. ten Cate, M. Versluis, and N. de Jong, "Vibrating microbubbles poking individual cells: drug transfer into cells via sonoporation," *J. Control. Release* **112**, pp. 149 (2006).

[17] T. Kondo, Y. Fukushima, H. Kon, and P. Riesz, "Effect of shear stress and free radicals induced by ultrasound on erythrocytes," *Arch. Biochem. Biophys.* **269**, pp. 381 (1989).

[18] K. R. Rau, P. A. Quinto-Su, A. N. Hellman, and V. Venugopalan, "Pulsed laser microbeam-induced cell lysis: time-resolved imaging and analysis of hydrodynamic effects," *Biophys. J.* **91**, pp. 317 (2006).

[19] H. Ashush, L. A. Rozenszajn, M. Blass, M. Barda-Saad, D. Azimov, J. Radnay, D. Zipori, and U. Rosenschein, "Apoptosis induction of human myeloid leukemic cells by ultrasound exposure," *Cancer Res.* **60**, pp. 1014 (2000).

[20] C. Munoz-Pinedo, D. R. Green, and A. van der Berg, "Confocal restricted height imaging of suspension cells (CRISC) in a PDMS microdevice during apoptosis," *Lab Chip* **5**, pp. 628 (2005).

[21] C. D. Ohl and B. Wolfrum, "Detachment and sonoporation of adherent HeLa-cells by shock wave-induced cavitation," *Biochim. Biophys. Acta.* **1624**, pp. 131 (2003).

[22] M. B. Glauert, "The wall jet," *J. Fluid Mech.* **1**, pp. 625 (1956).

[23] K. R. Rau, A. G. III, A. Vogel, and V. Venugopalan, "Investigation of laser-induced cell lysis using time-resolved imaging," *Appl. Phys. Lett.* **84**, pp. 2940 (2004).

[24] A. Vogel, P. Schweiger, A. Frieser, M. N. Asiyo, and R. Birngruber, "Intraocular Nd:YAG laser surgery: laser-tissue interaction, damage range, and reduction of collateral effects," *IEEE J. Quantum Electron.* **26**, pp. 2240 (1990).

4

Interaction of living cells with laser-induced cavitation bubbles in microfluidics [‡]

In this chapter the interaction of a adherent and suspension cells with spatially controlled cavitation bubbles is demonstrated. Adherent cells which remain adherent show leakage of their cytosol's content through the cell membrane. In contrast, suspension cells are strongly deformed into cushion and tear drop shapes. The suspension cells are more demanding because they are mobile and easily flush away in the course of the experiment. Therefore, these mechanical deformation experiments are conducted in confided geometries and with multiple cavitation bubbles. These experiments can be considered as a first step to micro-rheology using laser-induced cavitation.

[‡]Partially published as: Pedro A. Quinto-Su, Rory Dijkink, Firdaus Prabowo, Karthigayan Gunalan, Peter Rainer Preiser and Claus-Dieter Ohl, *Interaction of red blood cells with arrays of laser-induced cavitation bubbles*, Proceedings of the 7th International Symposium on Cavitation CAV2009, August 17-22, Ann Arbor, Michigan, USA, (2009).

4.1 Introduction

Microfluidics holds promises for biological research. Small lab-on-a-chip devices can be used to investigate and manipulate live cells [1]. For example the opening of the cell membrane which is a key step in introducing foreign materials substances like DNA fragments or biological markers. One technique which has already been implemented in a lab on a chip device is electroporation, the increase of a cell membranes permeability by applying low voltages [2, 3]. Because of this electroporation requires the addition of electrodes into the chip design and some way of trapping a cell in the electric field they produce [4]. This makes the production of the chips more complex and more expensive.

An alternative would be the use of sonoporation or membrane poration through strong shear flows created by cavitation bubbles [5, 6]. Some microfluidic work has been done using a single bubble and HL60 suspension cells [7]. Here a similar setup is extended with a spatial light modulator (SLM) giving the ability to simultaneously create multiple bubbles (see fig. 4.1 for an example) at any location in the area that is optically accessible with the microscope [8].

This chapter reports on two distinct experiments: one with adherent cells and one with suspension cells. The SLM was only available for the suspension cell experiments where a set of two or more bubbles surrounding a cell in suspension can subject it to a mechanical force through an accelerated flow without flushing it away. And though the experiments with adherent cells lacked are done with a single laser focus resulting into a single bubble.

4.2 Materials and methods

4.2.1 Adherent cell setup

A Nd:YAG laser (Solo-PIV, New Wave Research, Fremont, CA) generates a single 532nm pulse with a duration of 6ns (Figure 4.2). The objective in an inverted microscope (Axiovert CF 40, Zeiss, Goettingen, Germany) is used to focus the pulse into a microchannel containing the cells. The cavitation event is recorded using a sensitive double-frame camera (Sensicam QE, PCO, Weilheim, Germany) and a strobed high intensity LED. The camera uses the same objective as the laser with a dichroic mirror separating the their optical paths.

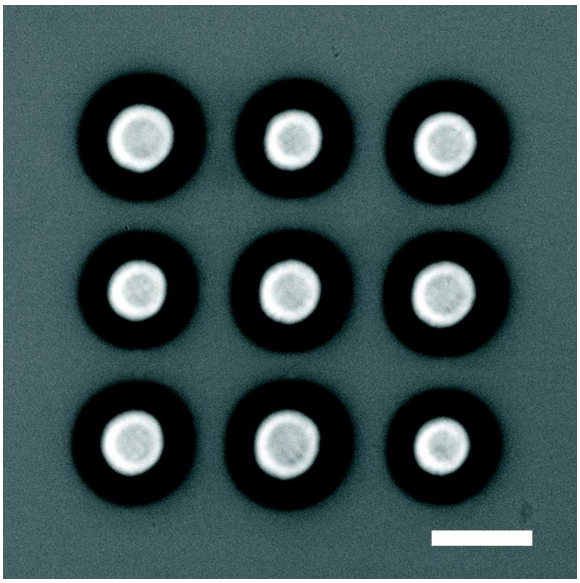

Figure 4.1: Example of an array of 9 expanding bubbles imaged at 1.2μs after generation. The length of the scale bar is 100μm.

To check the effect of the cavitation bubble on the cells both bright-field and fluorescent images are taken of the cells before and after the experiment. The built in microscope light source is used for the bright-field picture. For the fluorescent image a UV-light source (HBO 50, Zeiss, Goettingen, Germany) is coupled into the microscope instead of the laser using a switching mirror. The dichroic mirror is also swapped for fluorescent imaging to pass the UV-light.

4.2.2 Cell culture and preparation of the adherent cells

Epidermal HeLa cells (derived from human cervix carcinoma) are grown in Iscoves modified Dulbeccos medium supplemented with 10% of fetal calf serum (FCS) and 1% antibiotic antimycotic (all supplements are obtained from Invitrogen, Breda, The Netherlands). Cultures are performed in a humidified incubator with a temperature of 37°C and a CO_2 level of 5%. Tissue culture equipment is purchased from Nalge Nunc (Fisher Scientific B.V, Landsmeer, The Netherlands). Prior to the experiments, cells are seeded into commercially available microchannels (μ-slide VI, ibidi, Martinsried, Germany). The walls of the channels are treated to allow

the cells to adhere and grow on the lower channel wall. The cells are incubated overnight to allow the cells to attach to the surface and subsequently multiply once. $30-60 minutes$ before the experiment the growth medium is replaced with a phosphate buffered saline solution (PBS) containing Calcein-AM (Obtained from VWR, Amsterdam, the Netherlands) and Trypan blue (Acros Organics, Geel, Belgium). Trypan blue facilitates the uptake of laser energy during the experiment.

The cells are placed back in the incubator for another hour until the actual experiment. In this time the calcein-AM is absorbed into the cells where it is hydrolyzed into the fluorescent marker calcein. Calcein is unable to exit the cell by natural means and can thus function as a marker for membrane permeabilization.

4.2.3 Suspension cell setup

A Nd:YAG laser (Orion, New Wave Research, Fremont, CA) generates a single pulse at 532 nm with a duration of 6ns (Figure 4.3). It propagates

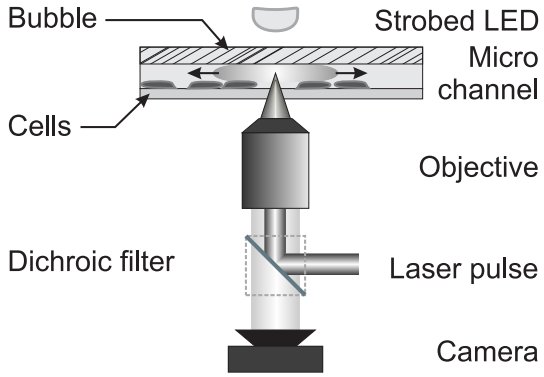

Figure 4.2: Shown here is a schematic representation of the setup used to expose adherent cells to a cavitation bubble. The cells grow on the lower wall of the microfluidics channel. A microscope objective is used to focus a single laser pulse into the channel causing a cavitation bubble to form. A high intensity LED above the channel is used to illuminate the bubble for a digital camera. The camera uses the same objective as the laser pulse, thus a filter set is needed to split the two beam paths and protect the CCD from the laser.

through a half wave plate to rotate the polarization and passes through a beam expander formed by lenses L1 and L2 to fill the display of the SLM. A digital hologram is projected on the SLM to create multiple foci. The pattern on the SLM imparts the phases needed to recreate the desired pattern at the focal plane of the microscope objective. The pattern is focused inside a thin microchamber filled with ink that maximizes the absorption of the laser light, such that at each laser focus a cavitation bubble is generated. The upper-left inset in figure 4.3 (above the SLM) shows the hologram used to create the 'five on a dice' pattern shown on the second inset.

The events are illuminated using a two more Nd:YAG lasers which are coupled into a fiber via cuvet filled with a fluorescent dye (LDS 698, Exciton, Dayton, Ohio). The function of the dye is to change the wavelength of the pulse allowing the illumination to pass through the dichroic mirror and notch filter and reach the camera. The partly incoherent fluorescence light is particularly suited for the illumination. The PCO camera, which is the same model as in the other set of experiments, is run in double frame mode. Together with the two separate lasers two images can be taken with an interframe time as short as 500 ns and exposure times of approx. $8-9\mathrm{n}s$.

4.2.4 Preparation of suspension cells

Red blood cells from healthy donors are used for the suspension cell experiments. A dense suspension of red blood cells was stored in a fridge. For the experiments the cells were diluted into yellow printer ink which allows laser absorption. To make the ink osmotically compatible with the cells a 10-times saline PBS solution was mixed with the ink at a ratio of 1:9.

A drop of ink containing red blood cells was pipetted onto a coverslip and a second coverslip was placed on top. Thin strips of aluminum foil are used as spacers between the two coverslips creating a $15\mu\mathrm{m}$ liquid film in between. The slides are clamped together and placed on the microscope.

4.3 Results

4.3.1 Adherent Cells

Figure 4.4 shows an overview of a sonoporation experiment with HeLa cells in a microchannel setup. Each frame also depicts a zoomed inset

of an area of interest, i.e. close to the laser focus. The two top frames show the cells before and after exposure to the cavitation bubble (*a* and *b* respectively) and frame *c* shows the location and maximum size of the bubble. When comparing these three images it first appears that the bubble doesn't have much an effect on the cells. The enlarged insets of frames *a* and *b* show some small changes in the cell contours but we need to look at the last image to see the real effect of the bubble. Frame *d* is a *difference image* obtained by subtracting the *before fluorescence* from the *after fluorescence* image. Thus black denotes an decrease and white an increase in the fluorescent intensity due to the bubble activity. The three cells that fall within the maximum bubble radius all show up dark meaning their membranes are permeabilized and calcein has leaked out.

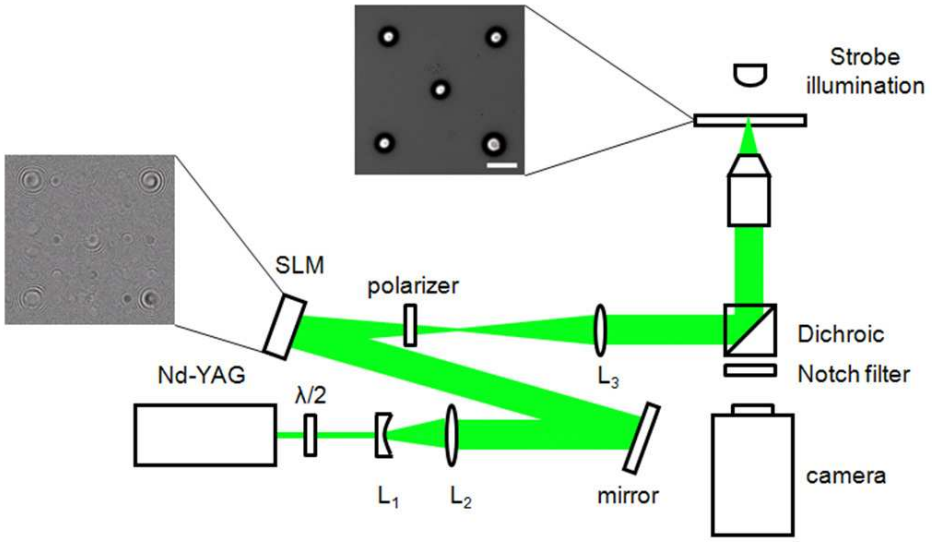

Figure 4.3: Schematic of the extended setup used to image the interaction of suspension cells and cavitation bubbles. The microfluidic chamber containing the cells resides above the microscope objective. The objective focusses a single laser pulse into the microchamber. The laser pulse first passes a spatial light modulator making multiple simultaneous bubbles possible. The inset at the SLM shows the phase image used to create the bubble array shown in the second inset. The bubbles are recorded on a double frame digital camera using strobed illumination.

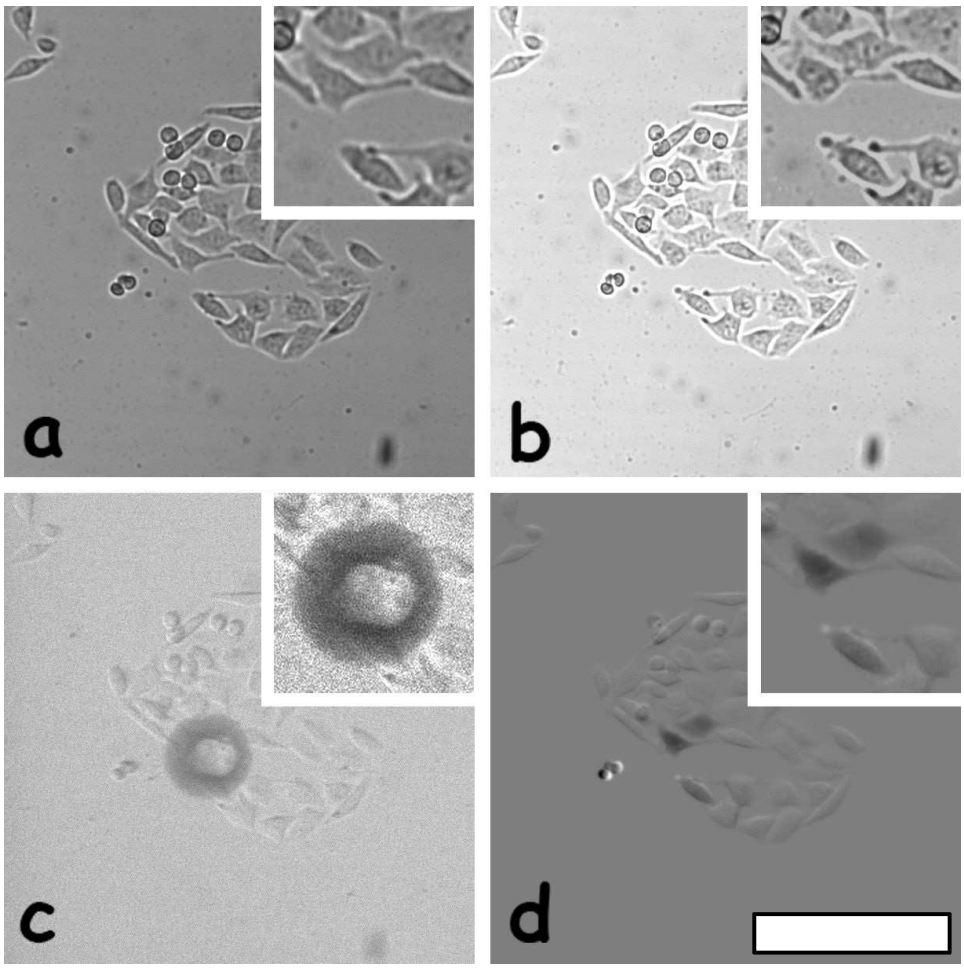

Figure 4.4: Overview of a cavitation exposure event with adherent cells. Frames *a* and *b* show the before and after images of the cells. The location and size of the cavitation bubble is shown in frame *c*. Membrane poration allows fluorescent dye to leak from the cell interior. The difference in fluorescent intensity before and after the cavitation event is shown in frame *d* where the dark grey shapes mark cells that have leaked dye. Each frame also has a zoom inset of the area surrounding the laser focus. The length of the scale bar is 100μm.

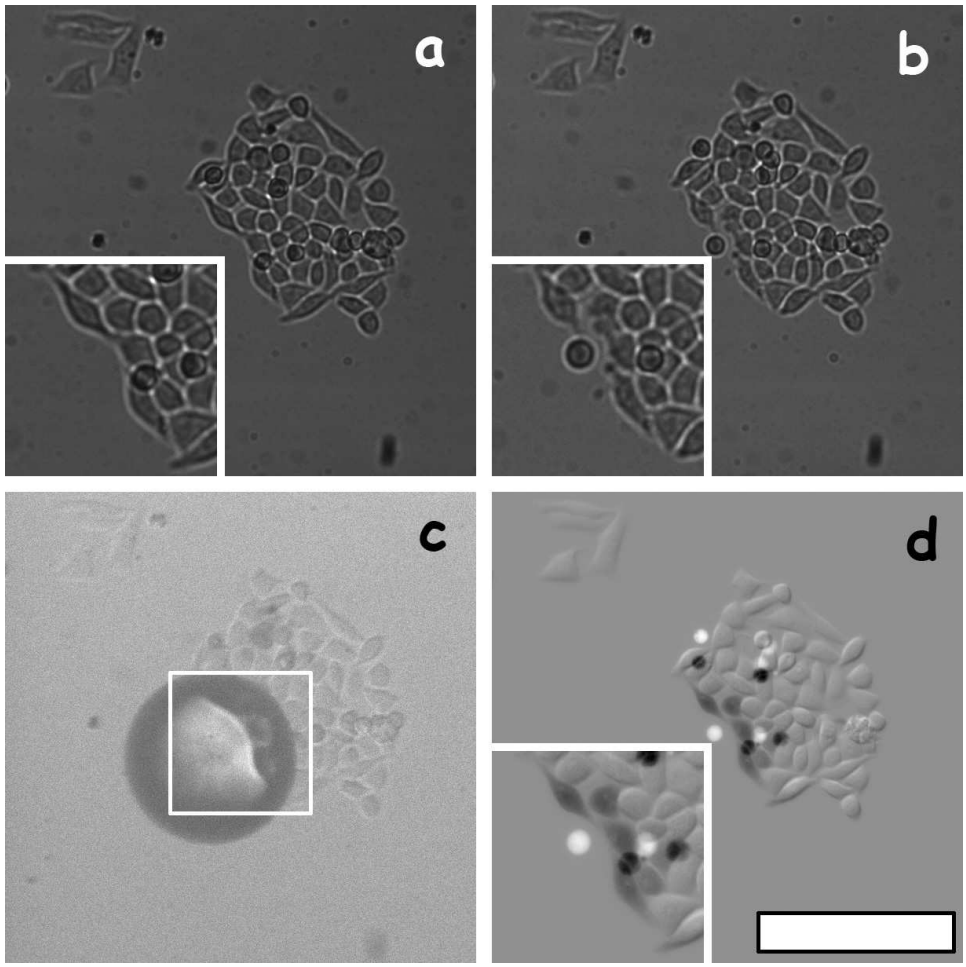

Figure 4.5: Overview of a cavitation exposure event with adherent cells. Frames *a* and *b* show the before and after images of the cells. The location and size of the cavitation bubble is shown in frame *c*. Membrane poration allows fluorescent dye to leak from the cell interior. The difference in fluorescent intensity before and after the cavitation event is shown in frame *d* where the dark grey shapes mark cells that have leaked dye. Three frames also has a zoom inset of the area surrounding the laser focus. Frame *c* only has the area marked out as a zoom would add no extra information. The length of the scale bar is 100μm.

The sharp black and white crescent shapes on the small round cells to the left of the bubble are not due to cell poration but a result of those cells being moved. Spherical HeLa cells are only weakly attached if at all and as a result are readily displaced by cavitation bubbles.

This is even more clear in figure 4.5 where the effect of a larger cavitation bubble is studied. The layout of the frames is the same as in the previous figure and frame *d* again shows the difference in fluorescent luminosity. The larger bubble has displaced the loose cells significantly resulting in pairs of black and white spots indicating the the original and final position of these cells. Comparison with the normal before and after images (frames *a* and *b*) confirm this conclusion.

Besides these black and white artifacts there are also adherent cells that show up dark grey because they have been porated and calcein has leaked out. As with the smaller bubble in fig. 4.4 all porated cells lie within the maximum radius of the cavitation bubble.

4.3.2 Suspension cells

The loose cells in the previous paragraph (see for instance fig. 4.5) showed that cells in suspension may displace due to the fluid motion induced by the cavitation bubble. We now present a configuration of two and more bubbles to target cells in suspensions. When two similar bubbles grow and collapse in phase there exists a stagnation point half way between the two bubble centers where the flow velocity is zero. Thus the cell remains localized by is exposed to normal and shear stresses. This is achived by arranging two laser foci on opposite sides of the target cell. Then the cells remains essentially stationary (see fig. 4.6 frames a to c).

The two expanding bubbles compress the cell in their center, see frame *b* of figure 4.6. As the cell is close to the stagnation point it is expected that the cells experience high pressures. Any liquid between the two bubbles flows out normal to the line connecting the bubble's centers. Together with the stagnation pressure the cells are exposed to shear stress.

The contour of the target cell (see the first of the three zooms beneath each frame for a high contrast close up) during bubble expansion has an eccentricity of $\varepsilon = 0.83$ at $t = 2\mu s$ even reaching $\varepsilon = 0.89$ at $t = 5\mu s$ where it was originally circular (i.e. $\varepsilon \approx 0$) in frame *a*. Afterwards the eccentricity of the cell, see frame *d*, is again zero though it is now lumpy and the diameter of an outer bounding circle has decreased by $\approx 10\% \pm 2\%$ with respect to the situation before the bubble oscillations. This sudden decrease in cell size suggests that the cell was has lost some of its content. It might

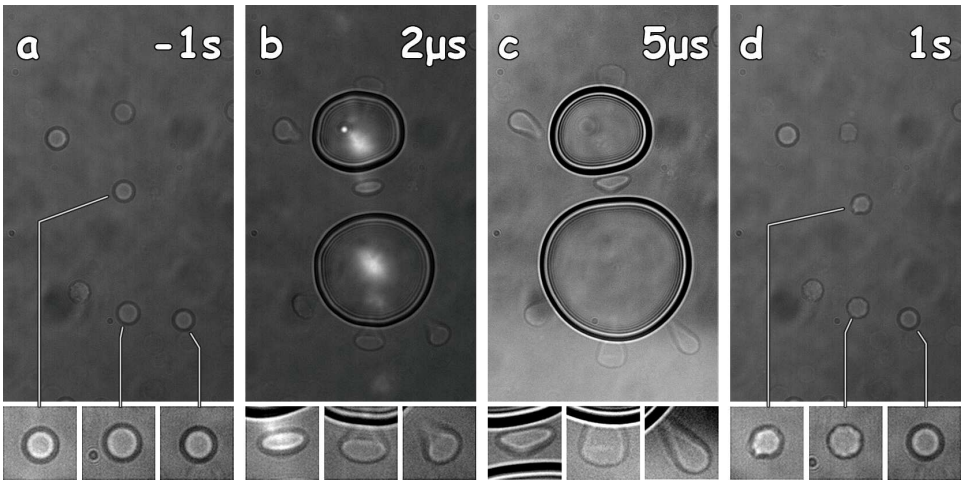

Figure 4.6: Set of 2 bubbles squeezing a red blood cell in their middle. *a* and *c* shows the red blood cells before and after and *b* is taken during the growth of the two cavitation bubbles.

be that the normal stress squeezing on the cell together with the shearing stress causing membrane rupture are leading to this rapid release of the cell's content.

The other cells surrounding the two bubbles take on a distinct "tear" shape (see the second and third zoom beneath each frame). Comparing frames *b* and *c* both motion blurring and the $1/r$ dependence of the flow field are ruled out. The images clearly show the bubble is still expanding, thus with a $1/r$ dependence of the flow field the side of the cell closest to the bubble should move out fastest flattening the cell instead of stretching it.

If the tail is motion blurring the cell has to move a distance equal to the length of the tail in the 10ns it takes to record the frame. This cannot be the case as $3\mu s$ later in frame *c* the cell has only moved a few micrometer.

An alternative explanation could be that the cell sits on the lower surface of the chamber and part of the cell is trapped in the boundary layer. Thus when the bubble expands creating a shear flow along the boundary the cell is partly caught in the velocity profile and stretched. The fact that the "tail" looks to be out of focus agrees with the our explantation that it is the lowest part of the cell.

Another interesting thing to note is that of the 5 cells surrounding the

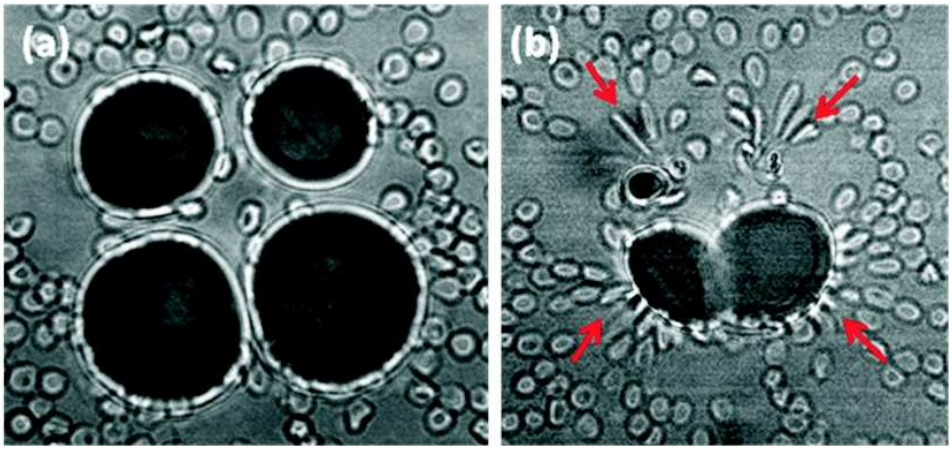

Figure 4.7: Array of 4 bubbles interacting with red blood cells. (a) Expansion of the bubbles. (b) Collapse of the array and deformation of the cells.

target cell only the cells with an initial location inside of the maximum bubble radius (R_{max}) look shrivelled in frame *d*. Look for example at the zooms beneath each frame, the middle cell starts of at $0.7 * R_{max}$ and the cell in the zoom on the right has an initial position of $1.1 * R_{max}$. Frame *d* shows the cell in the middle zoom to be shrivelled and shrunk but the cell in the rightmost zoom looks the same as before the bubble.

Figure 4.1 allready showed that the SLM is not limited to just two bubbles and figure 4.7 shows a set of four bubbles interacting with suspension cells. The concentration of cells is much higher this time and there are now multiple cells trapped between the four bubbles in the frame on the left. The four foci are not all of the same intensity causing the top two bubbles to collapse first as can be seen in the second frame of figure 4.7. As the bubbles collapse they each form a jet, denoted by the arrows in the second frame, aimed at the center of the bubble set. The cells that get caught in this jet flow are seen to be stretched even more that during the expansion and collapse of previous bubbles (see fig. 4.6)

4.4 Conclusion

Using a high speed camera and strobe photography with a temporal resolution of a few ns, we can observe the interaction between systems of

bubbles and cells, both adherent and in suspension. Poration of adherent cells was studied using a fluorescent dye that is otherwise trapped inside the cell. Decrease in fluorescence intensities has shown that only cells that are covered by the cavitation bubble during expansion are porated. Comparison of before and after images shows no structural damage to the porated and the cells further away. This observation is in agreement with studies of *Rau et.al.* that cells experience sufficiently strong shear during the bubble expansion from a hemispherical expanding bubble to rupture their membrane.

In the case of suspension cells we see noticeable deformation of red blood cells during the collapse of the bubbles. Though no fluorescent marker for membrane permeabilization was present the changes in the contour of the cell do suggest release of cytosol. Red blood cells, other than the targeted cell, that initially resided within the maximum bubble radius also show the wrinkled contour and decrease in size.

The cells just outside the bubbles maximum radius show no harm, at least for the duration of the experiment. However during bubble growth even these cells are deformed in large. Quantifying the deformation of these cells as they interact with bubble arrays could also prove useful, in particular for cell classification. It might be useful to distinguish anomalous cells from health ones which do have different mechanical properties such as for instance malaria infected red blood cells [9].

The SLM technique to create multiple bubbles has shown to be a very manageable tool. This technique may be applied to selected adherent cells from a larger population. Possibly, extracellular pathways between affected and unaffected cells can be studied.

References

[1] T. M. Squires and S. R. Quake, "Microfluidics: Fluid physics at the nanoliter scale," *Rev. Mod. Phys.* **77**, pp. 977 (2005).

[2] E. Neumann, M. Schaefer-Ridder, Y. Wang, and P. H. Hofschneider, "Gene transfer into mouse lyoma cells by electroporation in high electric fields," *EMBO J.* **1**, pp. 841 (1982).

[3] M. Khine, A. Lau, C. Ionescu-Zanetti, J. Seo, and L. P. Lee, "A single cell electroporation chip," *Lab Chip* **5**, pp. 38 (2005).

[4] M. B. Fox, D. C. Esveld, A. Valero, R. Luttge, H. C. Mastwijk, P. V. Bartels, A. van den Berg, and R. M. Boom, "Electroporation of cells in microfluidic devices: a review," *Anal. Bioanal. Chem.* **385**, pp. 474 (2006).

[5] C. D. Ohl, M. Arora, R. Ikink, N. de Jong, M. Versluis, M. Delius, and D. Lohse, "Sonoporation from jetting cavitation bubbles," *Biophys. J.* **91**, pp. 4285 (2006).

[6] K. R. Rau, P. A. Quinto-Su, A. N. Hellman, and V. Venugopalan, "Pulsed laser microbeam-induced cell lysis: time-resolved imaging and analysis of hydrodynamic effects," *Biophys. J.* **91**, pp. 317 (2006).

[7] S. L. Gac, E. Zwaan, A. van den Berg, and C. D. Ohl, "Sonoporation of suspension cells with a single cavitation bubble in a microfluidic confinement," *Lab Chip* **7**, pp. 1666 (2007).

[8] P. A. Quinto-Su, V. Venugopalan, and C. D. Ohl, "Generation of laser-induced cavitation bubbles with a digital hologram," *Opt. Express* **16**, pp. 18964 (2008).

[9] Y. Park, M. Diez-Silva, G. Popescu, G. Lykotrafitis, W. Choi, M. S. Feld, and S. Suresh, "Refractive index maps and membrane dynamics of human red blood cells parasitized by Plasmodium falciparum," *P. Natl. Acad. Sci. USA.* **105**, pp. 13730 (2008).

5

Laser-induced cavitation based micropump [‡]

Lab-on-a-chip devices are in strong demand as versatile and robust pumping techniques. Here, we present a cavitation based technique, which is able to pump a volume of $4000\mu m^3$ *within* $75\mu s$ *against an estimated pressure head of* $3bar$*. The single cavitation event is created by focusing a laser pulse in a conventional PDMS microfluidic chip close to the channel opening. High-speed photography at* $1 million frames/s$ *resolves the flow in the supply channel, pump channel, and close to the cavity. The elasticity of the material affects the overall fluid flow. Continuous pumping at repetition rates of up to* $5Hz$ *through* $6mm$ *long square channels of* $20\mu m$ *width is shown. A parameter study reveals the key-parameters for operation: the distance between the laser focus and the channel, the maximum bubble size, and the chamber geometry.*

5.1 Introduction

Bubbles are widely used as actuators in microfluidic devices. The most well known application is that in ink-jet printers [1]. There the explosive-

[‡]Published as: Rory Dijkink and Claus-Dieter Ohl, "Laser-induced cavitation based micropump",*Lab Chip* **8**, pp. 1676–1681 (2008).

like growth of vapor bubbles accelerates liquid though a nozzle and finally into a droplet for its deposition onto paper. These explosively expanding and shrinking bubbles which are commonly termed cavitation bubbles have recently received increasing attention for microfluidic applications. Cavitation enhances microfluidic mixing [2], allows for cell manipulation such as cell surgery [3] or cell lyses [4], and can be used for drug delivery within the micro-vascular system of a human body [5].

In contrast, cavitation occurs in some flow configurations where it is undesirable. Here, research focuses on the prevention of cavitation in microfluidics, for example in microfluidic phasechange heat-exchangers [6].

Yet, in the authors view, the advantages cavitation phenomena offer for microfluidic applications greatly surpass their disadvantages. Because of the rapid expansion and the flow focusing ability [7, 8] the liquid is accelerated to very high speeds. Thus, the prevalent low Reynolds number regime is overcome. This property was utilized in a recent study in Venugopalans group for the rapid mixing of chemicals in lab-on-a-chip devices [2], an application which is very difficult to achieve by other means [9]. A second application where cavitation is utilized is pumping. Here a high Reynolds number allows for flow asymmetry, such that the forward and back-stroke of the device posses different flow patterns. Tsai and Lin developed a bubble actuated micropump based on the difference in flow resistances of nozzles on the flow direction [10] where an oscillating bubble creates aperiodic flow which is given a preferred flow direction through the chip geometry. A very similar concept was utilized by Yin & Prosperetti where a vapor bubble is created at some distance from the center of a long channel, leading to a flow towards the longer half of the channel [11, 12]. Another concept of cavitation based pumps utilizes a special flow phenomenon when the bubble collapse progresses close to a rigid boundary. There, the bubble oscillation is strongly affected: during the shrinkage of the bubble the distant bubble interface bulges inwards and develops into a re-entrant jet directed towards the rigid boundary. Now, the trick in a pumping configuration is that the boundary has a small opening at the position where the jet would impact and it is small enough that the jetting phenomena is still occurring [13]. The hole permits the transport of liquid from above the boundary. Without this jetting phenomenon there would be flow through the boundary, however, the volume flux during bubble expansion and shrinkage would balance.

In this work we will scale the jetting flow concept down to lab-on-a-chip systems. In contrast to prior attempts of electrode or heater generated bubbles, we will make use of laser generated bubbles [8]. The advan-

tages of using an optical method is that a simple soft lithography technique can be used, no connections and wiring of the device is needed, and pumping can be achieved at many places on the chip. Additionally, the bubbles are transient vapor bubbles which quickly condense after actuation. Thus the pumping is not affected by any gas diffusion or creation of residual gas bubbles.

We will first explain the experimental setup to generate cavitation in lab-on-a-chip systems and how to study the pumping effect. Then the liquid motion during and after the pumping stroke is analyzed which reveals an important characteristic of elastic material based microfluidic devices. The experimental analysis is concluded with a parameter study of the bubble positioning/size and the chamber geometry.

5.2 Materials and methods

5.2.1 Microfluidic system and experimental setup

The microfluidic devices are made of PDMS (polydimethylsiloxane) with standard soft lithography techniques. The microfluidic device is bonded to a coverslip and viewed through an inverted microscope (CF 40, Carl Zeiss GmbH, Göttingen, Germany) with the coverslip facing down. The liquid is injected through tubing connected to the reservoirs, see Fig. 5.1. The long thin channels have a square cross section of $20 \times 20\mu\mathrm{m}^2$. The channel is passing through a chamber; the distance of the upper reservoir to the chamber inlet is $0.6\mathrm{mm}$ and $6\mathrm{mm}$ to the lower reservoir. Two different geometries are used, a square chamber with $200 \times 200\mu\mathrm{m}^2$, and a chamber with a flat boundary connected to the upper channel and a semicircular boundary connected to the lower one, see Fig. 5.1a. The slabs of PDMS are about $4\mathrm{mm}$ thick.

5.2.2 Cavitation generation

Single $6\mathrm{ns}$ long light pulses from a frequency doubled Q-switched Nd:YAG laser (NewWave, Solo PIV, wavelength $532\mathrm{nm}$) are focused in the microfluidic chamber with a $10\times$ microscope objective (NA0.25). The liquid is dyed with an aqueous solution of Direct Red 81 (DR81, Sigma-Aldrich Chemie, Zwijndrecht, Netherlands) resulting in a light absorption coefficient of $20.000\mathrm{m}^{-1}$ to $50.000\mathrm{m}^{-1}$ at the laser wavelength. The range of the laser energy is between $10\mu\mathrm{J}$ and $50\mu\mathrm{J}$.

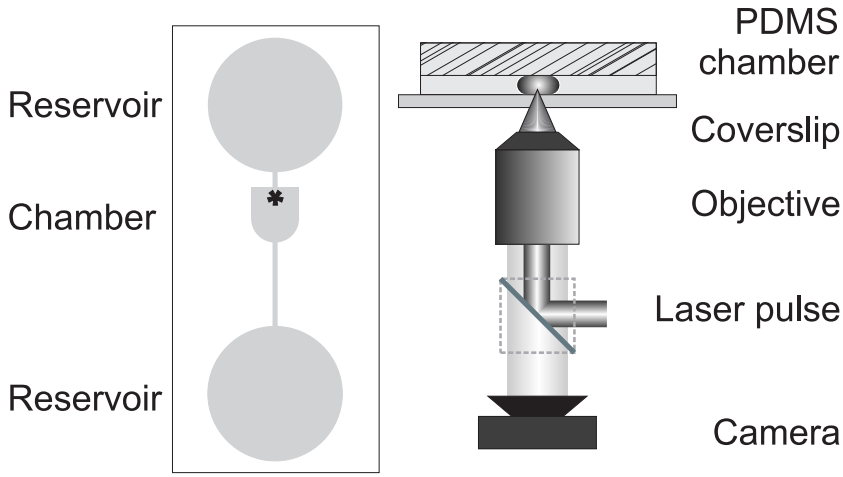

Figure 5.1: (a)Design of the microfuidic system to study the pumping effect: it consists of two circular fluid reservoirs connected via thin channels with the pumping chamber. The upper channel is $0.6\mathrm{mm}$ and the lower channel $6\mathrm{mm}$ long. The black asterisk denotes a typical location for the laser focus. (b) Sketch of the optical path for the generation of the cavitation bubble and the high-speed recording. The PDMS chip is bonded on top of a glass coverslip.

5.2.3 High-speed recording

The scene is recorded with a high-speed camera (HPV-1, Shimadzu, Duesseldorf, Germany).The laser and optical path of the camera are separated with suitable filters and a dichroic mirror. An intense fiber optic light (HL-1, Olympus, Zoeterwoude, The Netherlands) is necessary to obtain sufficient contrast to observe not only the bubble but also the tracer particles at the maximum frame rate of $1\mathrm{million frames/s}$ [8].

5.2.4 Flow-visualization with particle image velocimetry

Using a standard particle image velocimetry (PIV) algorithm (URAPIV, http://urapiv.wordpress.com) which correlates successive images from the high-speed recording, local flow velocities are obtained. For the algorithm an interrogation window of $8 \times 8\mathrm{pixels}$ is used at a spacing of

half the interrogation window size. The polystyrene tracer particles have a diameter of $2\mu m$ (Duke Scientific, Fremont, CA, USA). In contrast with conventional PIV experiments using a light sheet technique to constrain the image plane, here a relatively low NA objective records the particles within the chamber not only in a thin focal plane image plane but over the entire cross section. Therefore, the magnitude of the velocities is only a lower estimate of the chambers center velocity.

Additionally to the PIV algorithm applied inside the chamber, the particle displacement within the channels are measured manually.

We assume that the particles can follow the flow field with little slip. This is justified by the good agreement of the theoretical flow field with the measured one in previous work using the same type of particles [8].

5.2.5 Continuous pumping

For the continuous pumping experiments the microfluidic system was submerged in a water filled glass cuvet which was then placed on top of the microscope. For the recording of the fluid motion a sensitive double-frame camera (Sensicam- QE, PCO, Kehlheim, Germany) is used in combination with a strobed high intensity LED (V-Star, Lumiled, Philips). Image and motion analysis is done with Matlab and the image processing toolbox (Mathworks, Natick, MA, USA).

5.3 Results and discussion

5.3.1 Bubble dynamics and flow field inside the chamber

A single pump stroke consists of the rapid bubble expansion–collapse cycle followed by a slower residual flow. The bubble oscillations occur typically within $10\mu s$, the residual flow dies out only after about $80\mu s$. We discuss first the bubble expansion–collapse cycle together with the flow pattern.

The high speed recordings allow visualizing both the bubble shape and the flow pattern as shown in Fig. 5.2. Here, several frames from a $1 million frames/s$ recording depict the liquid slightly darker than the surrounding PDMS. The liquid is seeded with $2\mu m$ sized particles making the channel and pumping chamber easily distinguishable. The first image of Fig. 5.2 depicts the device just before the laser-induced cavitation bubble is generated. The second image displays the bubble initiation and shows

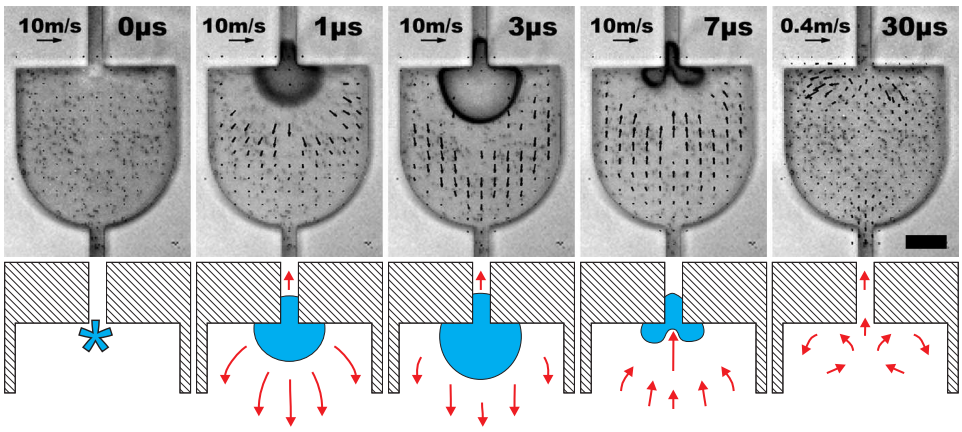

Figure 5.2: Selected high speed movie frames showing different stages of the bubble growth and collapse. The images include experimentally obtained velocity vector fields with a schematic representation of the flow field below each frame. The first image shows the chamber just before bubble initiation, then $1\mu s$ later the bubble is rapidly expanding, reaching its maximum size in the third image ($t = 3\mu s$). Afterwards the bubble starts to collapse creating a jet which is directed into the channel as can be seen in the fourth image. In the last image the bubble has completely disappeared leaving some circulating flow behind. Please note that the scale of the vectors, denoted by the reference arrow in the upper left corner of each frame, in the first 4 images is 25 times larger than the residual flow shown after the bubble has disappeared (5^{th} frame). The black bar in the lower right corner of the last frame denotes $50\mu m$.

the rapidly expanding bubble growing on the top wall of the chamber at the channel entrance with part of the bubble extending into the channel.

The rapid/explosive growth of the bubble and the limited exposure time of $500ns$ leads to a blurred bubble shape; yet we can estimate a lower radial velocity of the bubble during the first microsecond of at least $40ms^{-1}$! Due to the motion blurring the PIV algorithm isnt able to track the velocity close to the bubble interface, yet we see a nicely resolved outwards pointing flow pattern further away which drops almost to zero at the opposing channel entrance.

Because the lateral size of the bubble is much larger than the height of the chamber, the bubble obtains a pancake shape. In the third frame of Fig. 5.2, the bubble has gained its maximum expansion with some part of

the volume extending into the channel. Thereafter, the far field pressure drives the bubble to shrink. During the accelerated shrinkage/collapse of the bubble a jetting flow develops towards the upper channel resembling the collapse in semi-infinite liquid [14, 15], $t = 3\mu s$ in Fig. 5.2. The quasi two-dimensional nature of this experiment allows a detailed look on the jet shape. The jet accelerates through the bubble and is aimed towards the nearby boundary but because of the channel the jet doesnt impact on a PDMS chamber wall but flows into the channel. As we will show in the later discussions, it is this jetting which is important for the pumping effect.

In the later course of the bubble oscillation the bubble splits into two parts, $t = 7\mu s$ and it disappears. The flow pattern shown in frame $t = 30\mu s$ is a time average from $t = 10\mu s$ to $t = 30\mu s$. Upon careful inspection two counter rotating vortices remain, left and right of the upper channel entrance. The velocity after the bubble collapse is much lower; we find velocities of up to $0.4 m s^{-1}$ which quickly drop further from the upper channel inlet.

5.3.2 Flow inside the channel

Next we study the flow inside the channel and correlate it with the bubble dynamics. Here, we make use of individual tracked particles to quantify the fluid motion. Clearly, a boundary layer in the channel will lead to an uneven velocity distribution across the channel. Therefore, multiple particles are tracked; in general particles closer to the channel's center experience a larger displacement. Fig. 5.3 depicts the displacement of several particles in the upper (solid black lines) and lower channel (dashed grey) in combination with the bubble dynamics. For clarity, we have selected an experiment with a moderately large pumping effect. We will first concentrate on the particle motion in the upper channel.

The bubble dynamics lasts again for $10\mu s$ and selected frames are depicted on top of the graph in Fig. 5.3. The bubble expands further from the boundary as compared to Fig. 5.2, yet during jetting, the bubble moves close to the boundary ($t = 8\mu s$). This motion of the bubble centroid towards the boundary is well known in studies of cavitation bubbles close to semi-infinite boundaries [16, 17].

The tracer particle motion reveals the rapid motion during and following the bubble dynamics. When the bubble expands, $t < 4\mu s$ particles in the upper channel are accelerated upwards, whereas particles in the lower channel move downwards. This motion can be solely explained by

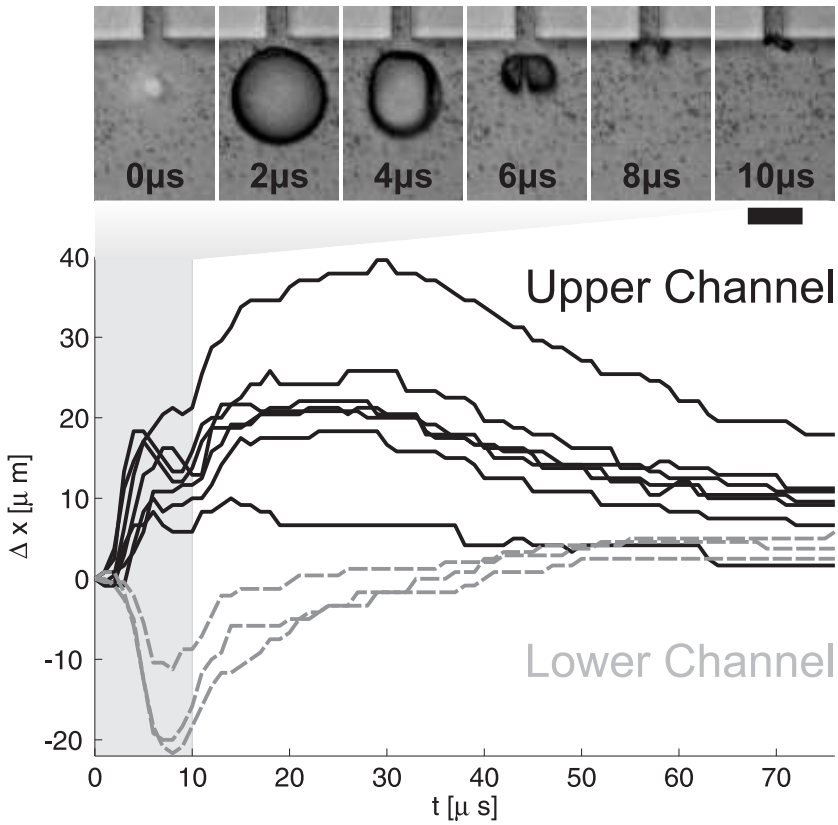

Figure 5.3: Another cavitating bubble is shown, this time located a little further from the channel opening. To estimate the induced flow speeds inside the channel, separate particles were tracked and plotted against time in the graph below the movie frames. The solid black lines are particles traveling in the pumping channel of which the opening can be seen in the images, for continuity some particles in the lower feed channel were also tracked and are displayed by the dashed grey lines. The light grey area between 010µs denotes where the movie frames are situated on the graphs timeline. The black bar below the last frame denotes 50µm.

the radial expansion of the bubble. In contrast, when the bubble starts to shrink, most of the upper particles are sucked towards the chamber, i.e. if both fluid motions would be symmetric no fluid displacement would remain. Yet, we find a lesser back flow, e.g. the second largest upward displacement graph moves approx. 18µm forward but only 5µm backward.

Most likely this is caused by the translational motion of the bubble centroid towards the upper channel: it is a superposition of the radial inflow and the translational, dipolar flow. During expansion however, the added mass [16] of the bubble prevents a large movement of the bubble centroid from the wall. Another observation is that the particle motion lags a few microseconds behind the bubble oscillations, e.g. maximum displacement during the expansion is observed between $t = 5\mu s$ to $t = 7\mu s$, whereas the bubble reaches maximum size at $t = 4\mu s$.

After the bubble expansion we find again a jet flow through the bubble which splits it into two parts at around $t = 9\mu s$ and reaches the upper channel inlet. Interestingly, it is at this time that all particles in the upper channel change direction. The particle motion prevails for $20\mu s$, long after the bubble has vanished. We explain this upward directed flow as a result of the continuing jet flow which lasts long after the bubble has disappeared. An equally valid description of the flow is that of two counter-rotating vortices left and right of the channel inlet accelerating liquid upwards at their contact line.

5.3.3 Effect of PDMS compliance

The solid lines in Fig. 5.3 exhibit a flow reversal in the upper channel at times $t > 30\mu s$ reducing the net displacement of the particles to about $40\% - 50\%$ of their maximum upwards travel. To investigate the cause of this flow reversal we studied the flow into the chamber by tracking particles in the lower feeding channel. Their trajectories are plotted in the same graph, Fig. 5.3 with dashed lines. During bubble expansion and early collapse, $t = 8\mu s$, the particles move away from the chamber. The maximum displacement is in the range from $10\mu m$ to $20\mu m$ and of the same magnitude as in the upper channel during bubble activity. Interestingly, no back flow occurs during the collapse of the bubble. Simple mass conservation in rigid structures would demand that the sum of the displaced volumes in the upper and lower channel is equal to the bubble volume and again zero after the bubble has disappeared. We now study the apparent missing volume by plotting the averaged volumes of the bubble, V_b, and the displaced upper and lower channel volume, $V_{uc} + V_{lc}$, in Fig. 5.4. The volumes V_{uc} and V_{lc} are calculated from the average of the displacement, Fig. 5.3, and the known channel cross section with volume leaving the chamber taken positive. The bubble volume is extracted by image processing assuming a generalized cylindrical bubble shape. The dashed-dotted line shows that the bubble obtains approximately a vol-

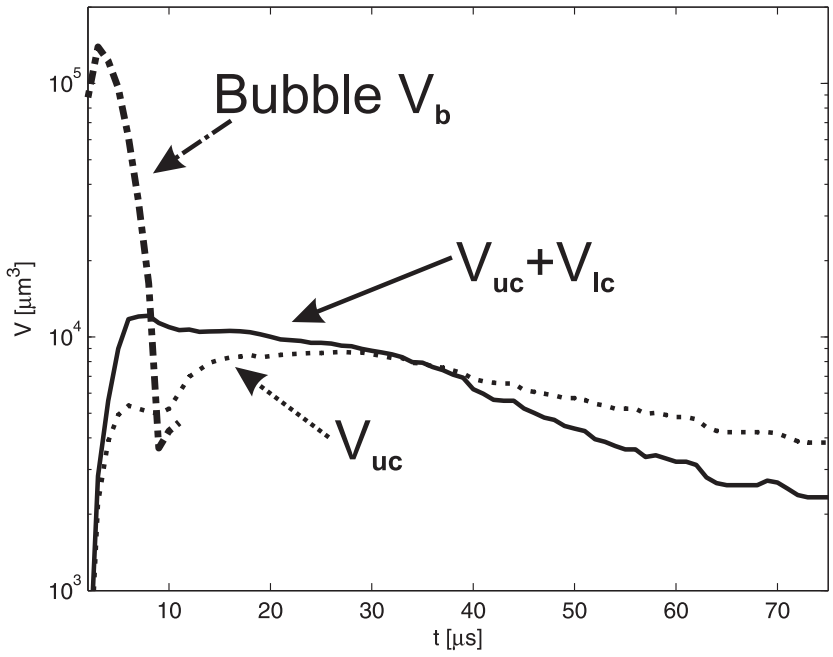

Figure 5.4: Volume balance during the pumping stroke: the void or bubble volume (dashed-dotted line), V_b, is compared with the total displaced liquid volume $V_{uc} + V_{lc}$ on a logarithmic scale. The difference between $V_{uc} + V_{lc}$ and V_b can be explained by a deformation of the pumping chamber. After the bubble has disappeared the total displaced volume is slowly relaxing to zero.

ume of $1.5 \times 10^5 \mu m^3$ which isnt balanced by the displaced channel volume of $1.3 \times 10^4 \mu m^3$. This discrepancy can be explained by a deformation of the fluid chamber. For the maximum bubble size we estimate that an expansion of the chamber of $1.7 \mu m$ towards the PDMS cover and the glass plate would already account for the missing volume. During the bubble shrinkage the situation reverses; the displaced volume, $V_{uc} + V_{lc}$, is larger than the bubble volume for $t > 7 \mu s$. This means that the chamber has shrunk.

After the bubble has disappeared, $t = 12 \mu s$, we observe a steady decline of $V_{uc} + V_{lc}$ with time. This is presumably caused by the expansion

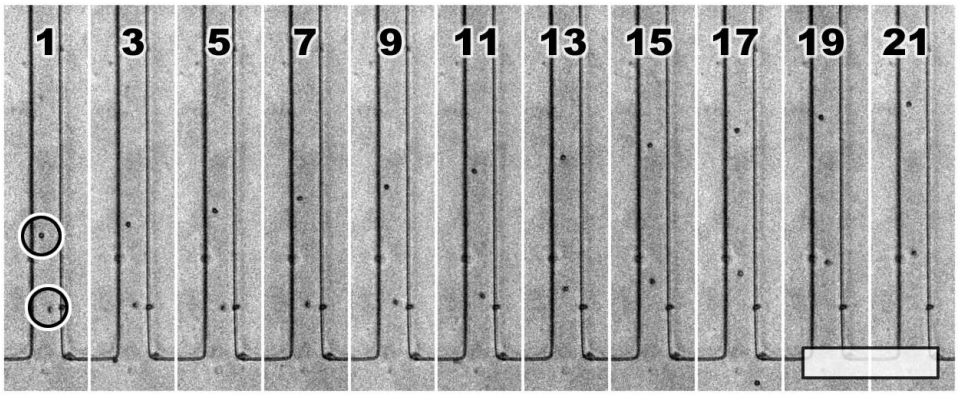

Figure 5.5: Pumping motion where the laser is run at 1Hz for multiple strokes: an image was taken 2ms after every pumping stroke, which is indicated at the top of each frame. Two tracer particles are encircled in the first frame with the top particle showing an average displacement of approximately 5μm per cycle or 10μm between frames. The white bar in the lower right corner denotes 100μm.

of the chamber back to its original size, sucking liquid back into the chamber. At time $t = 35\mu s$, V_{lc} becomes negative, thus both the upper and the lower channels now have a displaced volume in the same upwards direction. At the end of the pumping stroke, V_{uc} and V_{lc} become equal in magnitude but with opposing signs, i.e. the two volume displacements will be in the same direction and $V_{uc} + V_{lc}$ is zero. For a net volume displacement over a pumping stroke $|V_{uc}| > 0$ is required with the sign depending on the pumping direction.

5.3.4 Continuous pumping

Fig. 5.4 shows a steady decline of the displaced volume V_{uc} reaching $4 \times 10^3 \mu m^3$ after 75μs. This is equivalent with the averaged displacement of 10μm as shown in Fig. 5.3 (solid lines). One could argue that for longer times the net displacement and thus the pumping effect might be canceled.

To prove that this is not the case but a considerable net displacement remains the particles positions long after the bubble oscillation have been recorded. Additionally, the laser creating the bubble is operated in a continuous pulsing mode. Fig. 5.5 shows the particle displacement for 1Hz

laser frequency every second laser pulse and $2ms$ after the pumping stroke. Two particles are marked with a circle. The upper one moves approximately $10\mu m$ every two laser pulses. The lower particle which is imaged out of focus translates after some transition period ($1^{st}-9^{th}$ pump stroke) with the same displacement. This demonstrates that the remaining net displacement is indeed existent and $5\mu m$ per stroke, about half the displacement which we find after $75\mu s$, see Fig. 5.4.

Additionally, Fig. 5.5 shows that a continuous operation of the pump is possible. The maximum frequency of the laser used so far was $5Hz$ for 500 consecutive pulses. Under this operation condition, stable pumping was found without the formation of residual gas bubbles (see sets 5 and 6 in Table 5.1, discussion below). The repetition rate was limited by the experimental setup and not by the pump itself. The maximum pumping rate has not been explored. In the current design we expect that an upper boundary is most likely imposed by the heating of the PDMS and the liquid from the laser pulses causing an out-gassing of the liquid. Depending on the size and location residual gas bubbles might temporarily block the supply channels.

5.3.5 Parameter study

After reporting on the details of the pumping stroke we now change the easily accessible experimental parameters of the bubble pump, namely bubble size (R_{max}), distance from the upper channel entrance (h), and to some extent also the chamber geometry. For this study, separate bubbles are created at different locations on the center line of the channel starting at the straight upper wall ($h = 0\mu m$) and ending at the lower semicircular wall ($h = 200\mu m$). On the y-axis of Fig. 5.6 we plot the maximum displacement of the tracer particles in the supply channels. For distances $h < 100\mu m$ the displacement of particles in the upper channel is plotted whereas for $h > 100\mu m$ the particles in the lower channel are studied. Additionally, the laser energy is varied, which leads to three data sets with maximum radii of $R_{max} = 37.5\mu m$, $43.8\mu m$, and $50.0\mu m$ plotted as squares, diamonds, and circles, respectively. Although we dont know the energy absorbed in the liquid, the energy setting of the laser was increased by 50% and 100% to increase the bubble size for the latter two, respectively.

Let us first discuss the medium sized bubbles (diamonds in Fig. 5.6). Although there is some scatter in the data, we find two clear extremes for the maximum displacement, namely at $25\mu m$ and $170\mu m$. Thus optimum

#	$R_{max}/\mu m$	h/R_{max}	Pumpdirection	n	Strokefreq./Hz	$[\Delta x/\text{stroke}]/\mu m$
1	42 ± 1	0.69 ± 0.05	Down	8	1	2.3 ± 0.4
2	41 ± 1	0.52 ± 0.05	Up	8	1	2.5 ± 0.3
3	52 ± 1	0.69 ± 0.05	Down	8	1	4.9 ± 1.1
4	50 ± 1	0.64 ± 0.05	Up	9	1	3.9 ± 0.7
5	47 ± 1	0.59 ± 0.06	Down	7	5	5.4 ± 3.3
6	43 ± 1	0.57 ± 0.05	Up	9	5	4.1 ± 0.6

Table 5.1: Summary of the final liquid displacements achieved per stroke for bubbles with different sizes R_{max} and relative distances to the nearest channel opening h/R_{max}. Here a 200μm square chamber is connected to again a longer downwards channel and a shorter upwards channel. The number of particles tracked in each set is denoted by n.

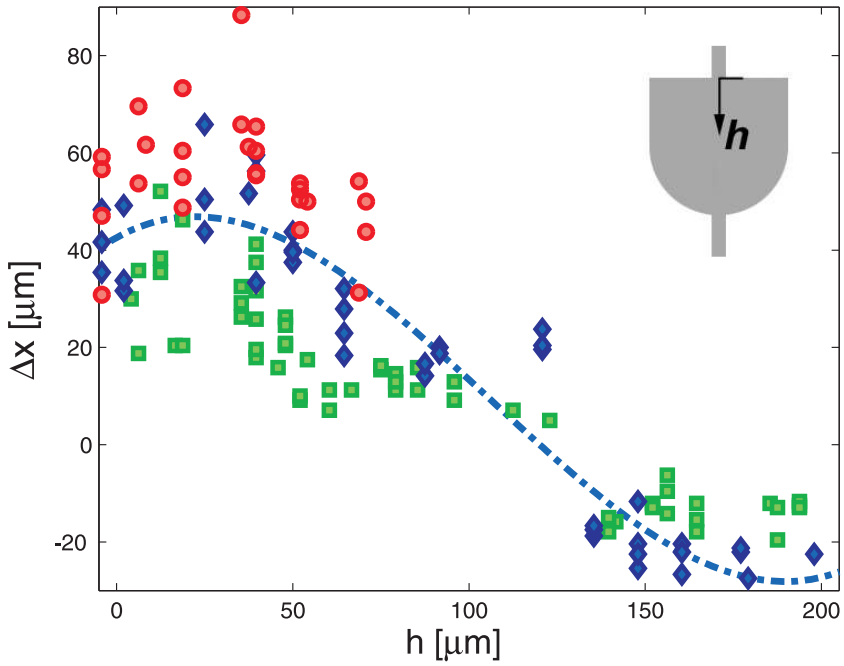

Figure 5.6: The maximum particle displacements (Δx) are plotted versus the position of the bubble generation, h, starting with 0 at the top channel, see sketch. The distance h is increased from $-5\mu m$ to the lower supply channel at $h = 200\mu m$. Half way through the chamber, $h = 100\mu m$, the pump switches direction and the maximum displacement of the particles in the lower channel are plotted.These measurements were done for three different bubble sizes ($R_{max} = 37\mu m$■, $44\mu m$♦, and $50\mu m$●). The dashed-dotted line is a third-order polynomial fit to the displacement from bubbles of $R_{max} = 44\mu m$.

pumping is observed when the bubble is created at about $30\mu m$ or about 80% of maximum bubble radius from the respective channel openings. The larger and smaller bubbles-circles and square, respectively-seem to support this 80% value.

Another interesting observation is that the maximum displacement for $h > 100\mu m$ (in the lower channel) is smaller than for $h < 100\mu m$ (in the upper channel); a larger displacement is found for the flat boundary.

This can be explained with a rounded boundary hindering the inflow from the sides more as compared to a flat boundary.

Another asymmetry of the system is the different channel lengths, see Fig. 5.1. Indeed an asymmetry in the channel lengths was exploited in the blinking bubble pump [12]. There however, the pumping was towards the channel with the higher resistance, which is opposite to our configuration; pumping occurs into the shorter channel. For our geometry we dont expect that this channel length difference affects the liquid displacement, which is also supported by the data presented in Table 5.1. In general larger bubbles show larger displacements per stroke independent of the direction of the pumping. Interestingly, the displacement at high stroke frequency increases (see sets 5 and 6 in Table 5.1); possibly some residual flow is generated or the liquid is heated up thus decreasing its viscosity. Clearly further experiments are needed to evaluate the limits of continuous pumping.

5.3.6 Comparison with unconstrained jetting pump

The bubble operated pump presented in this chapter is very much related to the jetting bubble pump invented by Khoo and Klaseboer (theory in ref. [18] and experiment in ref. [13]). In fact, the motivation of this work is to demonstrate that the jet based pumping mechanism works also in a lab-on-a-chip device. Yet, there are distinct differences in design and fluid dynamics. First, the pump of Khoo and Klaseboer operates in an infinite or very large container with millimeters sized bubbles, whereas here, the bubble is in the range of tens of micrometers and the bubble is constrained by an elastic material (PDMS). Our experimental data suggest that the chamber expands during the explosive growth and indents during bubble collapse. Thus, only some amount of the fluid displaced by the bubble is pumped into the channels; we estimated in the experiment shown in Fig. 5.4 about 10%.

After the bubble has disappeared the flow into the channel continues and increases to a maximum displacement after which it decreases again; this extremum has not been observed in Khoos and Klaseboers experiments [13], they did not find a flow reversal which is very evident in our experiments.

This back flow may be explained with the second difference between both experimental realizations: in the present work the pumping chamber is connected to long and thin supply channels, whereas a very short and thick connecting channel was used in the previous work. Thin chan-

nels, however, can be responsible for a significant viscous pressure head. Lets estimate a lower bound of this pressure head assuming cylindrical geometry and a developed flow, i.e. a Poiseuille flow. Thus, the pressure gradient dP/dx is given by

$$\frac{dP}{dx} = 4\mu u_{max} R^{-2}, \tag{5.1}$$

where μ is the dynamic viscosity $10^{-3} kg m^{-1} s^{-1}$, u_{max} the center velocity, and $R \approx 10 \mu m$ the channel diameter. A value for the center velocity is obtained from the maximum displacement, see Fig. 5.3, at time $t = 30 \mu s$ giving $u_{max} \approx 1.3 m s^{-1}$ and leading to a viscous pressure gradient of approx. $5.2 \times 10^7 Pa m^{-1}$. For a total channel length of $6.6 mm$ we obtain a considerable pressure head of about $3.4 bar$. This value is only a lower bound, as the flow field is not developed leading to larger velocity gradients at the channel boundaries.

We speculate that this pressure head leads to the observed quick stop of the flow and to the following flow reversal. Nevertheless, a net displacement and thus a pumping effect was observed which proves the applicability of cavitation based pumps in elastic microfluidic devices operating even against high viscous pressure heads of a few bars.

The advantage of using a laser to generate cavitation is that no additional manufacturing step in the PDMS chip fabrication is necessary, no mechanical or electrical connections are needed for operation, and already existing designs may be utilized. For operation the laser has to be focused on the wider side of a channel constriction. The main requirements are an optical transparent lab-on-a-chip and a means for conversion of the pulsed laser energy into a vapor bubble. This can be achieved either as presented here by using a laser-light absorbing dye or as demonstrated by Venugopalans group [2] by multiphoton ionization of the liquid. The phenomenon is based on high Reynolds number flows. Thus for more viscous liquids, adjustments to the geometry of the channel and/or size of the bubble are needed to allow for a cavitation based pump.

5.4 Conclusions

In conclusion we have demonstrated that single cavitation bubbles in microfluidics allows for the repeatable and precise control of picolitre volumes. The pumping effect utilizes a jetting phenomenon which has been studied and characterized with high-speed imaging.

For the inspected parameters optimum pumping was found when the distance between the laser focus and the channel inlet is about 80% of the maximum bubble radius. Additionally, continuous pumping has been demonstrated: for the maximum repetition rates tested which was 5Hz we obtained repeatable operation without the formation of residual gas bubbles. The technique presented in this article is already applicable for standard PDMS devices. We expect that further improvement in volume flux can be achieved with a modified channel layout. For example, Khoos and Klaseboers experiment [13] demonstrates that higher volume fluxes can be achieved for wider channels. Also very likely some of the back-flow can be eliminated by implementing diffuser type geometries along the channel, see ref. [10].

At last we want to mention, that by moving the laser beam to different locations, more complex pumping operations may be realized, for example, pumping liquids from one chamber into a set of branching channels. Here, the amount of pumped volume can be adjusted by the distance of the bubble to the channel or through the laser energy. The position of the laser focus may be selected by a switching mirror or through diffractive elements, for example spatial light modulators.

References

[1] H. P. Le, "Progress and trends in ink-jet printing," *J. Imaging Sci. Technol.* **42**, pp. 49 (1998).

[2] A. N. Hellman, K. R. Rau, H. H. Yoon, S. Bae, J. F. Palmer, K. S. Phillips, N. L. Allbritton, and V. Venugopalan, "Laser-Induced Mixing in Microfluidic Channels," *Anal. Chem.* **79**, pp. 4484 (2007).

[3] A. Vogel, J. Noack, G. Huttman, and G. Paltauf, "Mechanisms of femtosecond laser nanosurgery of cells and tissues," *Appl. Phys. B* **81**, pp. 1015 (2005).

[4] S. L. Gac, E. Zwaan, A. van den Berg, and C. D. Ohl, "Sonoporation of suspension cells with a single cavitation bubble in a microfluidic confinement," *Lab Chip* **7**, pp. 1666 (2007).

[5] M. W. Miller, D. L. Miller, and A. A. Brayman, "A review of in vitro bioeffects of inertial ultrasonic cavitation from a mechanistic perspective," *Ultrasound Med. Biol.* **22**, pp. 1131 (1996).

[6] C. Mishra and Y. Peles, "Flow visualization of cavitating flows through a rectangular slot micro-orifice ingrained in a microchannel," *Phys. Fluids* **17**, pp. 113602 (2005).

[7] B. W. Zeff, B. Kleber, J. Fineberg, and D. P. Lathrop, "Singularity dynamics in curvature collapse and jet eruption on a fluid surface," *Nature* **403**, pp. 401 (2000).

[8] E. Zwaan, S. L. Gac, K. Tsuji, and C. D. Ohl, "Controlled cavitation in microfluidic systems," *Phys. Rev. Lett.* **98**, pp. 254501 (2007).

[9] J. M. Ottino and S. Wiggins, "Introduction: Mixing in microfluidics," *Philos. Trans. R. Soc. Lond. A* **362**, pp. 923 (2004).

[10] J. H. Tsai and L. Lin, "A thermal-bubble-actuated micronozzle-diffuser pump," *J. Microelectromechanical Systems* **11**, pp. 665 (2002).

[11] Z. Yin and A. Prosperetti, "'Blinking bubble' micropump with microfabricated heaters," *J. Micromech. Microeng.* **15**, pp. 1683 (2005a).

[12] Z. Yin and A. Prosperetti, "A microfluidic 'blinking bubble' pump," *J. Micromech. Microeng.* **15**, pp. 643 (2005b).

[13] K. S. F. Lew, E. Klaseboer, and B. C. Khoo, "A collapsing bubble-induced micropump: An experimental study," *Sens. and Actuators A* **133**, pp. 161 (2007).

[14] J. R. Blake and D. C. Gibson, "Growth and collapse of a vapour cavity near a free surface," *J. Fluid Mech.* **111**, pp. 123 (1981).

[15] W. Lauterborn and H. Bolle, "Experimental investigations of cavitation-bubble collapse in the neighbourhood of a solid boundary," *J. Fluid Mech.* **72**, pp. 391 (1975).

[16] T. B. Benjamin and A. T. Ellis, "The Collapse of Cavitation Bubbles and the Pressures thereby Produced against Solid Boundaries," *Philos. Trans. R. Soc. Lond. A* **260**, pp. 221 (1966).

[17] Y. Tomita and A. Shima, "High-speed photographic observations of laser-induced cavitation bubbles in water," *Acustica* **71**, pp. 161 (1990).

[18] B. Khoo, E. Klaseboer, and K. Hung, "A collapsing bubble-induced micro-pump using the jetting effect," *Sens. and Actuators A* **118**, pp. 152 (2005).

6

Growth and collapse of a vapor bubble in a microtube : the role of thermal effect [‡]

The growth and collapse of a vapor bubble inside a microtube is studied both experimentally and theoretically. The length of the bubble, and the velocity and acceleration of its interface, are obtained from high-speed image recording (typically $1.25 \times 10^5 \mathrm{fps}$*) for various energy inputs and two tube diameters. To understand the underlying dynamics of the system, two theoretical models are compared with experiment. A model based on a discontinuous time-dependence of the vapor pressure inside the bubble is at variance with the data. It proves necessary to account in greater detail for the time dependence of the vapor pressure. A new model is proposed for this purpose which includes heat transfer in addition to inertia and viscous friction. Both the data and the model show that the vapor pressure decreases with time continuously instead of abruptly. The length, velocity and acceleration from the numerical simulations are found to be in good agreement with experimental data. Both the experiments and simulations clearly indicate that thermal effects play an important role throughout the*

[‡]In press as: Chao Sun, Edip Can, Rory Dijkink, Detlef Lohse and Andrea Prosperetti, *Growth and collapse of a vapor bubble in a microtube : the role of thermal effects*, J. Fluid Mech., (2009).

whole growth and collapse process.

6.1 Introduction

The dynamics of a free bubble has been studied extensively (see e.g. [1, 2, 3]) and it has been applied to a wide range of phenomena. The first studies devoted to bubbles in confined geometries were motivated by the development of ink-jet printing technology [4, 5, 6]. This early interest has been subsequently sustained by the rapid development of microfluidics (see e.g. [7, 8, 9]). Other applications have focused on the actuation properties of rapidly growing and collapsing bubbles. For example, the high liquid velocity induced by transient bubbles has been used to provide high-Reynolds number flow in microsystems [10]. [11, 12] have studied the dynamics of highly transient vapor bubbles in a tube and have demonstrated a pumping effect ([13, 14]; see also [15, 16]).

Here we study the growth and collapse of a vapor bubble inside a microtube both experimentally and theoretically. In previous studies [5, 13, 14], the vapor bubble was created using a thin-film heater at the tube surface. In the present work, the bubble is generated in the central region of a tube by focusing a laser pulse. The experiments are conducted varying the tube diameter and length and the laser energy. To increase heat absorption by the liquid, water mixed with dye is used.

The early models [11, 13, 14, 17] of these processes assumed that the high vapor pressure in the bubble caused by the initial heat pulse persisted only for a very short time and the subsequent dynamics was mostly governed by pressure and viscous effects. We find that these essentially mechanical models are inadequate to describe the observations and develop a new model which incorporates thermal effects.

6.2 Experimental setup

A sketch of the experimental setup, similar to the one used in the experiments of [18], is shown in Fig.6.1. Two glass microtubes were used in the experiments, one with an inner diameter of D = 50 μm, outer diameter 80 μm and length L = 27 mm, the other one with an inner diameter of 24.9 μm, outer diameter 80 μm and length 25 mm. For all experiments the same mixture of water and red food dye was used. The tubes were filled with the liquid, and both ends were covered by large droplets of the same

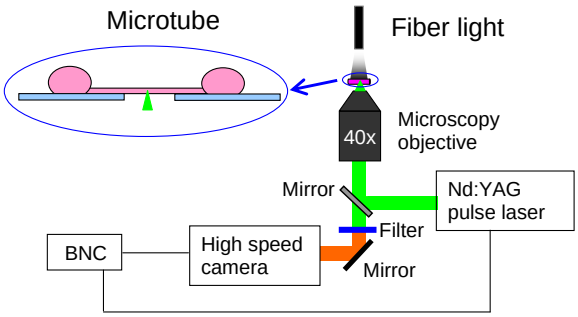

Figure 6.1: A sketch of the experimental setup.

solution (diameter ~ 5 mm) exposed at the atmosphere. The bubble was created at the midpoint of a microtube by focusing a laser pulse (Nd:YAG laser, Solo PIV, New Wave, Fremont, CA, USA) with a time duration of 6ns and a wavelength of 532nm by means of a $40\times$ objective. The energy of the laser varied from $27.6\mu\text{J}$ to $49.3\mu\text{J}$ for the $\text{D} = 50\mu\text{m}$ tube, and from $27.6\mu\text{J}$ to $56.3\mu\text{J}$ for the $\text{D} = 24.9\mu\text{m}$ tube. For calibrating energy, an energy meter (Gentec-eo XLE4) was fixed above the tubes. The energy absorbed by the working fluid was calibrated by measuring the difference of the energies after the empty glass tube and the glass tube filled with the working fluid. For the $\text{D} = 50\mu\text{m}$ tube, the absorbed energy varied from $6.5\mu\text{J}$ to $11.6\mu\text{J}$. The energy absorbed by the liquid in the $\text{D} = 24.9\mu\text{m}$ tube varied from $3.0\mu\text{J}$ to $6.1\mu\text{J}$.

A filter was used to block the reflected laser light to prevent damage to the camera. The motion of the bubble was recorded by a high speed camera with a maximum frame rate of 10^6 fps (HPV-1, Shimadzu Corp., Japan). In most of the experiments a lower speed, 1.25×10^5 fps proved sufficient. Illumination for the camera was provided by a fiber lamp (Olympus ILP-1) emitting a spectrum of light part of which passed through the filter to the camera. A digital delay generator (Berkeley Nucleonics Corp. CA, USA) was used to synchronize the camera and the laser.

6.3 Experimental results

Some representative frames taken during the evolution of the vapor bubble in the larger tube are shown in figure 6.2. The tube is initially full of water as shown in figure6.2 (a). The vapor bubble appears rapidly at the midpoint of the tube after the liquid absorbed $11.6\ \mu\text{J}$ from the laser pulse.

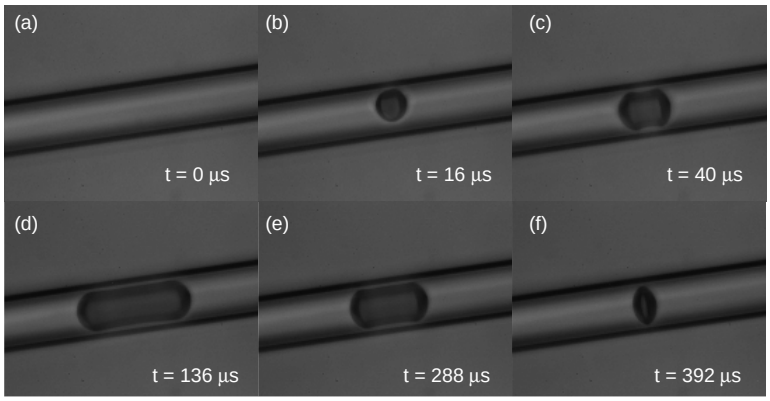

Figure 6.2: Representative frames of the vapor bubble evolution inside the microtube with an inner diameter 50 μm and length 27 mm; the absorbed laser energy is 11.6 μJ.

The bubble is initially a small sphere (figure 6.2(b)), it expands spherically until it nearly occupies the whole diameter of the tube, after which preferential growth in the axial direction begins (figure 6.2(c)). The shape of the bubble changes approximately to that of a cylinder occupying the majority of the cross section of the tube (figures 6.2(c,d,e)). A very thin liquid film on the tube wall, as expected from the no-slip condition on a hydrophilic surface, is barely visible in these pictures but with insufficient detail for a quantitative study. The appearance of the bubble during the expansion (figure 6.2(c)) and collapse (figure 6.2(e)) is similar except for the final stage (figure 6.2(f)), where it differs appreciably from its shape at the moment of formation (figure 6.2(b)). The final shape is oblate and the motion remains very nearly one-dimensional until the very end. For most of its duration, the bubble maintains a one-dimensional character, which makes a one-dimensional model a reasonable approximation.

By approximating the bubble as a cylinder, its length L_{bubble} along the axis of the tube and its diameter W can be extracted from the high-speed movies. By dividing the bubble volume $V_{bubble} = \pi W^2 L_{bubble}/4$ by the cross-section area of the microtube, we define an effective bubble length $L_{eff} = V_{bubble}/(\pi D^2/4)$. Since the system is symmetric with respect to the midpoint of the tube, we only consider half of L_{eff}. From here on, the 'bubble length' X refers to half of the real effective bubble length $X = L_{eff}/2$.

The time evolution of the measured bubble length X for different en-

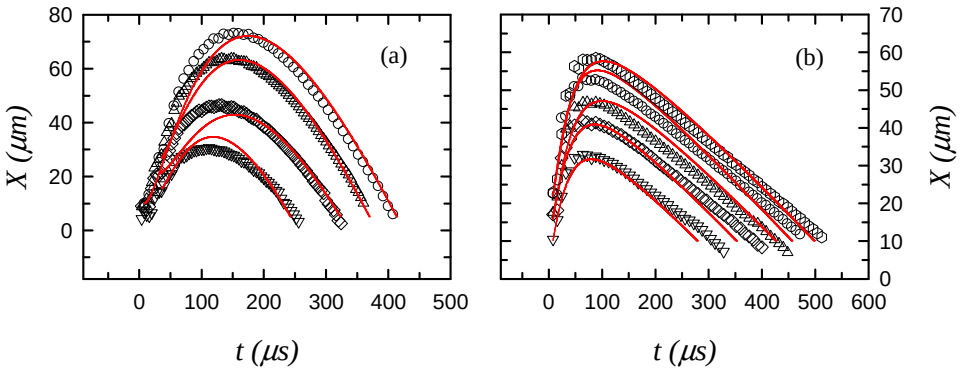

Figure 6.3: Time evolution of the bubble length X for different energy levels (a) in the tube with D = 50 μm; in descending order E = 11.6, 10.4, 8.2 and 6.5 μJ; (b) in the tube with D = 24.9 μm, for E = 6.1, 5.3, 4.8, 3.8 and 3.0 μJ. The open symbols are the experimental results and the lines are the results of the thermal model. See text for detailed parameters for the model.

ergy levels in the larger tube is plotted with open symbols in figure 6.3(a). In descending order, the absorbed energy is 11.6 μJ, 10.4 μJ, 8.18 μJ, 6.5 μJ respectively. The maximum bubble size and its lifetime increase with increasing energy. The overall trends of the X(t) curves for different energy levels are quite similar. The vapor bubble expands quickly, and shrinks more slowly after reaching its maximum size.

The contrast between growth and collapse is even sharper with the smaller tube. The bubble length versus time for different energy levels, in the smaller tube, is shown with open symbols in figure 6.3(b). More experimental runs were available with this tube and each X(t) curve shown is the result of averaging three different experiments under the same nominal conditions. Shot-to-shot reproducibility was however good. In descending order, the absorbed energy is 6.1 μJ, 5.3 μJ, 4.8 μJ, 3.8 μJ and 3.0 μJ, respectively. Again, the maximum length and the lifetime of the bubble increase with increasing energy and the overall trends of the X(t) curves for different energy levels are quite similar. The collapse of the bubble in this case proceeds much more slowly than its expansion. Unlike the larger tube case, the duration of the collapse process is about 10 times longer than that of the expansion.

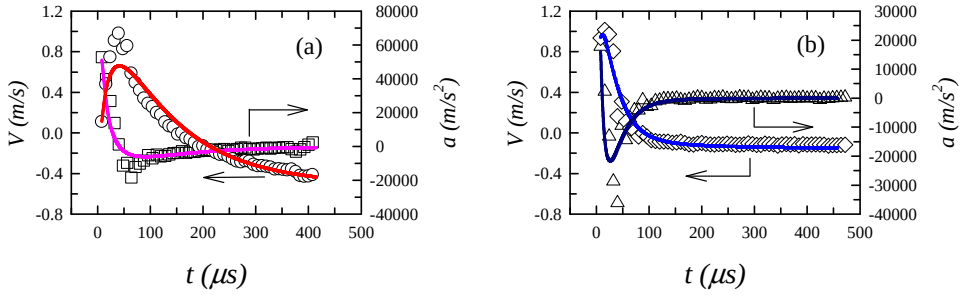

Figure 6.4: Velocity and acceleration of the interface versus time. (a) $D = 50\ \mu m$ with $E = 11.6\ \mu J$, and (b) $D = 24.9\ \mu m$ with $E = 5.3\ \mu J$. The open symbols are the experimental results and the lines the numerical results given by the thermal model.

To fit the measured $X(t)$, we used cubic splines from which the velocity and acceleration of the liquid/vapor interface can be extracted. The time dependence of the velocity in the larger tube is shown for $E = 11.6\ \mu J$ by the circles in figure 6.4 (a). The velocity of the interface increases quickly to a maximum around 1 m/s at $t \sim 40\ \mu s$, and then decreases continuously to a minimum value around -0.4 m/s where the bubble disappears. The time dependence of the velocity in the smaller tube, for $E = 5.3\ \mu J$, is shown by the open diamonds in figure 6.4 (b). The velocity of the interface increases to around 1 m/s at $t \sim 16\ \mu s$ and then decreases continuously. Since the very first instants of the bubble growth were too fast to be recorded, the first data readings that could be taken correspond to a finite velocity. The maximum velocity in the smaller tube is reached earlier than in the larger tube and the collapse velocity (0.2 m/s) is smaller than that in the larger tube (0.4 m/s).

The acceleration of the interface is also shown in figure 6.4 (a). Here the squares are for the larger tube with $E = 11.6\ \mu J$. The acceleration begins with a huge value around 55,000 m/s^2, then immediately becomes negative down to around $-10{,}000$ m/s^2, and finally increases again to a very small value. The huge value at the beginning is a remarkable feature which may be potentially useful in microfluidic systems. The acceleration of the interface in the smaller tube, with $E = 5.3\ \mu J$, is shown by the triangles in figure 6.4 (b). It begins with a positive value around 20,000 m/s^2, and decreases rapidly to a negative value around $-35{,}000$ m/s^2, af-

ter which it increases quickly to a very small value. The stronger deceleration for the thinner tube reflects the enhanced viscous forces on the small scale.

We now describe two simple theoretical models which are helpful to shed some light on these observations.

6.4 Theoretical models

As remarked before, the approximate one-dimensional nature of the bubble evolution suggests the possibility of using a simple one-dimensional model for its behavior which is sketched in figure 6.5. Here the left vertical line is the plane of symmetry at the midpoint of the tube which coincides with the center of the bubble. We are interested in the motion of the right vapor-liquid interface located at $X(t)$. If the pressure at the other end of the liquid column is a constant p_∞, the equation of motion of the liquid column in the tube is, approximately [17],

$$\ell_L \rho_L \frac{d^2X}{dt^2} = p_V(t) - P_\infty - \mathcal{R}\frac{dX}{dt} \tag{6.1}$$

Here ℓ_L is the length of the liquid column, which we keep constant and equal to half of the tube length given the smallness of the the bubble; p_V is the vapor pressure in the bubble and $\mathcal{R}$ represents the effect of viscous losses. By approximating the flow in the tube as quasi-steady fully developed Poiseuille flow, we model this term as $\mathcal{R} = 32\mu\ell_L/D^2$, in which μ is the liquid viscosity. This approximation is justified if the viscous diffusion length is comparable to, or larger than, the tube radius $D/2$, i.e. $2\sqrt{\nu\tau_b}/D \gtrsim 1$. With a bubble lifetime $\tau_b \simeq 400$ μs and $D = 50$ μm, this ratio is about 0.8. This value does not fully support the approximation, which will therefore tend to underestimate somewhat the true viscous loss. However the error may be expected to be moderate, which is supported by the results that will be shown later.

6.4.1 The step-function pressure model

In past work (see e.g. [11]) the dynamics of the bubble was modeled including inertia and viscosity but neglecting thermal effects. The pressure inside the bubble was taken equal to the vapor pressure of the liquid at the initial undisturbed temperature, except for a short interval $0 \leqslant t < \Delta t$

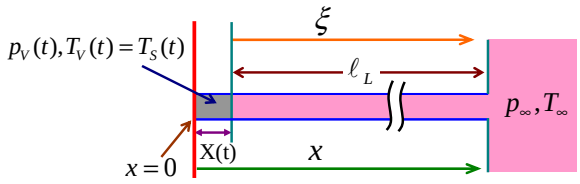

Figure 6.5: Conceptual sketch used in the formulation of the thermal

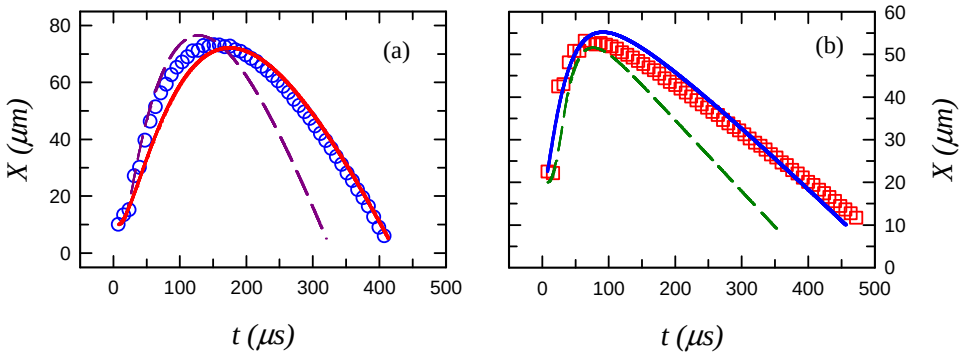

Figure 6.6: Comparison of the bubble length $X(t)$ vs. time as measured and predicted by the models for the cases (a) $D = 50$ μm and (b) $D = 24.9$ μm. The open symbols are the experimental results; the dashed lines are the predictions of the step-function pressure model and the solid lines those of the thermal model.

during which it was given a large value $p_0 + \Delta p$. We can now compare the predictions of this model with our data.

This simple model has two free parameters, Δp and the duration of the overpressure Δt. As suggested by the data to be shown later, we take the initial high pressure $p_V = p_0 + \Delta p = 10^6$ Pa and fit Δt so as to match approximately the observed maximum elongation of the bubbles in figures 6.3. For the larger tube (D =50 μm) and E = 11.6 μJ we take τ = 22 μs while, for the smaller tube (D =24.9 μm) with E = 5.3 μJ, we take τ = 25 μs. For $t > \Delta t$ the pressure inside the bubble falls to $p_V = p_V(25^oC)$ = 3.2×10^3 Pa. The initial bubble length for both cases was selected from experiment, $X(0)$ = 10 μm for D = 50 μm and $X(0)$ = 20 μm for D = 24.9 μm. The initial velocity for both cases was taken as 0.

The results of this step-function pressure model for the two cases are shown with the dashed lines in figure 6.6. The open symbols are the ex-

perimental data (a) $D = 50$ μm with $E = 11.6$ μJ and (b) $D = 24.9$ μm with $E = 5.3$ μJ. Although in a very general way some aspects of the observed bubble dynamics are reproduced, a major difference between this model and our data lies in the much faster collapse than in the experiment. This aspect cannot be changed by simply playing with the free parameters Δp, Δt and the initial velocity of the interface.

In order to get some insight into the failure of this model, we use the dynamic equation (6.1) in reverse to calculate p_V from the measured velocity and acceleration of the bubble interface. If we assume that the vapor is saturated, we can calculate the vapor temperature $T_S(t)$ from $p_V(t)$ by using the approximate relation

$$p_V = p_{V0} \exp\left[\frac{H_{Latent}}{R_v}\left(\frac{1}{T_0} - \frac{1}{T_S}\right)\right] \tag{6.2}$$

deduced from the Clausius-Clapeyron equation assuming a constant latent heat H_{Latent}; this approximation is legitimate over the limited temperature range of our experiment. In this equation R_v is the universal gas constant divided by the vapor mass; we take $p_{V0} = 10^5$ Pa and $T_0 = 100$ °C.

For $D = 50$ μm with $E = 11.6$ μJ, the results of these calculations are shown with open diamonds in figures 6.7 (a) and (b). The pressure starts at around 8 atm, which leads to the huge acceleration of the liquid column. The insert in figure 6.7 (a) is the vapor pressure versus time on an enlarged vertical scale, which clearly shows that the pressure decreases with time continuously instead of reaching a constant value. The corresponding vapor temperature is shown by the open triangles in figure 6.7(b). The temperature starts at 170 °C, and decreases continuously with time. A very surprising result is that at the end of the bubbles existence the temperature is still ~ 60 °C instead of the undisturbed liquid temperature ~ 25 °C. The similar trends of the vapor pressure and temperature in a smaller tube with $E = 5.3$ μJ are shown by open symbols in figures 6.7 (c) and (d).

This analysis shows that the previous model fails because it replaces the actual slow pressure fall by an abrupt decrease.

6.4.2 The thermal model

It is interesting to explore to what extent these data can be reproduced by complementing the mechanical model of equation (6.1) with a thermal

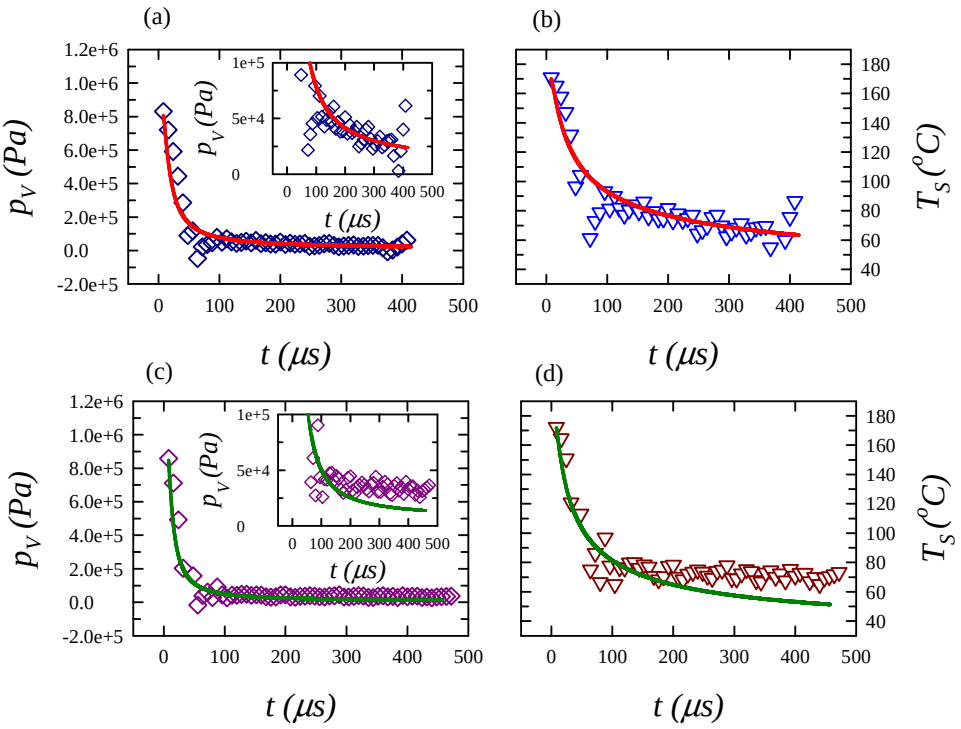

Figure 6.7: Vapor pressure and temperature vs. time for the larger tube with $E = 11.6$ μJ (a, b), and the smaller tube with $E = 5.3$ μJ (c, d). The open symbols are experimental results, the lines the thermal model predictions. The insert in (a) and (c) shows the vapor pressure vs. time on an enlarged vertical scale.

model. For this purpose we write an energy balance for the vapor in the following form (see e.g. [19]):

$$H_{Latent}\frac{d}{dt}(\rho_V X) = k\frac{\partial T}{\partial x}\bigg|_{x=X} - \rho_V c_s X\frac{dT_S}{dt} \tag{6.3}$$

The left-hand side of this equation is the latent heat associated with the vapor generation or condensation. The first term in the right-hand side, in which k is the thermal conductivity of the liquid, is the energy conducted to the vapor space from the liquid column. The last term, in which c_s is the specific heat along the saturation curve and $T_S(t) = T(X(t), t)$ is the temperature at the liquid surface, accounts for the energy necessary to maintain the vapor at saturation conditions; c_s is given by $c_s = c_{pV} - H_{Latent}/T_S$ in which c_{pV} is vapor specific heat [20].

In formulating the energy balance (6.3) we have assumed that the vapor is in spatially uniform conditions and that it exchanges energy by conduction with the liquid column but not with the tube wall. We will return to this point later.

The temperature change of the liquid column is controlled by the diffusion equation

$$\rho_L c_p \frac{\partial T}{\partial t} = k\frac{\partial^2 T}{\partial \xi} \tag{6.4}$$

where $\xi = x - X(t)$ and c_p is the liquid specific heat. This equation must be solved subject to the boundary conditions

$$T(\xi = 0, t) = T_S(t) \tag{6.5}$$

and

$$T(\xi = \ell_L, t) = T_\infty \tag{6.6}$$

In order to solve the liquid diffusion equation we also need to provide the initial temperature profile along the liquid column. This is a matter of considerable uncertainty because we do not have sufficient information on the spatial distribution of the absorbed laser energy. Furthermore, it is likely that the initial temperature distribution has a three-dimensional character which it is difficult to mimic with a one-dimensional model. Very close to the instant of bubble nucleation, we can envisage a small vapor nucleus surrounded by a hot liquid layer which thins as the vapor expands. By the time the bubble has grown to occupy the cross section

of the tube and the one-dimensional approximation becomes applicable, this layer will be adjacent to the bubble surface on the faces of the two liquid columns which bound it. On this basis, we postulate an initial temperature distribution given by

$$T(\xi) = T_\infty + (T_S(t_0) - T_\infty)\exp[-(\xi/2\delta)^2] \tag{6.7}$$

where $T_S(t_0)$ is the initial vapor temperature and δ is the thickness of the thermal layer surrounding the vapor space; we will use this quantity as a fitting parameter.

We start the integration attributing to the bubble the measured length and velocity at the first instant t_0 at which the movie record shows an effectively one-dimensional bubble near the beginning of each experiment. For the larger tube with $E = 11.6$ μJ, we take the data recorded at $t_0 = 8$ μs after the laser triggering: initial bubble size $X(t_0)$ = 10 μm, initial velocity $V(t_0) = 0.11$ m/s and initial vapor temperature $T_S(t_0)$ = 170 °C; the initial vapor pressure is calculated from initial vapor temperature according to equation (6.2) and is 8.07×10^5 Pa. Furthermore, ℓ_L is 13.5 mm, $p_\infty = 10^5$ Pa, $T_\infty = 25$ °C. By choosing the parameter $\delta = 2.9$ μm we find the bubble-length-versus-time shown by the solid line in figure 6.6 (a). The time dependence of the bubble size agrees well with experimental data (open circles). The velocity and acceleration of the interface, shown by the solid lines in figure 6.4 (a), also agree well with experiment.

The vapor pressure and temperature versus time are shown by the solid lines in figure 6.7 (a) and (b). Both predictions are seen to be consistent with the experiment. In particular, the model captures well the continuous decrease of these quantities. It is remarkable also that the final bubble temperature, ~ 60 °C, is reproduced by the model.

The actual heat exchange between the bubble and its surroundings is a complex problem for which too little information is available to permit the formulation of a faithful model. The thermal diffusion length over a time of 100 μs is about 4 μm, which is comparable with the thickness of the liquid film deposited on the tube wall, expected to be of the order of micrometers. This liquid layer is probably formed from the liquid heated by the laser pulse and therefore will have some initial energy content. It is therefore not clear whether the tube wall, which should be cold as it will not have absorbed energy from the laser, plays a role in the thermal exchange. In view of all these uncertainties, the one-dimensional thermal model used before may perhaps best be seen as a phenomenological model which appears nevertheless able to capture at least a good part of

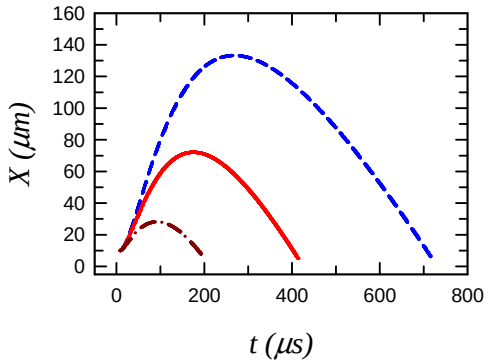

Figure 6.8: Calculated $X(t)$ curves for the thermal model with different values of the parameter δ for the larger tube with the same initial conditions as for $E = 11.6$ μJ; in descending order δ is 4.5, 2.9 and 1.5 μm. The middle line with δ = 2.9 μm is the best fit to the experimental data shown in figure 6.3 and 6.6.

the relevant physics. The importance of heat diffusion is brought into evidence by the sensitivity of the model to the value of the parameter δ. This point is illustrated in figure 6.8 which shows the bubble length vs. time as obtained with δ = 1.5, 2.9 and 4.5 μm.

The results of the model for the other cases of figure 6.3(a) are shown by the lines in the same figure. The initial conditions used in each case together with the corresponding value of δ for the larger tube with different energy levels are listed in table 6.1. At low laser energy it takes a few frames for the bubble to acquire a one-dimensional character and therefore t_0 is somewhat greater. The parameter δ does not change too much except for the lowest energy level. The solid lines in figure 6.3 (a) are the calculated bubble length versus time. A reasonably good agreement is apparent for each energy level. Only at the lower value of the energy does the model start to show some noticeable discrepancy with experiment, presumably because the one-dimensional approximation becomes invalid.

As a typical example for the smaller tube we consider the case with $E = 5.3$ μJ, again taking as the initial conditions the data: $t_0 = 8$ μs, initial velocity $V(t_0)$ = 0.94 m/s, initial bubble size $X(t_0)$ = 22.5 μm, initial vapor temperature $T_S(t_0)$ = 172.0 °C and initial vapor pressure $p_V(t_0) = 8.48 \times 10^5$ Pa. Furthermore, ℓ_L is 12.5 mm with p_∞ and T_∞ as before. A reasonable fit to the data is obtained by taking $\delta = 1.8$ μm. The bubble length versus time calculated from the thermal model is shown by the solid line

D (μm)	E (μJ)	$X(t_0)$ (μm)	$V(t_0)$ (m/s)	$T_S(t_0)$ (°C)	δ (μm)
50	11.6	10.0	0.11	170.0	2.9
	10.4	26.7	0.42	134.7	3.1
	8.2	21.0	0.11	135.7	3.6
	6.5	15.5	0.33	141.3	1.9
24.9	6.1	21.9	0.77	179.4	1.9
	5.3	22.5	0.94	172.0	1.8
	4.8	16.9	0.67	172.7	2.2
	3.8	15.7	0.77	163.2	2.1
	3.0	10.1	0.80	151.2	2.4

Table 6.1: The initial conditions and the respective fitting parameter δ of the thermal model for different energy levels.

in figure 6.6 (b). The bubble size versus time again agrees very well with experiment (open squares). The velocity and acceleration of the interface are shown by the solid lines in figure 6.4 (b) and they are both seen to be consistent with experiment. The vapor pressure and temperature versus time in this case are shown by the solid lines in figure 6.7 (c) and (d). Both predictions are seen to be consistent with the experiment. Although they are not in precise agreement with the experiment, the overall trends are well captured by the model.

The performance of the model for the other experiments in figure 6.3 (b) is shown by the solid lines in the same figure. The initial conditions and the respective values of δ are listed in table 6.1. The δ-values for different energy levels are quite close, ranging between 1.8 and 2.4 μm. The comparisons between the experiments (open symbols) and the results shows a very good agreement for all energy levels.

6.4.3 Energy partition

The present model contains both mechanical and thermal aspects and it is interesting to examine how the energy is apportioned among the different components. Let us consider the larger tube $D = 50$ μm with an absorbed energy $E = 11.6$ μJ. From figure 6.4 the maximum velocity is 0.98 m/s; the corresponding kinetic energy is $2(\frac{1}{2}\rho_L S\ell_L \dot{X}^2) \simeq 0.025$ μJ, where $S = \pi D^2/4$ is the tube cross section and the factor of 2 accounts for both

liquid columns. The instantaneous viscous energy dissipated is $2\mathcal{R}S\dot{X}^2\Delta t$, and $2\mathcal{R}S\dot{X}^2$ evaluated at the maximum velocity is 576 μJ/s. No matter what value of Δt is selected, this energy term is negligible. If we take Δt = 100 μs, $2\mathcal{R}S\dot{X}^2\Delta t$ = 0.058 μJ. Both these mechanical energies are much smaller than the laser energy absorbed by the liquid.

The total latent heat necessary to keep the bubble filled with saturated vapor at the point of its maximum volume is $2S\rho_V H_{latent} X_{max}$. At maximum expansion $T_S = 79\ ^\circ C$, $\rho_V = 0.29\ kg/m^3$, $X_{max} = 72\ \mu m$ so that $2S\rho_V H_{latent} X_{max}$ = 0.18 μJ, which is also much smaller than the 11.6 μJ absorbed by the liquid. Where is the other energy? The answer is that most of the laser energy has gone into heating up the liquid. The energy required to generate the temperature distribution (6.7) is

$$2\int_0^{\ell_L} (T_S(t_0) - T_\infty) \exp[-(\xi/2\delta)^2] c_p \rho S \, d\xi \tag{6.8}$$

Evaluating this integral using δ = 2.9 μm, $T_S(t_0)$ = 170 °C, we find ~11.7 μJ, which is quite close to the laser energy input.

6.5 Conclusions

The dynamics of a laser-generated vapor bubble in microtubes with different diameters has been studied experimentally and theoretically. A pure inertia-driven model, neglecting thermal effects, failed to capture quantitatively the growth and collapse of the bubble. A new model was developed by considering heat transfer in addition to inertia and viscosity. This model has proved to be capable of reproducing the observed behavior of the bubble. It is concluded that thermal effects play an essential role during the whole process of growth and collapse.

References

[1] C. Brennen, *Cavitation and Bubble Dynamics* (Oxford University, Oxford, 1995).

[2] M. Brenner, S. Hilgenfeldt, and D. Lohse, "Single-bubble sonoluminescence," *Rev. Mod. Phys.* **74**, pp. 425 (2002).

[3] M. S. Plesset and A. Prosperetti, "Bubble Dynamics and Cavitation," *Ann. Rev. Fluid Mech.* **9**, pp. 145 (1977).

[4] R. R. Allen, J. D. Meyer, and W. R. Knight, "Thermodynamics and Hydrodynamics of the Thermal Ink Jets," *Hewlett-Packard J.* **36**, pp. 21 (1985).

[5] A. Asai, "Application of the Nucleation Theory to the Design of Bubble Jet Printers," *Jpn. J. Appl. Phys.* **28**, pp. 909 (1989).

[6] A. Asai, "Bubble dynamics in boiling under high heat flux pulse heating," *J. Heat Transfer* **113**, pp. 973 (1991).

[7] V. S. Ajaev and G. M. Homsy, "Modeling shapes and dynamics of confined bubbles," *Ann. Rev. Fluid Mech.* **38**, pp. 277 (2006).

[8] V. S. Ajaev, G. M. Homsy, and S. J. S. Morris, "Dynamic Response of Geometrically Constrained Vapor Bubbles," *J. Colloid Interface Sci.* **254**, pp. 346 (2002).

[9] A. Mazouchi and G. M. Homsy, "Thermocapillary migration of long bubbles in cylindrical capillary tubes," *Phys. Fluids* **12**, pp. 542 (2000).

[10] C. D. Ohl, M. Arora, R. Dijkink, V. Janve, and D. Lohse, "Surface cleaning from laser-induced cavitation bubbles," *Appl. Phys. Lett.* **89**, pp. 74102 (2006).

[11] E. Ory, H. Yuan, A. Prosperetti, S. Popinet, and S. Zaleski, "Growth and collapse of a vapor bubble in a narrow tube," *Phys. Fluids* **12**, pp. 1268 (2000).

[12] H. Yuan and A. Prosperetti, "The pumping effect of growing and collapsing bubbles in a tube," *J. Micromech. Microeng.* **9**, pp. 402 (1999).

[13] Z. Yin and A. Prosperetti, "'Blinking bubble' micropump with microfabricated heaters," *J. Micromech. Microeng.* **15**, pp. 1683 (2005a).

[14] Z. Yin and A. Prosperetti, "A microfluidic 'blinking bubble' pump," *J. Micromech. Microeng.* **15**, pp. 643 (2005b).

[15] T. K. Jun and C.-J. Kim, "Microscale Pumping with Traversing Bubbles in Microchannels," *Solid-State Sensors and Actuator Workshop (Hilton Head Island)* pp. 144–147 (1996).

[16] T. K. Jun and C.-J. Kim, "Valveless pumping using traversing vapor bubbles in microchannels," *J. Appl. Phys.* **83**, pp. 5658 (1998).

[17] Z. Yin, A. Prosperetti, and J. Kim, "Bubble growth on an impulsively powered microheater," *Int. J. Heat Mass Transfer* **47**, pp. 1053 (2004).

[18] E. Zwaan, S. L. Gac, K. Tsuji, and C. D. Ohl, "Controlled cavitation in microfluidic systems," *Phys. Rev. Lett.* **98**, pp. 254501 (2007).

[19] B. Yang and A. Prosperetti, "Vapour bubble collapse in isothermal and non-isothermal liquids," *J. Fluid Mech.* **601**, pp. 253 (2008).

[20] L. D. Landau and E. M. Lifshitz, *Statistical Physics* (Pergamon press, Oxford, 1980).

7

Cavitation induced high speed jetting from a microtube

‡

The growth of a vapor bubble just inside an open end of a microtube can accelerate liquid into a jet with speeds up to $110\,\mathrm{m/s}$*. High-speed imaging (at a speed of* $10^6\,\mathrm{fps}$*) is used track the cavity developing inside the tube and the jet emerging from the tube. The cavitation bubble is created using a focused* $6\,\mathrm{ns}$ *laser pulse. The effect of both the distance between the focus and the end of the tube and the amount of laser energy used is studied. The jet speed depends strongly on the laser energy but an upper limit was found around* $110\,\mathrm{m/s}$*. These speeds are similar to the speeds reported for jets developing inside cavitation bubbles and therefore this setup is suggested as a model to study high-speed jets similar in size and velocity as they are occurring within a cavitation bubble collapsing close to a boundary.*

7.1 Introduction

The previous chapter discussed a cavitation bubble created in a capillary. As the cylindrical bubble was much longer than it was thick it can be approximated as a 1 dimensional bubble. The bubble was created in the

‡in preparation for Physics of Fluids.

middle of a long capillary submerged in liquid at both ends.

This chapter explores what happens when the same bubble is created close to an open end of the tube. Thus, it is not submerged as in the previous experiments but situated in air.

The asymmetry in the viscous pressure head will cause the bubble expansion to be directed mainly towards the open end of the tube forcing the liquid between the nucleation point of the bubble and the open end. As the bubble expands explosively the ejected liquid accelerates into a jet with speeds up to $110\mathrm{m}/\mathrm{s}$. In this chapter we study and discuss the experimental observation of these high-speed and micrometer thick jets.

Similar jets in size and speed have been observed inside collapsing cavitation bubbles and have been subject of numerous studies (e.g. [1, 2, 3, 4]). These jet velocities are in the range of jet velocities measured inside millimeter sized cavitation bubbles [5]. Besides the reentrant jet a cavitation bubble near a solid boundary also generates a vortex ring [6]. Together with the volume oscillation and the bubble's displacement towards the boundary this makes for a complex fluid dynamic system . The tube jet could be a way to decouple the jet from the rest of the bubble dynamics thus making it possible to study the role of only the jet in cavitation processes like: cavitation erosion [5], ultrasonic cleaning [7] and sonoporation (see chapter 3).

7.2 Experimental setup

A sketch of the experimental setup, similar to the one used in the previous chapter, is shown in Fig.7.1. The main difference being the capillary which has an inner diameter of $20\mu\mathrm{m}$ and one end open in air (Hilgenberg GmbH, Malsfeld, Germany). The other side of capillary is glued into a syringe needle to allow easy mounting and filling. By connecting the needle to a vertical liquid filled reservoir, hydrostatic pressure ensures that the capillary is always completely filled.

A $6\mathrm{n}\mathrm{s}$ laser pulse (Nd:YAG laser @$532\mathrm{n}\mathrm{m}$, Solo PIV, New Wave, Fremont, CA, USA) is focussed into the capillary to create a cavitation bubble. The laser energy is calibrated using a laser energy detector (XLE4, Gentec-eo, Quebec, Canada). The liquid used in these experiments is red printer ink to facilitate an optimal absorption of the green laser light. An inverted microscope (Axiovert CF 40, Zeiss, Goettingen, Germany) is used to focus the laser pulse and guide it into the microtube.

A second microscope with a larger field of view (SZX12, Olympus, To-

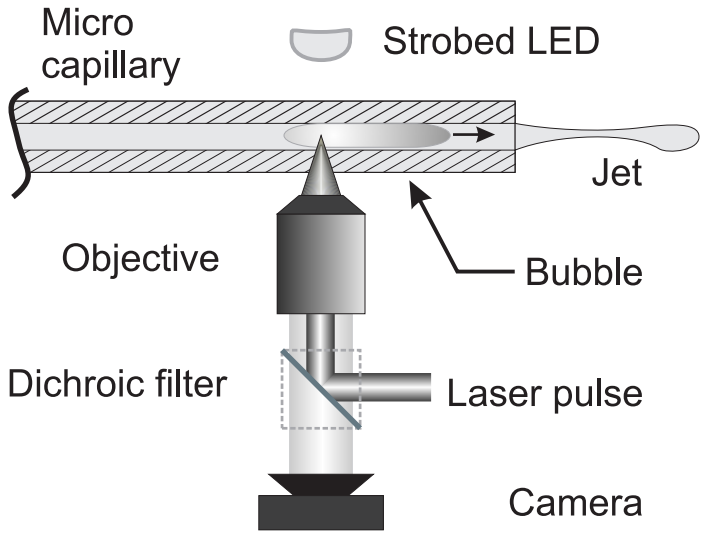

Figure 7.1: Depicted is a schematic overview of the setup. A laser pulse is focussed into a thin capillary creating a cavitation bubble. As the bubble expands it pushes liquid out of the nearby open end of the tube. A strobed LED and a single frame camera are used to make control images of the bubble. Not shown are the high-speed camera and high-intensity flash source used to record the jet in time.

kyo, Japan) is used to image the jet emerging from tube. Recordings at $10^6 \mathrm{fps}$ are made using a high-speed camera (HPV-1, Shimadzu Corp., Japan) and a high intensity flash lamp. The duration of the flash is approximately $40\mu\mathrm{s}$, but as most jets leave the frame within that time it is deemed sufficient.

7.3 Results

7.3.1 A single jet

By creating the bubble close to the open end of the capillary the expanding cavity will eject liquid from the tube creating a jet. The dependence of the jet speed on laser energy and distance between the tube end and the laser focus are investigated.

First we will look at a single jet, the frames from a high-speed movie

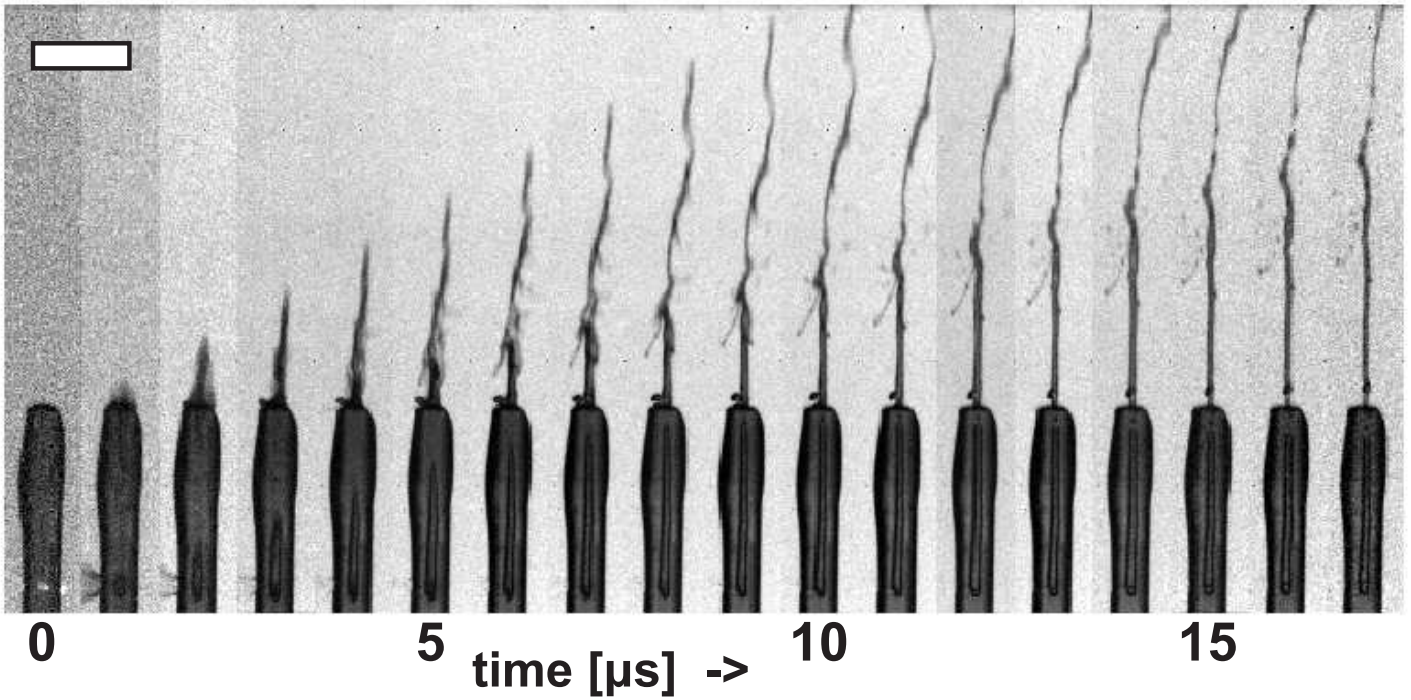

Figure 7.2: Shown here are the frames from a high speed recording of a jet being ejected out of a capillary by an expanding cavitation bubble. Cavitation inception takes place at $t = 0\mu s$ as a result of a $24.4\mu J$ laser pulse. The capillary has an inner diameter of $20\mu m$ and an outer diameter of $80\mu m$. For reference a $200\mu m$ scalebar is added to the top left corner.

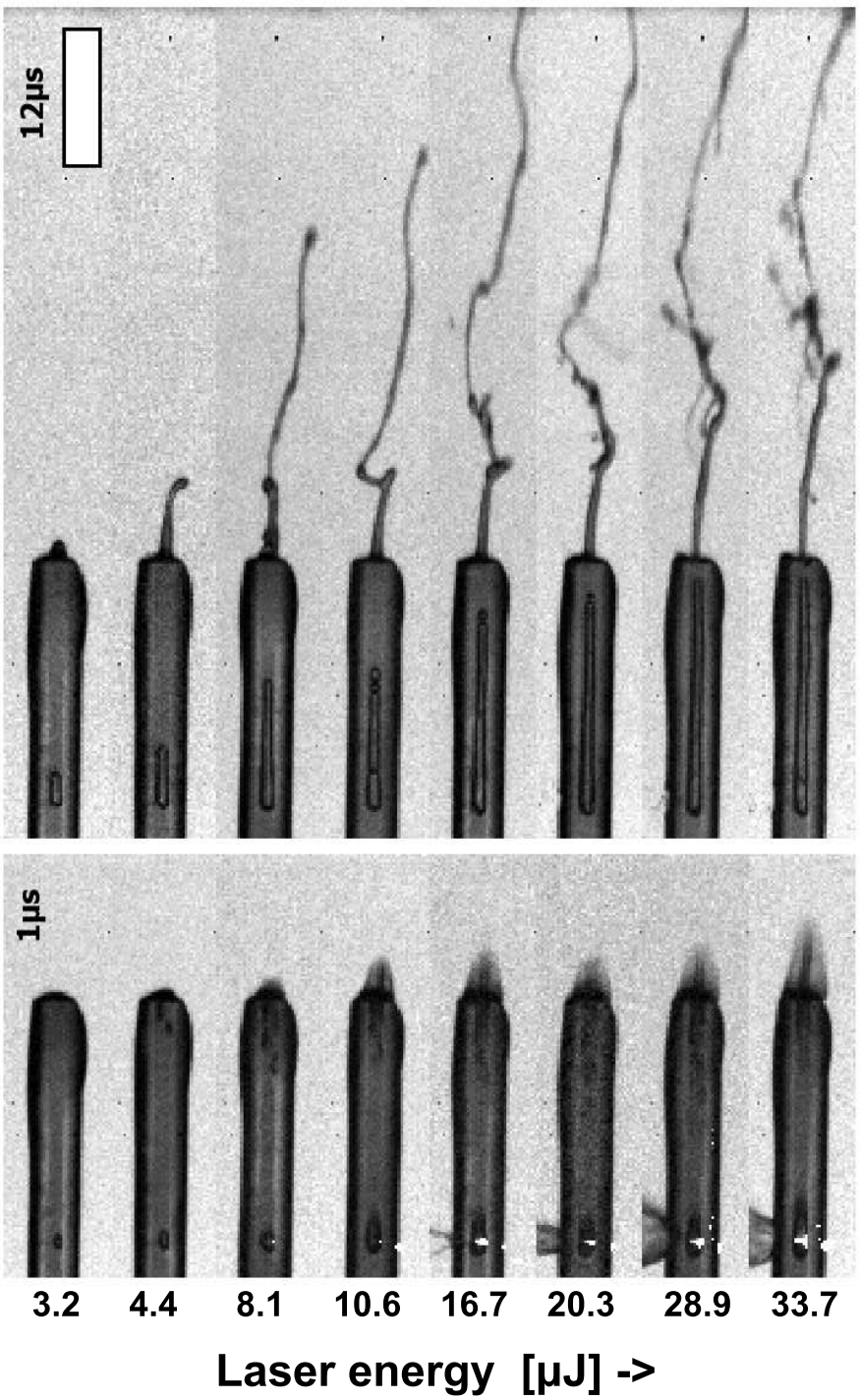

Figure 7.3: The bubbles and jets created by laser pulses with increasing levels of energy are shown at 1 and 8µs after cavitation inception. The left column also shows a secondary cavitation event at the opening of the capillary for all but the upper most tube. The white bar in the top right corner denotes 200µm.

are shown next to each other in fig. 7.2. The bubble can first be seen in the second frame and consecutively grows at an approximately constant speed until it reaches the end of the tube between 8 and 9μs after cavitation inception. Upon connecting with the surrounding air the internal vapor pressure in the bubble will instantly equalize with the atmospheric pressure. With the sudden drop in pressure the bubble closes of again and slow starts to shrink as the vapor remaining inside starts to cool down and condensate.

The frames also show that the bubble only grows in the the direction of the open end of the tube pushing the intervening liquid out.

The liquid is then ejected from the tube and forms a jet. The tip of the jet can already be seen in the same frame as where the bubble is first visible, i.e. 1μs. Same as with the bubble the tip of the jet immediately acquires its maximum velocity and exits the frame after 10μs. Interestingly enough as the front part of the jet is shooting away a second jet emerges from the tube opening. The first part is thin, irregular and faster than the second section which is thicker and remains straight for the rest of the frameset in fig. 7.2. A straight forward hypothesis is that there are two mechanisms at work responsible for the two different parts of the jet.

7.3.2 The role of laser energy

To further investigate the underlying physics of the jet structure fig. 7.3 shows the frames at 1μs and 12μs for 8 jets all created with different laser energies. The later frames in the right column show that only the lower 6 experiments developed the thin fast jet. The mechanism behind the thin jet could be a secondary cavitation event, the frames taken 1μs after the laser pulse show blurry black structures just inside the opening of the tube.

Cavitation is usually accompanied by shockwave emission. The quasi 1 dimensional nature of the system could mean that the shockwave becomes guided by the capillary an may only attenuate weakly with distance. When the shockwave reflects at the liquid air interface it comes back to overlap with it's tail. The negative pressures associated with this could be strong enough to cavitate the liquid resulting in the dark structure which possibly is depicting a single or multiple bubbles (seen the left column of figure 7.3).

The reflection of the shock wave may lead to fine spray and later as the bubble collapse close to the interface to a fine jet [8]. Due to the low pressure close to the fast jet the spray is sucked towards the jet. The expansion

of the primary cavity which happens on a much longer time scale is then responsible for the thick jet that emerges after the collapse of the surface cavitation. The fact that the velocity of the thick jet and the expansion velocity of the bubble are roughly the same strengthens our hypothesis of a complex interaction of shock waves, cavitation, and jetting.

7.3.3 Location of the laser focus

Next we investigate how the position of the laser focus effects the jetting. Figure 7.4 depicts images of 4 jets with similar laser energies but different focus locations. At this energy all distances show the blur of the secondary cavitation at the open end of the capillary (see the left column of frames in fig 7.4).

The column of frames on the right shows the jets 8μs after cavitation inception. The four jets differ quite a lot, the bottom most jet is the same as in figure 7.2 and both the crude thin and the straight thick part of the jet have been discussed. Moving the laser focus a bit closer to the tube end we see again a thin jet but the straight second section seems to be missing. There is some change from a thin to a thicker jet but the thick part is by no means straight.

Moving even closer we get the jet from the second row of frames. The secondary cavitation event is to small to create a thin jet similar to the second low energy jet from figure 7.3 and the jet due to the expansion of the primary cavitation bubble is no longer a clean straight jet. It also lags behind the the rest in speed which could be a result of these parameters. Another option is that the amount of laser light entering the tube is significantly lower. The movie frames sometimes show a bulge around the tube near the end, this is the result of ink slowly seeping out and wetting the exterior of the capillary. Evidence for this can be found in the splashes erupting from the sides of the tube above and sometimes below the tube. As the laser pulse enter from below a splash on top is no problem but the second frame in the left column also show a downward splash meaning that laser energy was absorbed before the pulse could even enter the capillary.

The capillary was wiped just before each experiment but the short time in between is enough for a small buildup of ink. For the experiments further away from the tube opening there was no problem as the focus was beyond the bulge of ink.

Finally the top frames show the closest position of the focus. The primary bubble expands all the way out of the tube in approximately 2μs

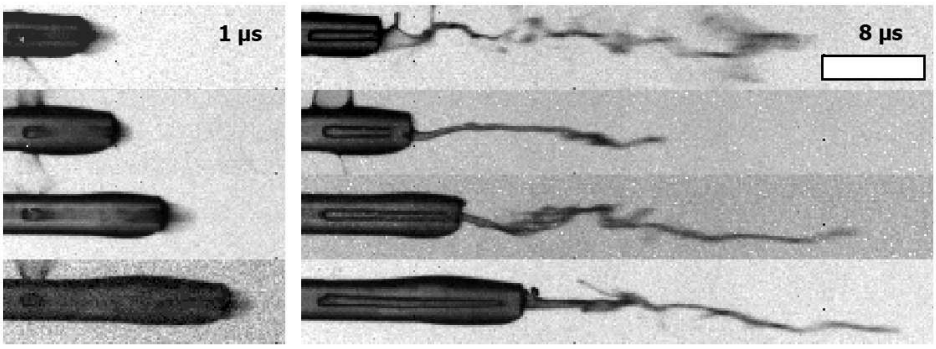

Figure 7.4: The bubbles and jets created by 24.4µJ laser pulses with increasing distance from the opening of the tube are shown at 1 and 8µs after cavitation inception. The left column also shows the secondary cavitation event at the opening of the capillary. For reference the white bar in the top right corner denotes 200µm.

leaving little time or room for a secondary cavitation event. The result is the most chaotic jet yet, looking less like a jet and more like a directed splash.

7.3.4 The jet velocity

Even though the four jets from figure 7.4 show different structures all the jets, with the exception of number 2, traverse about the same distance in the 8µs between frames. Therefore it might be interesting to look at the speeds of the jets. For this we used the very tip of the jet and don't differentiate between the further dynamics of the jet. Figure 7.5 shows the jet tip velocity plotted against the energy of the laser pulse for four sets of different laser-focus to tube-end distances.

There is a good amount of scatter in the data but mostly in the set at 168µm which was previously identified as the distance that is affected the strongest by the ink bulge on the exterior of the tube. The scatter in the other sets is much less and only in the direction of lower velocities. There is a sharp upper boundary to the data points and this boundary is approximately the same for all the sets. As the image comparing jets from these four sets already showed the dependence of the jet velocity on the location of cavitation inception is minimal.

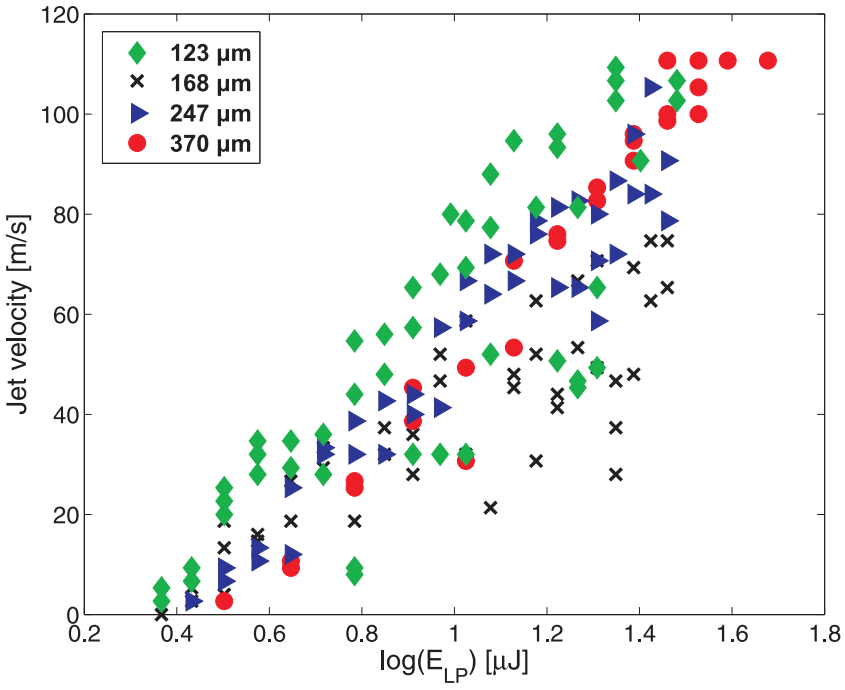

Figure 7.5: The velocity of the jet-tip is shown for different focus positions and laser energies. The focus positions is relative to the end of the tube and shown here are sets at 123µm (diamonds), 168µm (crosses), 247µm (triangles) and 370µm (circles).

Surprisingly the sets at 1233µm and 370µm both also show a second limit: at very high energies the velocity ceases to increase any further but remains at a constant value. A possible reason could be an error in image analysis but re-check by eye verified the analysis. A terminal velocity for jets in air seems unlikely which leaves a stagnation in the driving force as most likely option. To check if a similar behavior occurs for the bubble expansion the bubble length is tracked.

For practical reasons (i.e. this set reaches the highest laser energies and with the longer tube has more frames of bubble growth that can be tracked) only the bubbles at 370µm are tracked. A selection of tracks is shown in figure 7.6 where the arrow denotes the direction the curves evolve to for increasing laser energy. The low energy curves all show the

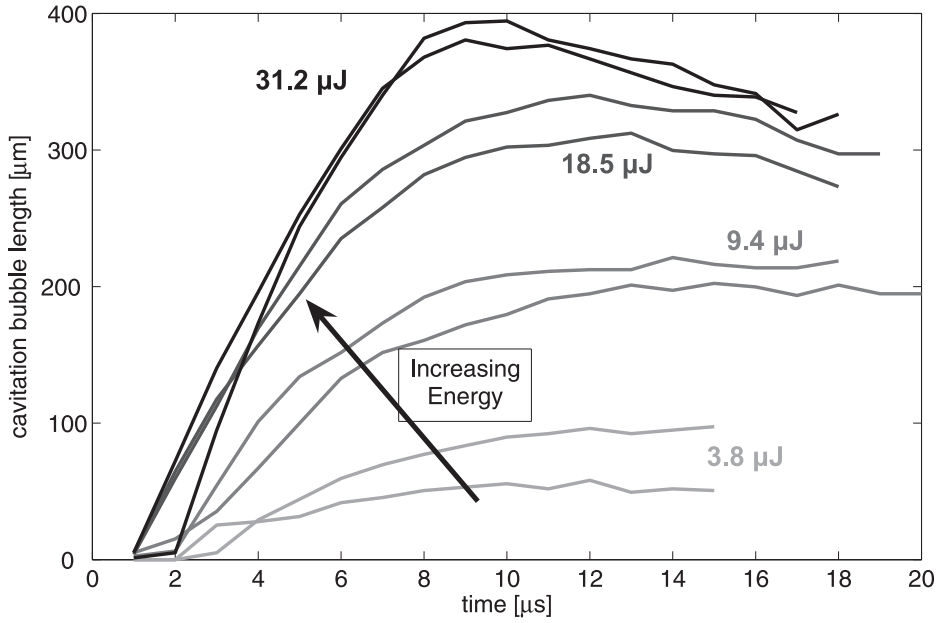

Figure 7.6: The length of the primary cavitation bubble plotted against time. the different curves represent bubbles created with different laser energies. The arrow shows the direction the curves move for increasing laser energy

bubble growth slowing down and then stopping but at high energy the curve becomes straight for the first part of the bubble expansion. The highest energy even reaches a constant expansion rate until the bubble vents its vapor pressure when it connects with the surrounding air at the end of the tube.

The black curves are the maximum rate of bubble expansion and all bubbles with higher energy fall on top of these curves. The limit on expansion rate is reached at the same energy when the jet speeds stagnate suggesting a direct dependence of jet speed on the bubble.

7.4 Conclusion

In this chapter we investigated cavitation bubbles created near the end of a long capillary. As a result of the rapid expansion of the bubble a thin jet

of liquid is ejected from the end of the capillary. Velocities up to $110\mathrm{m}/\mathrm{s}$ have been measured.

In most cases the shape of the jet is far from straight with ligaments branching of from the main jet. With time the ligaments and the jet itself will break up into a spray of small droplets [9, 10]. High velocity sprays and droplet impacts measurements are still few [11] but are of great interest as they can cause erosion for instance in steam turbines and in the aerospace industry with the impact of rain drops on planes flying at high velocities [12, 13]. Sprays and high velocity drops can also be used for cleaning or to cut surfaces [14].

The thin jet is most likely the result of shockwave reflection at the free interface [15]. Submerging the tube end gets rid of the interface and thus should leave just the thicker smooth jet though the jet will be much slower.

References

[1] T. B. Benjamin and A. T. Ellis, "The Collapse of Cavitation Bubbles and the Pressures thereby Produced against Solid Boundaries," *Philos. Trans. R. Soc. Lond. A* **260**, pp. 221 (1966).

[2] J. R. Blake and D. C. Gibson, "Cavitation bubbles near boundaries," *Ann. Rev. Fluid Mech.* **19**, pp. 99 (1987).

[3] Y. Tomita and A. Shima, "High-speed photographic observations of laser-induced cavitation bubbles in water," *Acustica* **71**, pp. 161 (1990).

[4] O. Lindau and W. Lauterborn, "Cinematographic observation of the collapse and rebound of a laser-produced cavitation bubble near a wall," *J. Fluid Mech.* **479**, pp. 327 (2003).

[5] A. Philipp and W. Lauterborn, "Cavitation erosion by single laser-produced bubbles," *J. Fluid Mech.* **361**, pp. 75 (1998).

[6] A. Vogel, W. Lauterborn, and R. Timm, "Optical and acoustic investigations of the dynamics of laser-produced cavitation bubbles near a solid boundary," *J. Fluid Mech.* **206**, pp. 299 (1989).

[7] D. Krefting, R. Mettin, and W. Lauterborn, "High-speed observation of acoustic cavitation erosion in multibubble systems," *Ultrason. Sonochem.* **11**, pp. 119 (2004).

[8] J. R. Blake and D. C. Gibson, "Growth and collapse of a vapour cavity near a free surface," *J. Fluid Mech.* **111**, pp. 123 (1981).

[9] E. Villermaux, P. Marmottant, and J. Duplat, "Ligament-mediated spray formation," *Phys. Rev. Lett.* **92**, pp. 074501 (2004).

[10] J. Eggers, "Nonlinear dynamics and breakup of free-surface flows," *Rev. Mod. Phys.* **69**, pp. 865 (1997).

[11] A. V. Chizhov and A. A. Schmidt, "Impact of a high-velocity drop on an obstacle," *Tech. Phys.* **45**, pp. 1529 (2000).

[12] F. J. Heymann, "High-Speed Impact between a Liquid Drop and a Solid Surface," *J. Appl. Phys.* **40**, pp. 5113 (1969).

[13] M. Rein, "Phenomena of liquid drop impact on solid and liquid surfaces," *Fluid Dyn. Res.* **12**, pp. 61 (1993).

[14] N. K. Bourne, "On Impacting Liquid Jets and Drops onto Polymethylmethacrylate Targets," *P. Roy. Soc. Lond. A Mat.* **461**, pp. 1129 (2005).

[15] A. Zijlstra and C. D. Ohl, in *Proceedings of 19th International Congress on Acoustics - Madrid* (2007).

8 Conclusions

This thesis deals with the utilization of cavitation bubble dynamics for on small scales, in particular for the ulization in microfluidics and for drug delivery. The general theme of this work is the formation and interaction of a thin but very fast liquid jet. It is the key contributor for the cell membrane poration (Chapter 3). Therefore, we study it in detail and present novel measurements of the the wall shear stress (Chapter 2). The jet is utilized in microfluidics to pump very small amounts of liquids within short timescales (Chapter 5).

The wall shear stress from millimeter sized jetting bubbles was studied in detail both in time - the lifetime of the jet is only a few microseconds - and in space. After impacting onto the nearby boundary the jet spreads out radially shearing the surface. Chapter 2 studies this feature in detail, in particular we find experimentally a power law decrease, $-11/4$, of the wall shear stress with distance from the stagnation point. The same dependency has been predicted for a *steady* impinging jet [1].

The distance of the bubble to the wall also has a strong influence, far from the wall ($\gamma > 2.5$) the jet has to traverse the intervening liquid, where it loses most of it's strength, before it can impact on the wall. As the bubble gets closer the wall shear stress increases up until around $\gamma > 0.6$ where it reaches a maximum. For bubbles even closer to the wall the jet no longer has enough time to accelerate before hitting the wall. But for these small standoff distances there is a second shear flow generating mechanism,

i.e. the radial bubble growth across the surface, which now becomes the dominating factor.

This knowledge of the strong dependence of the local shear strength both on bubble standoff distance and radial distance from the point of impact is important for interpretation of the cell experiments presented in chapter 3.

Evidence for the strong dependency of the membrane poration on the shear stress is presented in chapter 3. Our findings are that a typical cavitation impact pattern on a layer of adherent cells shows concentric rings, around the impact point, with different degrees of membrane damage. The inner circle directly below the bubble is completely denuded of cells. Surrounding this empty patch is an annular ring off cells which has been porated as indicated by their uptake of a fluorescent marker (Calcein). Some cells directly on the boundary with the empty patch have partially detached and taken on a spherical shape but were seen to reattach in the following 12-24 hours after cavitation exposure. Finally outside of the zone of porated cells lie the cells which felt no measured effect from the cavitation bubble.

The conclusion from chapter 2, that bubble growth creates shear when the bubble is in contact with the surface, resurfaces in chapter 3. Cells are porated for stand-off distances all the way up to 0 where the jet no longer exists. Thus a second mechanism, the radial growth of the bubble across the surface, is generating the shear required to porate the cells. This finding nicely agrees with that of Venugopalan's group [2, 3].

This radial bubble growth on top of a surface can easily be translated to microfluidics. A cavitation bubble generated in a chamber much lower than it is wide expands radially in a quasi-2D fashion [4]. Seeding adherent cells in such a chamber then allows us to create a radially expanding "pancake" like bubble on top of this layer. In chapter 4 we demonstrate this that all adherent cells contained within the maximum bubble radius are porated and no cell death or detachment is observed.

Chapter 4 also discusses the interaction of cavitation bubbles with suspension cells in a similar geometry. In an attempt to keep cells from being flushed away a spatial light modulator (SLM) is used to create multiple bubbles surrounding the target cells. The target cell trapped between the two bubbles is seen to slightly shrink and shrivel suggesting that membrane poration was achieved here, too.

The multi bubble experiments show that the 2 dimensional character of the setup does not rule out jetting. If the bubble is generated near a boundary such as a second bubble or a chamber side wall the quasi-2D

bubble will jet towards this boundary [4]. This jetting on the microscale inspired us to design a microfluidic pump driven by a cavitation bubble in chapter 5. The chip is simple in design and fabrication and the pump works remarkably well pumping a few picoliter into the channel each stroke.

Finally a cavitation bubble inside a microchannel is studied. A laser pulse is focussed inside a capillary to create a very thin cylindrical bubble. The dynamics is compared to an established model and our newly developed model. What's new in the model is the addition of a thermal effect which, when comparing to the experiments, turns out to improve the results enormously.

To make the effect of the limited length of the tube as small as possible the bubble was created in the middle of the tube. The final chapter discusses the other extreme: creating the bubble at the end of a capillary. The asymmetry causes the bubble to only expand in the direction of the open end pushing any intervening liquid out. These jets erupting from the tube opening were measured to go as fast as $120\mathrm{m}/\mathrm{s}$.

This work demonstrates the large area where laser induced cavitation bubbles can be utilized. They are fluid actuators with enormous potential in particular in confined geometries.

References

[1] M. B. Glauert, "The wall jet," *J. Fluid Mech.* **1**, pp. 625 (1956).

[2] K. R. Rau, A. G. III, A. Vogel, and V. Venugopalan, "Investigation of laser-induced cell lysis using time-resolved imaging," *Appl. Phys. Lett.* **84**, pp. 2940 (2004).

[3] K. R. Rau, P. A. Quinto-Su, A. N. Hellman, and V. Venugopalan, "Pulsed laser microbeam-induced cell lysis: time-resolved imaging and analysis of hydrodynamic effects," *Biophys. J.* **91**, pp. 317 (2006).

[4] E. Zwaan, S. L. Gac, K. Tsuji, and C. D. Ohl, "Controlled cavitation in microfluidic systems," *Phys. Rev. Lett.* **98**, pp. 254501 (2007).

Summary

The behavior of a cavitation bubble is greatly influenced by its surroundings. In an unbounded liquid a cavitation bubble grows and collapses spherically but a nearby solid boundary changes everything. Now the bubble collapses towards the wall and looses its spherical shape. During collapse a thin jet is formed piercing through the center of the bubble aimed towards the wall. Upon impacting on the boundary the jet spreads out radially exerting a strong shear stress on the wall. The shear strength drops with a $-11/4$ power law.

The strength of the jet depends strongly on the starting distance between the bubble and the wall. The jet impact velocity increases the closer the bubble gets to the wall up to a maximum for a standoff distance of about ~ 0.6. For bubbles closer than that the jet velocity decreases.

This jet flow can be utilized to temporarily porate the membranes of living cells; adherent cells are grown on the wall of a culture flask and exposed to a single cavitation bubble. As the jet impacts on the cell monolayer it detaches cells in a circular region around the point of impact. Surrounding the cleared area there is a ring where the shear stress was to weak to detach the cells but strong enough to rip small holes in the cell membrane.

This permeabilization of the membrane can be detected by adding a dye to the liquid such that only the porated cells will be stained. Afterwards the cells are tracked for an entire day to make sure they survive the treatment.

Interestingly enough when a bubble is created with a standoff distance smaller than $\gamma = 0.6$ the amount of stained cells keeps increasing while the circular detachment area shrinks. The cause for this is the bubble growth on top off the surface which is also strong enough to porate cells.

This finding can be used for instance in microfluidics. If a bubble is created in a thin liquid film between two parallel plates the bubble takes on a flat pancake like shape. This quasi 2-dimensional bubble grows and collapses in a circular fashion and no jets are formed. But as was shown

before bubble growth across a surface can also porate cells and by growing cells on one of the two walls in such a system this was also proven the case in microfluidics.

Cells in suspension can also be porated but during bubble growth they take on a "tear" shape which is expected to be a result of entraining the cell from the boundary layer into the main flow. A way to circumvent this instability we created a second bubble on the other side of the cell. The cell becomes compressed and simultaneously sheared yet it remains in place.

Bubbles in confined geometries jet in the presence of a channel wall; even when a small channel opening is present. By positioning the bubble such that the jet does not impact on the wall but flows into the a channel opening realizes a pump. This idea which was put forward for larger millimeter sized bubbles by Khoo's group (*Khoo, et.al. 2005*) has now been for the first time realized on the microscale for lab on a chip devices.

Similar to the step from 3D to 2D the addition of second side wall close the first side wall takes us from 2D to a quasi 1-dimensional bubble. A bubble generated in such a long and thin channel only grows and collapses in the lengthwise direction of the channel. A one dimensional model does indeed describe the bubble dynamics quite accurately but only if the temperature inside the bubble is taken into account.

This time another solid boundary will not induce jetting in the bubble. A free interface close to the jet however does result in a jet. It is however not a jet penetrating through the bubble but the result of the rapidly growing bubble pushing liquid out of the open end of the channel. We demonstrate on demand and reproducible jetting on the micrometer scale with more than 100 m/s.

Samenvatting

De dynamiek van een cavitatie bel wordt sterk beinvloed door zijn omgeving. In een oneindige vloeistof zal de bel nog spherisch groeien en imploderen maar is er een vaste wand in de buurt dan verandert alles. De cavitatie bel verliest zijn bolvorm en beweegt tijdens het imploderen naar de wand toe. Tijdens dit process wordt er ook een dunne vloeistof straal gevormd die door het midden van de bel schiet richting de vaste wand. Nadat de vloeistof straal op de wand heeft geraakt stroomt de vloeistof radieel langs de wand weg waarbij het een sterke afschuifspanning uitoefent op de wand. Deze afschuifspanning neemt af naarmate de afstand vanaf het midden toeneemt en wel volgens deze afstand tot de macht $-11/4$.

De afstand tussen de wand en waar de bel gevormd wordt heeft ook een grote invloed op de kracht van de vloeistof straal die gevormd zal worden. De kracht neemt toe naarmate de bel dichterbij de wand gevormd wordt tot de ge-non-dimensionaliseerde afstand γ gelijk is aan ongeveer 0.6. (De afstand tussen de bel en de wand wordt dimensieloos gemaakt door hem te delen door de maximale straal van de bel). Rond $\gamma = 0.6$ is de kracht van de straal maximaal want voor bellen die dichterbij de wand worden gevormd neemt de kracht weer af.

Deze vloeistof straal kan gebruikt worden om tijdelijke porien in cel membranen te creëren. Een enkele laag cellen wordt op de bodem van een kweek flacon gegroeid en dan blootgesteld aan een enkele caviterende bel. De inslag van de vloeistof straal is zo krachtig dat alle cellen rondom dat punt worden weggespoeld. Op de rand van de lege zone is the afschuifspanning zo afgezwakt dat de cellen niet meer losgerukt worden van de wand, the stroming is echter nog wel net krachtig genoeg om in een grens gebied van enkele cellen diep kleine gaatjes in de celmembranen te creëren.

Dit permeabiliseren van het cel membraan kan worden gedetecteerd door een kleurstof toe te voegen zodat alleen de cellen met geperforeerde membranen gekleurd worden. Na het cavitatie experiment worden de

cellen nog een dag lang gevolgd om er zeker van te zijn dat de cellen het ook op de langere termijn overleven.

Voor bellen dichter bij de wand dan $\gamma = 0.6$ neemt de kracht van de vloeistof straal af, interessant genoeg blijft het aantal gepermeabiliseerde cellen toenemen terwijl het aantal weggespoelde cellen wel afneemt. De rede hiervoor is dat voor deze bel-wand afstanden de cavitatie bel op het oppervlak groeit wat op zichzelf al krachtig genoeg blijkt te zijn om cellen membranen te perforeren.

Dit tweede mechanisme kan heel goed toegepast worden in micro fluidica. Als er een cavitatie bel wordt gecreëerd in een dunne vloeistof laag tussen twee parallele wanden dan neemt hij een platte pannekoek vorm aan. Deze quasi 2-dimensionale bel is radieel symetrisch en zal geen water straal vormen. Maar zoals hiervoor al is gezegd is de radiële bel expansie over een cel laag genoeg om de cellen te permeabiliseren. Door cellen in een dergelijk systeem te kweken en aan cavitatie bloot te stellen is bewezen dat dit inderdaad ook werkt in een micro-systeem.

De tot nu toe besproken cellen groeien op de wand maar de interactie tussen suspensie cellen en cavitatie bellen is net zo intressant. Tijdens de groei van de bel nemen cellen in de directe nabijheid een "druppel"-vorm aan wat waarschijnlijk komt doordat zo'n cel zich deels in de grenslaag bij de wand bevindt waar de stroomsnelheid naar nul gaat. Een oplossing hiervoor is het introduceren van een tweede bel aan de andere kant van de cel. Door de symetrie die er dan onstaat zal de cel geperst en opgerekt worden tussen de twee bellen maar niet meer verplaatst worden.

Deze 2-dimensionale bellen zullen wel een water straal produceren als er een zijwand nabij is; zelfs als een kleine kanaal opening in de wand zit. Door de cavitatie bel zo te positioneren dat de water straal dan niet op de wand maar in deze kanaal opening stroomt kan er een pomp gerealiseerd worden. Dit idee dat is bedacht voor millimeter grote 3D bellen door de groep van Khoo (*Khoo, et.al. 2005*) is nu voor het eerst ook op een microschaal verwezenlijkt.

Gelijk aan de stap die ons van 3D naar 2D bracht zal een tweede zijwand (de bel bevindt zich nu aan een dun vierkant kanaal) een bij bandering 1-dimensionale cavitatie bel opleveren. Vlak nadat de bel gevormd is zal hij al de gehele buis doorsnede gevuld hebben en kan daarna alleen nog in de lengte richting van de buis groeien. De dynamica van de bel is dan ook heel goed te voorspellen met een 1D-simulatie model maar alleen als de temperatuur van de voeistof damp in de bel wordt meegenomen.

De verdere toevoeging van solide wanden zal nu geen vloeistof straal

meer opeleveren. De introductie van een vrij oppervlak resulteert nog wel in een vloeistof straal, maar de manier waarop is geheel anders dan de vloeistof stralen die tot nu toe besproeken zijn. Door de cavitatie bel zich dicht bij een door lucht omgeven uiteinde van de buis te laten vormen zal de bel tijdens zijn expansie vloeistof met hoge snelheid uit de buis persen. Het resultaat is een reproduceerbare vloeistof straal op micrometer schaal met snelheden van boven de $100\mathrm{m}/\mathrm{s}$.

Acknowledgements

The research described in this thesis is financially supported by the "Nederlandse Organisatie voor Wetenschappelijk Onderzoek (NWO)" through the VIDI program. It was carried out at the Physics of Fluids research group of the faculty of Science and Technology of the University of Twente with two month-long visits to the division of Physics and Applied Physics at Nanyang Technical University in Singapore. I gratefully acknowledge the support of these institutions.

First of all, I want to thank my two promotors Prof. dr. Detlef Lohse and assist. Prof. dr. Claus-Dieter Ohl for giving me the opportunity to do my PhD research at the Physics of Fluids group and for the freedom I had in conducting it. They taught me a lot in these four years, both on doing research and on writing up and presenting the results afterwards.

During my PhD I was surrounded by a lot of knowledgeable people that I could cooperate with or were more than willing to help me in some other way. Coming from a pure physics background I knew next to nothing about bio-medical research, making the work with Erwin Nijhuis and Séverine Le Gac very educational and fruitful for which I am very gratefull. For the 'cells&cavitation' chapters I would also like to express my gratitude to Yvonne Kraan for teaching me the basics on cell culturing and helping us set up our own bio-workplace. Also I would like to thank Michel Delius, Tom Groothuis and Karthigayan Gunalan for providing various cell lines.

I would like to thank Pedro Quinto Su for allowing me to use his setup and helping me when needed during my stay in Singapore. Also many thanks to Zhao Xue, Roberto Gonzales Avila, Lammert Heijnen, Fridaus Prabowo, Tobias Mueller and Rainer Dumke for the many games of tablesoccer and just making my stay in Singpore that much more fun.

I would like to thank Chao Sun for coming up with the experiment and the work he did on the 1D-cavitation in a capillary tube. Many thanks to Edip Can for the numerical calculations he did on this subject, the agreement with the experimental data is still impressive.

I want to thank my further co-authors Albert van der Berg, István Vermes, André Poot, Peter Rainer Preiser and Andrea Prosperetti for the significant contributions they made to the thesis.

Over the past four years I had a lot of bachelor and master students in the lab doing part of the tedious measurements for me for which I am very grateful! I would like to thank Johan van der Dennen for continuing the work on the acoustic scallop, Hans van Tooren and Emily van Mierlo and Bram Elschot for their work on the shearing of cells, Koen Winkels and Merlin Kole and Mark-Jan van der Meulen for their work on various microfluidic bubble-pumps, Theo Driessen and Jelle Storteboom for recording some very nice jets piercing through cavitation bubbles and finally Ivan van der Kroon and Erik-Jan Staat for their work on jetting from capillary tubes.

I would like to thank Joanita Leferink for all the administrative work, especially in the last months of the PhD. Thanks to the technical staff, Bas Benschop for the hard and software support and Gert-Wim Bruggert and Martin Bos for making al the parts I came up with and for making the wise decision to not buy me that lab-chainsaw.

I would also like to acknowledge all the members of the group, and my many office and lab-mates through the years in particular, for providing a fun working environment. Special thanks to my paranimfen Aaldert Zijlstra and Arjan van der Bos for their willingness to stand beside me at my defense.

On a more personal note I would like to thank my parents Jan and Máire and my sister Orla for their support both in my PhD and in general. I would also like to take this opportunity to express my thanks the family Eijck for welcoming me so freely into their midst.

Finally, I want to thank Anja Eijck for her love and support despite my apparent disability to grow up.

Rory Dijkink
Enschede, May 2009

About the author

Rory Dijkink was born on March 2nd, 1979, in Amsterdam, the Netherlands. He graduated from high school at "Fons Vitae Lyceum" in Amsterdam in 1997, and started studying Applied Physics that same year at the University of Twente in Enschede. His studies included a study-tour of California and Mexico City in 2002 and a three-month traineeship at the Medizinisches Laserzentrum in Lübeck in 2003. In 2005 he graduated on the self-propelled microdevice "the Acoustic Scallop" in the Physics of Fluids. After his studies he continued as a PhD in the same group working on laser induced cavitation and the effects of various solid boundaries on the cavitation collapse. The main part of the work was done in the labs of prof. dr. Detlef Lohse at the University of Twente but for two months he did research at NanYang Technical University in Singapore while visiting his second promoter dr. Claus-Dieter Ohl.